Activated Liquid Transport by Thermal Marangoni Effect and by Avoiding the Coffee Ring Effect

Dissertation

Zur Erlangung des Grades

"Doktor der Naturwissenschaften"

im Promotionsfach Physikalische Chemie

am Fachbereich Chemie, Pharmazie und Geowissenschaften

der Johannes Gutenberg-Universität Mainz

Aiting Gao

Geboren in Shanxi, P.R China

Mainz, 2021

Die vorliegende Arbeit wurde im Zeitraum von September 2016 bis March 2021 unter der Anleitung von [In der elektronischen Fassung aus Datenschutzgr¨unden entfernt] am Max-Planck-Institut für Polymerforschung in Mainz angefertigt.

Tag der mündlichen Prüfung: 25. May 2021

Dekan: [In der elektronischen Fassung aus Datenschutzgr¨unden entfernt]
1. Berichterstatter:
2. Berichterstatter:
3. Berichterstatter:

Dissertation an der Universit¨at Mainz (D77)

Declaration

I hereby declare that I wrote the dissertation submitted without any unauthorized external assistance and used only sources acknowledged in the work. All textual passages which are appropriated verbatim or paraphrased from published and unpublished texts as well as all information obtained from oral sources are duly indicated and listed in accordance with bibliographical rules. In carrying out this research, I complied with the rules of standard scientific practice as formulated in the statutes of the Johannes Gutenberg University Mainz to ensure standard scientific practice.

<div align="right">

Aiting Gao, Mainz..

</div>

Zusammenfassung

Flüssigkeitstransport, insbesondere auf der Mikrometerskala, ist entscheidend für zahlreiche Anwendungen wie z. B. die Mikrofluidik für chemische oder biochemische Analysen und den Tintenstrahldruck. Für Strömungen im Mikrometermaßstab gibt es einen signifikanten Einfluss der Grenzflächen. Je kleiner die Größe eines Systems ist, umso größer wird die Fläche der Grenzflächen im Vergleich zum eingeschlossenen Volumen. Um also Strömungen auf der Mikroskala zu erzeugen, zu kontrollieren und zu manipulieren, spielen Grenzflächen eine bedeutende Rolle.

Meine Studie konzentriert sich darauf, wie Flüssigkeitsströmungen unter Variation der Bedingungen an den Grenzflächen, d.h. durch Einführung von Oberflächenspannungsgradienten, lokal unterdrückter Verdampfung oder lokaler Erwärmung, beeinflusst werden. Diesbezüglich habe ich zwei Fälle untersucht:

a) die optische Manipulation von Flüssigkeitsströmungen durch den Thermokapillareffekt an superhydrophoben Oberflächen

b) Steuerung der Verdampfung zur Manipulation von Strömungen in einem verdampfenden Tröpfchen auf ölbenetzten Oberflächen

Eine praktikable Möglichkeit, Flüssigkeitsbewegungen auszulösen, ist die Einführung von Oberflächenspannungsgradienten an freien Flüssigkeitsgrenzflächen, was zum Marangoni-Effekt führt. Dieser Ansatz wurde jedoch nur selten angewendet, um kontinuierliche Strömungen in begrenzten Flüssigkeitssystemen, z. B. in mikrofluidischen Geräten, auszulösen, da es keine freien Flüssigkeitsgrenzflächen gibt. Im ersten Fall der beiden genannten Projekte wird experimentell gezeigt, dass nicht benetzte superhydrophobe Oberflächen die notwendige freie Flüssigkeitsgrenzfläche bereitstellen können, um Marangoni-Strömungen zu ermöglichen. Mit Laserlicht heize ich diese Oberfläche asymmetrisch auf und erzeuge so über die erzeugten Gradienten in der Oberflächenspannung Flüssigkeitsströmungen in der Nähe der Flüssigkeitsgrenzfläche. Mit konfokaler Mikroskopie und computergestützten Strömungssimulationen wurde die Strömungsgeschwindigkeitsverteilung in der flüssigen Phase analysiert. Meine Ergebnisse zeigen, dass es möglich ist Marangoni-Strömungen auf superhydrophoben Oberflächen mit einer optischen Methode zu erzeugen. Ich stellte fest, dass neben den Marangoni-Strömungen auch eine auftriebsgetriebene Strömung auftreten kann, die in früheren Arbeiten über Marangoni-Strömungen an superhydrophoben Oberflächen noch

nicht berücksichtigt wurde. Der Beitrag dieser beiden Mechanismen wird untersucht, um Richtlinien für ein effizientes Design von Marangoni-Pumpsystemen zu liefern.

Im zweiten Fall der untersuchten Grenzflächenmodifikationen befasse ich mich mit dem Trocknungsmuster eines Tropfens. Im Allgemeinen ist die Verdampfung eines Tropfens entlang seiner freien Flüssigkeitsgrenzfläche inhomogen. Diese Inhomogenitäten induzieren Strömungen innerhalb eines Tropfens. Dies wiederum beeinflusst die Trocknungseigenschaften. Ein weit verbreitetes Phänomen ist z. B. der allgegenwärtige "Kaffeering"-Effekt, benannt nach den ringförmigen Strukturen von Rückständen, die nach dem Trocknen eines Kaffeetropfens auf einer Oberfläche zurückbleiben. Bei Druck-, Strukturierungs- und Beschichtungsprozessen, bei denen es auf gleichmäßige Muster ankommt, stellt dieser Effekt jedoch eine große Herausforderung dar. Daher sind Methoden zur Unterdrückung des Kaffeering-Effekts sehr gefragt.

In diesem Projekt stelle ich einen Ansatz vor, der das Verdampfungsprofil an der Tropfenoberfläche direkt steuern kann um den Coffee-Ring-Effekt zu unterdrücken Wasser Tröpfchen werden auf ein mit einem nicht mischbaren Öl vorbenetzten Substrat aufgebracht. Das Öl - mit geringerer Oberflächenspannung - steigt spontan auf und bildet einen scheinbaren "Benetzungsrand" um den Tropfenrand. Dieser Öl-"Benetzungsrand" hilft, die Verdampfung von Flüssigkeit am Tropfenrand zu verhindern. Dadurch werden die nach außen gerichteten Kapillarströmungen unterdrückt, die normalerweise zum Kaffeering führen.

Infolgedessen werden Aufwärtsströmungen erzeugt, die nichtflüchtige Bestandteile wie z. B. Partikel gelöst im Tröpfchen, zur Tröpfchen Oberfläche treiben. In der Folge kommt es zu gleichmäßigen Ablagerungen auf dem Substrat. Dieser Mechanismus wurde durch die Beobachtung des dynamischen Verhaltens von Kontaktlinien, Kontaktwinkeln und des Migrationsprozesses von dispergierten Partikeln im verdampfenden Tropfen verifiziert.

Als eine mögliche Anwendung habe ich eine Reihe von Suprapartikeln (zusammengesetzt aus kleineren Partikeln) mit scheibenartiger Form hergestellt. Tests mit chemisch unterschiedlichen Arten von Partikeln wurden mit diesem einfachen Ansatz durchgeführt, um seine breite Anwendbarkeit zu zeigen.

Zusammenfassend lässt sich sagen, dass die Steuerung von Flüssigkeitsströmungen durch die Manipulation von Flüssigkeitsgrenzflächen anwendbar ist und zu einem faszinierenden Flüssigkeitsverhalten führt. Dies bietet neue Möglichkeiten in Anwendungen wie Flüssigkeitspumpen, -transport und Oberflächenstrukturierung.

Abstract

Liquid transport, particularly on the micrometer scale, is crucial for numerous applications, such as microfluidics for chemical or biochemical analysis, and inkjet printing. For flows on the micrometer scale, there is a significant influence of the interfaces. This is because the smaller the size of the system, the larger the area of the interfaces becomes compared to the enclosed volume. Hence, in order to create, control and manipulate flows on the microscale, interfaces play a significant role.

My study focuses on how liquid flows, subjected to variations of the conditions at the interfaces, i.e., by introducing surface tension gradients, locally suppressed evaporation or local heating, are affected. In this respect, I investigated two cases:

a) optical manipulation of liquid flows by the thermocapillary effect on superhydrophobic surfaces

b) controlling evaporation to manipulate flows in an evaporating droplet on surfaces prewetted with oil

A feasible way to trigger liquid motion is to introduce surface tension gradients on free liquid interfaces, which leads to the Marangoni effect. However, this approach has been rarely reported to trigger continuous flows in confined liquid systems, e.g., microfluidic devices, due to the lack of free liquid interfaces. In the first case of the two mentioned projects, I show experimentally that non-wetted superhydrophobic surfaces can provide the necessary free liquid interface to allow for Marangoni flows. I use laser light to heat this surface asymmetrically. Thereby fluid flows are created near the liquid interface via the gradients produced in the surface tension. With confocal microscopy experiments and computational fluid dynamics simulations, the flow velocity distribution in the liquid phase was analyzed. My results show that it is possible to introduce Marangoni flows on superhydrophobic surfaces with an optical approach. I find that besides the Marangoni flows, a notable buoyancy-driven flow may occur, which has not yet been considered in previous works on Marangoni flows at superhydrophobic surfaces. The contribution of these two mechanisms is investigated to provide guidelines for an efficient design of Marangoni pumping systems.

In the second case of the investigated interface modifications, I address drying patterns of a droplet. In general, the evaporation of a droplet is non-uniform along its free liquid interface. This induces flows within the droplet, which ultimately affect its drying features. For instance,

a wide-spread phenomenon is the "coffee ring" effect, named after the ring-like structures of residues left after a drop of coffee has dried on a surface. However, in printing, patterning and coating processes, where uniform patterns are highly required, this effect presents a major challenge. It is hence highly desired to methods to suppress the coffee-ring effect.

In this project, I introduce an approach that can directly control the evaporation profile at the droplet surface to suppress the coffee-ring effect. It is realized by depositing water droplets on a substrate pre-wetted by a with water immiscible oil. The low-surface-tension oil spontaneously climbs up and forms an apparent "wetting ridge" around the droplet edge. This oil "wetting ridge" helps to hinder liquid from evaporating at the droplet edge. This suppresses the outward capillary flows, which normally lead to the coffee ring.

Consequently, upward flows are generated and drive non-volatile components, such as particles dispersed in the droplet, toward the droplet surface. In consequence, I have produced uniform depositions on the surface. This mechanism is verified by monitoring the dynamic behavior of contact lines, contact angles, and the migration process of dispersed particles in the evaporating droplet.

As a possible application, I have produced a range of supraparticles (assembled from smaller particles) with disk-like shapes. Tests with chemically different types of particles have been performed by this straightforward approach to show its wide range of applicability.

In summary, controlling liquid flows through manipulating liquid interfaces is applicable and leads to fascinating liquid behavior. This provides new possibilities in applications such as fluid pumping, transporting, and surface patterning.

Table of Contents

1. Introduction

Understanding how to modify liquid transport at the microscale can help to have a fundamental understanding of many physical phenomena, *e.g.,* "tears" of wine,[1-2] regulated or chaotic convective cells[3-6] and the "coffee ring" effect[7]. For liquid flows on microscopic length scales, manipulating the fluid interface provides a natural approach to manipulate and control flows due to their large surface-to-volume ratio. Traditional techniques such as mechanical pumping, magnetic stimuli, electro-wetting, or electro-osmotic force are used to manipulate liquids with micro/milliliter volumes. They however mostly take effect on the bulk of the fluid. For mechanical pumping, this leads to a large increase in the required pumping pressure with decreasing size of the channel.

An alternative to omitting these techniques is to vary parameters defining the liquid interfaces, *e.g.,* surface tension or local control of evaporation. With the term liquid interface, I always refer to water-air interfaces. The liquid interface is not only the boundary that separates two immiscible phases, but opposed to a solid-liquid interface, it is also a boundary that can move. This provides an excellent platform to manipulate flows in the liquid. In the following, I will briefly introduce some key features of these two mechanisms that are fundamental to my studies.

1.1 The Marangoni effect

The Marangoni effect occurs when a variation of surface tension is present at the interface between two fluids, e.g., between a liquid phase and a gas phase. The difference in surface tensions induces a directional flow along the interface. (**Figure 1**) This effect is named after Carlo Marangoni.[8-9] By observing an oil droplet spreading on a water surface, he concluded that the spreading occurs due to the surface tension variation between the two liquids. This effect can be applied to all liquid or fluid systems. The Marangoni effect plays a critical role in many liquid dynamic behaviors, such as directional/convective flows[10-11], guiding droplets/floating objects transport at the fluid interfaces[12] and many spreading dynamic phenomena, *e.g.,* fingering instabilities[1-2, 13-14] and "Marangoni bursting" (a large droplet spreads and breaks up into thousands of tiny droplets)[15].
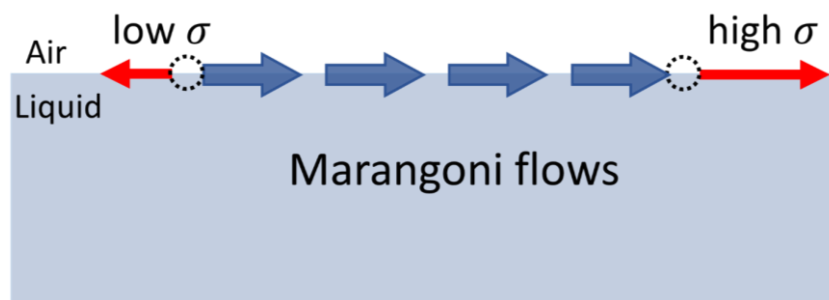
Figure 1. Illustration of Marangoni flows due to surface tension variation on a liquid interface. Red arrows: surface tension stress; Blue arrows: Surface flows from the region of low surface tension to the region of high surface tension.

The Marangoni effect can be created by applying a thermal, solvent, or electrical gradient at the liquid interface[1] leading to a gradient in surface tension. Thermally-induced Marangoni flows are also called thermocapillary flows. They allow microscale operations with optical heating, e.g., actuation of microswimmers[12] or droplets[16], and guiding flows by dispersing photothermal metallic nanoparticles in liquid systems.[17-19] This is the basis of the emerging field of optofluidics. In addition, the resulting interfacial velocity can be tuned as a function of the temperature gradient along the interface. In contrast to the flows produced by a concentration gradient or by an electric field, temperature gradients can be introduced in various liquids (charged and neutral solutions) and are pollution-free (e.g., without adding surfactants).

The temperature gradient-induced Marangoni flow is the main focus of this thesis.

1.1.1 Thermocapillary effect

Surface tension can vary with temperature in different ways. For most liquids, it decreases with increasing temperature, $\frac{\partial \sigma}{\partial T} < 0$. This decrease is due to the enhancement of molecular mobility with an increase in temperature (which decreases the cohesive interactions between molecules).[20] Under these circumstances, the thermocapillary effect causes liquid flows from heated regions (low surface tension) to cold regions (high surface tension). Under most practical circumstances, the surface tension σ can be considered to vary linearly with the temperature T.[21-23] There are two basic modes:

1) Temperature gradient perpendicular to the free liquid interface. It usually occurs when a liquid layer with a free upper interface is heated from below. The liquid layer becomes unstable when the temperature difference between the bottom and the upper liquid interface

exceeds a critical threshold.[5] In most cases, due to the presence of gravity, the buoyancy effect also needs to be considered. In consequence, the instability in the liquid layer develops into the so-called Marangoni-Bénard convection;[5]

2) Temperature gradient tangential to the free liquid interface. This produces a surface tension gradient (or Marangoni stress) along the liquid interface.[24] The Marangoni effect then induces surface flows from low to high surface tension regions.

The flow patterns that evolve from the Marangoni flow in a fluidic system will depend on the geometry of the system. For example, in a container with an upper free interface, backflows will occur due to mass conservation in the system (**Figure 2**).
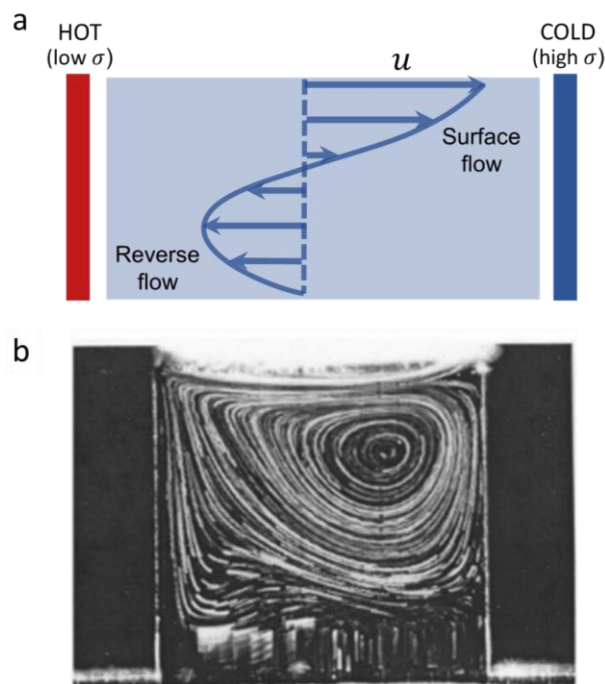
Figure 2. Example for the onset of Marangoni convective cells in a liquid phase. (a) Schematic of the thermocapillary-induced liquid flow in the liquid layer. The flow propagates near the upper liquid interface from a hot to a cooled region, while a reversed flow occurs at the deeper part of the liquid layer due to mass conservation. (b) Thermocapillary convections in a $NaNO_3$ melt solution in a rectangular container.[25]

The thermocapillary-induced liquid flow near the liquid interface can drive floating or immersed objects, including bubbles and droplets, along a temperature gradient from the heated regions to cold regions.[25] For a thin liquid film, deformation or rupture can occur due to the thermocapillary effect.[26-30] Recently, the spatial control of the liquid rupture due to the

thermocapillary effect in jet dynamics and its potential in inkjet printing techniques has been reported.[31-32]

1.1.2 Thermocapillary flows on non-wetting surfaces

As discussed before, the thermocapillary effect produces Marangoni flow in the liquid phase. It could be expected for this flow to be the driving force for liquid transport in microfluidic devices. However, for a liquid phase on solid surfaces, this surface-driven flow cannot be realized in the absence of the liquid-fluid interfaces at which a surface tension gradient ($\frac{\partial \sigma}{\partial x}$) can develop.

To solve this problem, it has been proposed to utilize superhydrophobic surfaces to introduce liquid-fluid interfaces (the gas is here treated as fluid) and trigger thermocapillary flows.[33] A superhydrophobic surface is a surface that has micro-/nanoscale features and is chemically hydrophobic, such as a Lotus leaf.[34] These surfaces have contact angles higher than 150° and roll-off angles of less than 10° for water droplets. They have paid much attention because of their liquid repellency and drag reduction abilities.[35] A liquid phase (e.g., water) on such a surface will only stay on the protruding tips while keeping the air in the valleys between these structures. This wetting state is also called the "Cassie-Baxter" state (**Figure 3**). Therefore, at the contact area between the liquid and the substrate, a discontinuous liquid-air interface is formed.
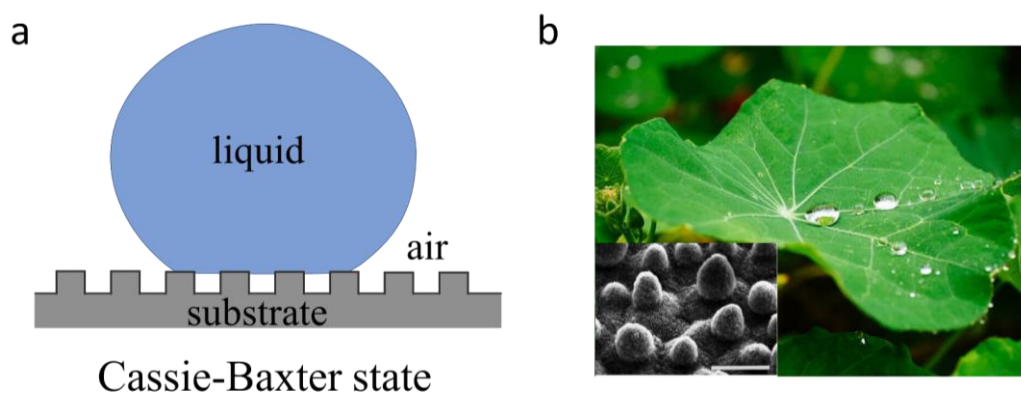
Figure 3. (a) Schematic illustration of a liquid droplet in the Cassie-Baxter state. (b) Self-cleaning on lotus leaves. Inset shows the hierarchical bump structures on a leaf surface. Source: Gardenbetty. Inset: Reprinted with permission from[34], Copyright by Springer Nature.

Baier *et al.* [33] have theoretically predicted that thermocapillary flows can be induced on the superhydrophobic surface when imposing it with a temperature gradient. The direction of the

liquid flow agrees with the direction of temperature gradient decrease, which corresponds to the increase of surface tension (**Figure 4**). He has predicted that a thermocapillary flow of up to a few mm/s can be achieved over superhydrophobic surfaces with a temperature gradient of 10 °C/cm. More recently, Amador *et al.* [36] experimentally examined thermocapillary flows in channels with micro-pillar structured sidewalls. When imposed a temperature gradient of 2 °C/cm along the channel, flows with a speed of 10 ~ 50 μm/s were observed.
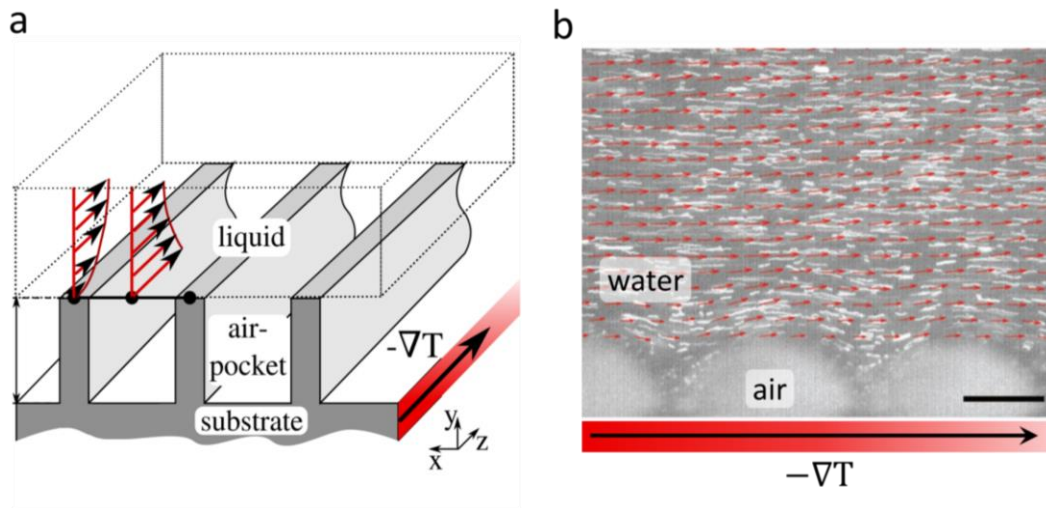
Figure 4. Thermocapillary-induced flow on a superhydrophobic surface (with fin structures). (a) Schematic of the thermocapillary flow under a temperature gradient; Reprinted with permission from [33], Copyright (2010) by the American Physical Society. (b) Flow visualization by tracing particles that are dispersed in the water phase. Scale bar: 50 μm. Reprinted with permission from[36], Copyright by John Wiley and Sons.

To the best of our knowledge, only a few theoretical investigations on thermocapillary flows over superhydrophobic surfaces have been reported.[33, 37-38] Baier *et al.*[33] theoretically investigated the directional flows formed near a superhydrophobic surface with fin structures. They investigated the flows in the longitudinal case (where the surface structure is parallel to the flow directions) or transverse case (surface structure particular to the flows). So did other theoretical works[33-34]. However, on a superhydrophobic surface with irregular structures, the surface structures' orientation may lead to different velocities. Such structures have not yet been addressed. Hence, in this thesis, I investigated this issue and expected to provide more guidelines for designing Marangoni-driven superhydrophobic fluidic systems. Furthermore, all previous work relies on direct heating of the liquid interface. In my work, I showed that this heating could also be obtained optothermally.

1.2 The Coffee ring effect

Another efficient approach to manipulating liquid transport is to control liquid evaporation across the liquid-air interface. Liquid evaporation has attracted attention due to its complex liquid phenomena and importance toward biological and industrial applications, such as printing and coating processes, water desalination,[39] energy generation,[40] phase-change cooling,[41] and biomedical systems. For these applications, understanding and manipulating the internal flows in the evaporating liquid phase is crucial. This thesis will focus on investigating a simple evaporation model--a sessile droplet evaporating on a substrate.

A sessile droplet evaporating on a solid surface seems to be a simple process; however, its physics is complicated. Multiple interrelated factors included, e.g., wetting phenomena, evaporation flux across its surface, contact line pinning, and the Marangoni effects. These factors are critical to alter the internal flows of the evaporating liquid, which leads to complex fluidic phenomena. In addition, droplets containing nonvolatile components drying on solid substrates can leave different patterns.[42-43]

1.2.1 Droplet evaporation

In general, a droplet containing nonvolatile components, *e.g.,* particles, drying on a solid substrate leaves a ring-like pattern. This pattern is called the "coffee ring" after its most prominent representative in everyday life. During the drying process, the edge of the droplet is pinned to the substrate. (**Figure 5**). The fastest evaporation rate at the contact line[7] causes a certain volume of liquid to evaporate to the outer atmosphere in a short time. To replenish the loss of liquid, the liquid in the interior is driven to the (pinned) droplet edge by an outward flow, which is also called a capillary flow (the curved lines with arrows). During this process, the nonvolatile solutes dispersed in the droplet are also driven to the droplet periphery and accumulated there (**Figure 5b**). Eventually, a ring pattern is formed on the substrate. This phenomenon is ubiquitous in the drying process when the liquids partially wet the solid substrates.
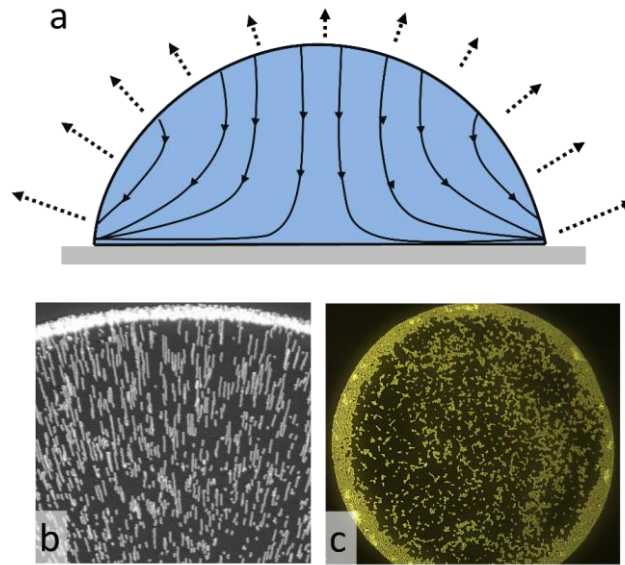
Figure 5. Flow profiles inside a droplet evaporating on a solid surface. Outward flows are generated and drive dispersed matters to its pinned contact line. (a) Schematic of the relevant parameters and the streamlines in the evaporating droplet. The straight dashed arrows: non-uniform evaporation flux of vapor at the liquid-air interface. (b) Visualization of the outward capillary flow in the droplet. White dots: dispersed particles. Reprinted with permission from Ref [44]. Copyright by Springer Nature. (c) A coffee ring deposition formed by drying a droplet on a solid surface.

Pinning of the droplet periphery can arise from the substrate roughness and the nonvolatile solutes accumulating there. The surface roughness (or chemical heterogeneities) temporarily anchors the droplet contact line; this allows nonvolatile solutes to start accumulating here, increasing the energy barrier for the droplet contact line depinning from here.[45] However, not every drying droplet leaves such a ring-like pattern. Other mechanisms, e.g., Marangoni-Bénard convections, Rayleigh-Bénard convections[46] (originates from spatial variation of liquid density, which allows heated, lighter liquid flowing upwards and cooler, denser liquid flowing downwards), and the droplet wetting behavior, may influence flows in the evaporating droplet and affect the final deposition patterns.

The non-uniform evaporation also induces concentration or temperature differences in the liquid phase. These differences induce surface tension gradients at the free liquid interface and lead to Marangoni instabilities, e.g., Marangoni flows/convections.[47-48] For instance, there are two competing flows for a droplet evaporating on a cold substrate (or heated at its apex). One is the outward capillary flow that drives nonvolatile solutes to the edge; the other is the

Marangoni convection induced by the temperature gradient across the droplet surface, which helps drive the nonvolatile solutes away from the edge. Therefore, convective flows form in the droplet (**Figure 6**).[49-52]
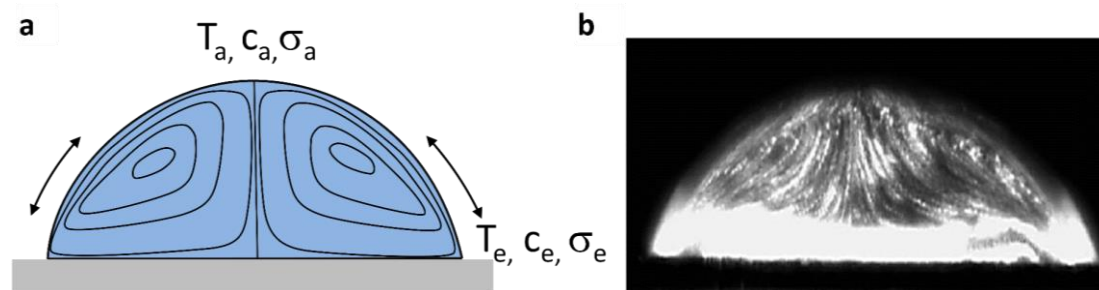
Figure 6. Marangoni convections inside an evaporating droplet on a solid substrate. (a) Streamlines of the convective flows in the droplet. A surface tension gradient between the apex (T_a, c_a, σ_a) and the droplet edge (T_e, c_e, σ_e) is shown at the droplet surface due to the temperature or concentration difference. The direction of the Marangoni flow depends on the real situation. For instance, the Marangoni flow is towards the center of the droplet in the presence of surfactants or evaporation on a heated substrate, while the flow is reversed in some cases of solvent mixtures and evaporation on a cold substrate. (b) Marangoni convections in a drying octane droplet. Fluorescent poly(methyl methacrylate) (PMMA) particles were dispersed in the droplet to visualize the internal flows. Reprinted with permission from Ref[52]. Copyright © 2006, American Chemical Society.

In recent studies, the natural convections caused by density in the evaporating multi-component droplets have also been observed.[53] This effect can play a dominant role by observing opposite radial flows in sessile and pendant binary droplets. Therefore, different flow patterns may be observed during the evaporation and they are influenced by the relative importance of the evaporation rate, the thermocapillary and buoyancy effect.

1.2.2 Suppression of the coffee ring effect

Evaporation of liquids offers an external-field-free and straightforward approach to yield particle self-assemblies with complex and ordered structures. For instance, the "coffee ring" effect has been reported to show its potential in surface patterning with controlled spatial arrangements, such as 1d filaments,[54] concentric "coffee rings" and polygonal network structures.[55] However, in uniform coating applications, such as inkjet printing[56-57] and biological microarrays[58], the nature of the "coffee ring" effect is usually undesired. To regulate

the drying patterns, approaches aiming at modulating the internal flows of the evaporating droplets have been introduced. [52, 59-61]

An efficient approach is by manipulating the vapor flux around the evaporating droplet.[62] Deegan *et al.*[63] have investigated three distinct droplet evaporation manners, i.e., higher evaporation at the droplet rim (edge-favored evaporation), uniform evaporation and higher evaporation at the apex of the droplet, and their deposition features (**Figure 7**). In the first two evaporation cases, ring-like patterns are obtained (**Figure 7a** and **7b**). However, if higher evaporation is illustrated at the apex of the droplet, more homogeneous depositions are produced (**Figure 7c**). The distinct difference of depositions is that as the evaporation flux varies, the internal flows in the evaporating droplets have been altered from the outward capillary flows (first two cases, **Figure 7d**) to upward flows (third case, **Figure 7e**). Thus, the solutes in the droplets are either driven towards the edge or driven to the center of the droplet, which ultimately forms different deposition patterns.
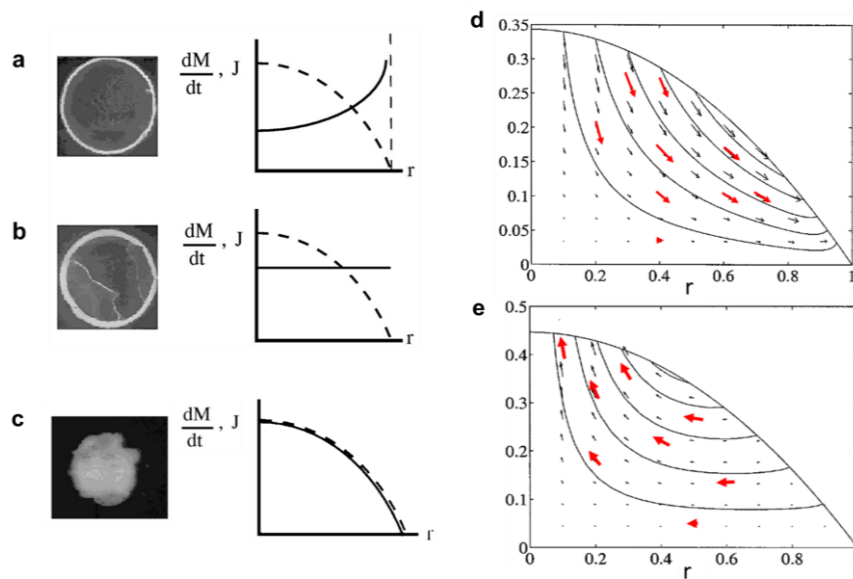
Figure 7. Images of depositions left by droplets dried under different conditions. (a) Higher evaporation at the droplet periphery of a droplet evaporating on a typical substrate; (b) Uniform evaporation mode for a droplet mounted on a pedestal and surrounded by water; (c) Higher evaporation at the droplet apex for a droplet placed in a chamber with a hole above the droplet apex. The first two cases lead to coffee ring patterns, while the last case produced a uniform pattern. The evaporation profile curves for these cases are also plotted. Solid line: the evaporation rate (J); Dashed lines: the height of the droplet interface. (d)(e) The corresponding flow patterns in the sessile droplets in (a), (b) and (c), respectively. Reprinted from Ref[63]. Copyright American Physical Society.

1.2. The Coffee ring effect

These works inspired me to explore an efficient approach to control the droplet evaporation profile. Recently, lubricated surfaces, consisting of micro/nano-structures infused with lubricating liquids, have been attracted much attention since they show low contact angle hysteresis to immiscible droplets.[64-65] The droplet configuration results from interactions among the four distinct phases (oil, air, the droplet, and the solid substrate) in the system. Varanasi *et al.*[66-67] have mentioned that the low-surface-tension oil may climb up and forms an apparent "wetting ridge" around the droplet edge (**Figure 8**).
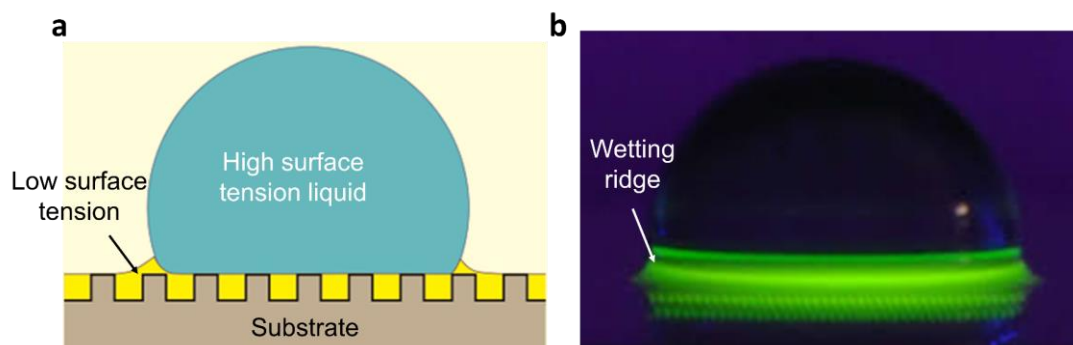
Figure 8. (a) Schematic of a droplet placed on a textured surface infused with a lubricant liquid. Due to the interfacial tension differences, the lubricant forms an apparent "wetting ridge" around the sessile droplet. (b) Photograph of a water droplet on a silicone oil-infused pillar substrate. The oil phase was dyed with a fluorescent UV tracer DFSB-175. Reprinted with permission from Ref.[66], Copyright ROYAL SOCIETY OF CHEMISTRY.

This configuration has attracted much attention focusing on investigating its corresponding dynamic processes, such as the evolution of the oil "wetting ridge" or the shielded droplet in transporting[68] or evaporating processes.[69] However, the evaporation process of the droplet itself is not fully understood yet. One open question is: what is the role of the oil "wetting ridge" during droplet evaporation? Since the lubricant shields the droplet edge, liquids diffuse to the surrounding atmosphere from here may largely decrease and thus changes the evaporation profile along the droplet surface.[70] It shows the potential of manipulating vapor fields around droplets to control their internal flows and even their depositions. This would be of great interest for designing large-scale surface patterning techniques.

1.3 Frame of this work

This thesis deals with two topics in controlling liquid transport by introducing gradients at the liquid interfaces. The first topic introduces a surface tension gradient at the liquid interface. The result Marangoni effect can induce interfacial flows, which then develop into bulk motion. The second topic is to alter flows in the evaporating liquid by controlling the evaporation flux across the liquid surface. This leads to a suppression of the "coffee ring" effect. Both approaches are realized by utilizing non-wetting surfaces, which are introduced in the respective chapter.

Chapter 2 describes an optical approach to triggering continuous liquid flows over solid surfaces by the thermocapillary effect. The experimental setup is designed as a glass substrate fabricated with photothermal materials as the superhydrophobic surface above a millimeter-thick liquid layer. A focused laser is used as the light source to illuminate the superhydrophobic surface from above. The temperature distributions near the substrate and the corresponding thermally-induced flow patterns are investigated by an infrared camera and a laser scanning confocal microscope. The flow mechanisms, i.e., the thermocapillary effect and buoyancy effect and their contributions, are investigated with simulations based on a 2D asymmetric model. Further experiments on surfaces with different morphologies and wettabilities were done for comparison. This study investigates the relationship between the design of the setup and the corresponding flows, which is essential for gaining insight into how to get optimized Marangoni flows.

Chapter 3 describes an effective way to suppress the "coffee ring" effect via a controlled evaporation approach. This is realized by depositing water droplets on low-surface-tension oil-coated surfaces. The laser scanning confocal microscope is utilized to investigate the dynamic evolution of the evaporating droplets, i.e., wetting configuration, contact line behavior, and internal flow patterns. After complete evaporation of the droplets, final deposition features with respect to the experimental conditions, i.e., the substrate wettability, the initial thickness and viscosity of the oil phase, are investigated. Additionally, I also present the potential of utilizing the oil-coated surfaces to prepare supraparticles (agglomeration of small particles forming a bigger particle) on large scales.

These two strategies for controlling liquid transport, including Marangoni flows on superhydrophobic surfaces and the controlled evaporation of the oil-shielded droplets, are summarized in the last chapter.

2 Optothermally-induced fluid flows on superhydrophobic surfaces

The following work is based on the manuscript that submitted to Langmuir, as Gao et al. (2021): *Gao, A., Butt, H.-J., Steffen, W., Schönecker, C.:* Optical manipulation of liquids by thermal Marangoni flow on a superhydrophobic surface. *Langmuir, 2021.* Reproduced in part with permission from *Langmuir*, submitted for publication. Unpublished work copyright [2021] American Chemical Society.

The following texts, figures and tables quoted (within "") are the same in the submitted manuscript.

Thermocapillary flow occurs when a temperature gradient is applied along a liquid-liquid or a liquid-air interface. Here, an active way to trigger liquid flows over superhydrophobic surfaces via an optical approach is introduced. The concept is shown in **Figure 9**.
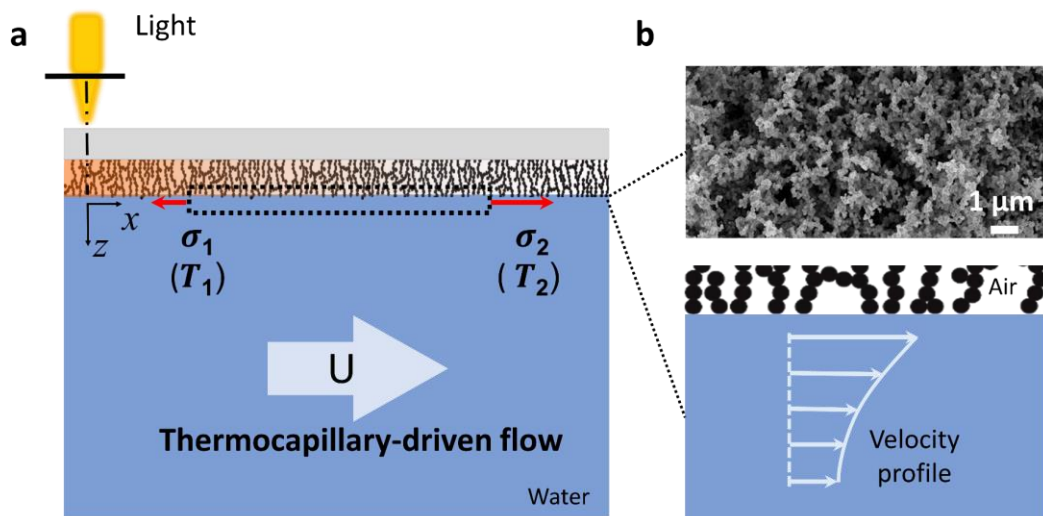
Figure 9. Concept of light-induced thermocapillary flows in a liquid layer, which is in contact with a superhydrophobic surface (on the top). (a) Schematic of the Marangoni flow induced by non-uniform light irradiation on the upper surface. The photothermal effect on the substrate induces a non-uniform temperature distribution at the liquid interface, thus causes Marangoni stress $(\frac{\partial \sigma}{\partial x})$ and lead to directional flows (U). Red arrows illustrate the corresponding surface tension at the hot and cold regions, respectively. (b) Morphology of the soot surface employed in the experiments (top) and schematic of the discontinuous liquid-air interface at the superhydrophobic surface (bottom).

As described in chapter 1.2, the liquid-air interfaces on superhydrophobic surfaces in a Cassie-Baxter state allow us to introduce Marangoni flows at surfaces where otherwise only over solid walls with zero velocity at the surface would be present. In this work, fabricating superhydrophobic surfaces with photothermal materials further adds the functionality to trigger flows via optical heating. For instance, candle soot coating, being black and thus heat-absorbing, has a multi-tier geometry with structures from nanometers to millimeters and its re-entrant structure makes it a good material for superhydrophobic surfaces (**Figure 9b**). Local heating of such a surface via a focused light source will then create a temperature gradient along the superhydrophobic surfaces. The resulting change in surface tension will drive a flow. The fundamentals of this flow, experimental investigations, and the corresponding flow mechanisms are discussed in the following sections.

2.1 Theoretical background

2.1.1 Thermocapillary flow on the liquid-air interface

According to the Eötvös rule, surface tension, especially the surface tension at the liquid-air interface, shows an almost linear relationship with temperature: [23]

$$\sigma = V_m^{-2/3} k(T_c - T) \qquad (2\text{-}1)$$

Here, V_m is the molar volume of the liquid, $V_m = M/\rho$, where M is the molar mass and ρ is the liquid density; T_c is the critical temperature at which σ approaches zero; k is the Eötvös constant, for most liquids $k \sim 2.1 \times 10^{-7}$ J/K·mol$^{2/3}$. If there is a small temperature variation at the surface, its surface tension also can be expressed as:[71]

$$\sigma(T) = \sigma_0(T_0) - \sigma_T(T - T_0) \qquad (2\text{-}2)$$

where σ_T is the surface tension temperature coefficient, $\sigma_T = -\frac{\partial \sigma}{\partial T}$. It is a negative value for most of the liquids. Applying a temperature gradient ($\frac{\partial T}{\partial x}$) at the liquid surface (in x-direction), *e.g.,* local heating of the liquid, the difference in surface tension between the heated and cold regions creates a surface tension gradient along the liquid surface ($\frac{\partial \sigma}{\partial x}$). A tangential surface stress $\tau_{(\sigma)}$ thus arises at the liquid surface, which can be written as $\tau_{(\sigma)} = \frac{\partial \sigma}{\partial x} = -\frac{\partial \sigma}{\partial T}\frac{\partial T}{\partial x}$. In the tangential direction, it is only balanced by the viscous stress $\tau_{(\mu)}$ associated with liquid motion, which is expressed as $\tau_{(\mu)} = \mu \frac{\partial u}{\partial z}$. Therefore, the balance between these two stresses gives:

14

$$\frac{\partial \sigma}{\partial T}\frac{\partial T}{\partial x} + \mu\frac{\partial u}{\partial z} = 0 \tag{2-3}$$

Here, μ is the dynamic viscosity of the fluid. For water that investigated in this thesis, $\frac{\partial \sigma}{\partial T} = -0.155$ mN/(m·k); $\mu = 8.9\times10^{-4}$ Pa·s at 25 °C. u is the fluid velocity generated along x direction in the liquid and z the coordinate perpendicular to the interface (**Figure 9**). Hence, any temperature gradient will induce a flow in the liquid.[72] Equation (2-3) assumes that the surface stress of the air phase is negligible.

The Marangoni number, which defined as the ratio of the thermocapillary flow and viscous force, is also used to characterize the strength of thermocapillary convection. It can be expressed as a velocity times a characteristic length, divided by a diffusion constant. Hence,

$$Ma = u\frac{L}{\alpha} \tag{2-4}$$

where α is the thermal diffusion of the liquid, L is the characteristic length. This is the general expression for a liquid with a liquid-air interface. With the increase of the Marangoni number, thermocapillary convections can be developed from steady, multi periodic, and turbulent flow patterns.[73-74]

2.1.2 Slip on superhydrophobic surfaces

The key property of a superhydrophobic surface is that it provides a slip to the liquid being in contact with the surface. While the liquid flow velocity at solid surfaces is typically zero, a slip allows for a finite velocity at the surface. This often facilitates the flow, reduces drag or enhances droplet motion. The slip is characterized by the so-called slip length b.[75] It is defined as the distance from the solid substrate surface to where the extrapolated flow velocity vanishes (**Figure 10**). In general, the effective macroscopic boundary condition of a solid surface is described as

$$u_s = b\frac{\partial u}{\partial z} \tag{2-5}$$

where u_s is the tangential velocity at the surface (slip velocity), $\frac{\partial u}{\partial z}$ is the local shear rate perpendicular to the directional flow. For instance, on smooth hydrophobic surfaces, the slip length is only tens of nanometers, while on hydrophilic surfaces, it is undetectably small (nearly zero).[76-77] It is therefore usually neglected.

2.1 Theoretical background
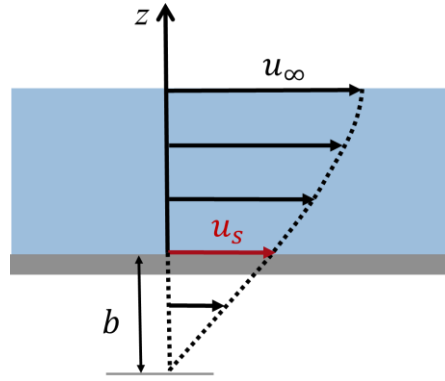
Figure 10. Slip boundary condition of a solid wall in a directional flow u parallel to the wall.
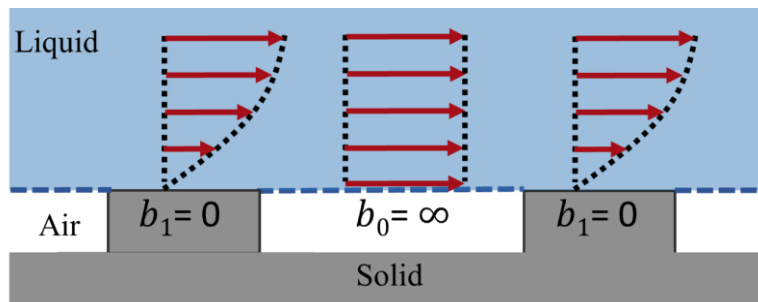
Figure 11. Schematic image of water in the Cassie-Baxter state on a superhydrophobic surface. Liquid-air interface: ideal scenario of a no-shear boundary, $b_0 = \infty$; Solid-liquid interface: No-slip boundary ($b_1 = 0$).

In contrast, the effective slip length on a superhydrophobic surface is much larger due to the presence of the liquid-air interfaces, typically of the order of micrometers.[78-79] In an idealized scenario (**Figure 11**), the corresponding liquid-air interfaces and liquid-solid interfaces can be considered as periodic no-shear boundaries with an infinite slip ($b_0 = \infty$) and no-slip boundaries ($b_1 = 0$).[80] Under these assumptions, Philip *et al.* calculated the effective slip length b of superhydrophobic surface with regular groove structures.[80-82] In the case of the groove structures being aligned parallel to the liquid flow (Longitudinal flow), the effective slip length b_l is expressed as[80-81]

$$b_l = -\frac{L}{\pi} \ln\left(\cos\left(\frac{\pi \phi_g}{2}\right)\right) \tag{2-6}$$

where L is the period of the groove units and ϕ_g is the air fraction at the liquid interface. Assuming the groove structures are perpendicular to the liquid flow (transverse flow), then the expression is given as[82]

16

$$b_{\mathrm{t}} = -\frac{L}{2\pi} \ln\left(\cos\left(\frac{\pi\phi_g}{2}\right)\right) \tag{2-7}$$

The effective slip length in the longitudinal case is twice of the transverse case. Therefore, the orientation of the flows needs to be considered. These two expressions show two extreme cases for liquid flows over a superhydrophobic surface since the flow is least and most hindered by the no-slip conditions (the liquid-solid interfaces). Therefore, for a superhydrophobic surface with the same liquid-air interface fraction but arbitrary morphology, the corresponding effective slip length should be between these two cases.

Later, Schönecker *et al.*[83-84] have considered the non-ideality of the condition at the liquid-air interfaces. This allows the introduction of the influence of the geometry of the micro-structures and the viscosity of the enclosed fluid, i.e., in general air. By modeling liquid flow past a periodic array of rectangular grooves that contain a second immiscible fluid, they further broaden the theoretical expressions to superamphiphobic surfaces where many organic liquids also stay Cassie-state on them. Two normalized slip length $b^* = b/L$ for the longitudinal and transverse flow cases are given by

$$b_l^* = -\frac{\ln\left(\cos\left(\frac{\pi\phi_g}{2}\right)\right)}{\pi + \dfrac{1}{2aD_lN}\ln\dfrac{1 + \sin\left(\frac{\pi\phi_g}{2}\right)}{1 - \sin\left(\frac{\pi\phi_g}{2}\right)}} \tag{2-8}$$

$$b_t^* = -\frac{\ln\left(\cos\left(\frac{\pi\phi_g}{2}\right)\right)}{\pi + \dfrac{1}{2aD_tN}\ln\dfrac{1 + \sin\left(\frac{\pi\phi_g}{2}\right)}{1 - \sin\left(\frac{\pi\phi_g}{2}\right)}} \tag{2-9}$$

where N is the viscosity ratio between two immiscible liquids, $N \sim \mu_1/\mu_2$. D_l is the non-dimensionalized maximum local slip length for longitudinal flow, which is a function of the aspect ratio A of the groove structure as well as the fluidic interface fraction ϕ_g. D_t is the corresponding local slip length for the transverse case. These equations have been widely used in calculating the slip length b for superhydrophobic surfaces, which are in good agreement with expressions for superhydrophobic surfaces with various structures.[85-87]

2.1.3 Thermocapillary flow on superhydrophobic surfaces

Due to the liquid-air interfaces on superhydrophobic surfaces, a temperature gradient on such a surface can induce thermocapillary flows. Equation (2-3) expresses the thermocapillary flow for a liquid with a slip boundary, i.e., a liquid-air interface, but not for the scenario of mixed no-slip – slip conditions on a superhydrophobic surface (**Figure 11**). Therefore, to evaluate the thermocapillary flow on such a surface, an effective boundary condition is required.

Considering a deep channel with a superhydrophobic wall in the longitudinal case, Baier *et al.*[33] showed that the Marangoni stress on the wall is proportional to the slip length b of the superhydrophobic surface. The thermocapillary flow velocity near the superhydrophobic surface, thus can be expressed as:

$$u \sim -\frac{\partial \sigma}{\partial T}\frac{\partial T}{\partial x}\frac{b}{\mu} \qquad (2\text{-}10)$$

This relationship gives a good approximation for the bulk flow induced by the thermocapillary effect for longitudinal grooves. For a superhydrophobic surface with arbitrary geometries, its boundary condition is difficult to be addressed with a simple mathematical expression. Only by equation (2-8) may overestimate the actual thermocapillary flows. For instance, if equation (2-10) is applied to transverse grooves (with the slip length for transverse grooves, $b_t = \frac{b_l}{2}$), the predicted flow velocity is larger than the actual one. Baier has illustrated that this is due to two reasons:[88] Firstly, the temperature gradient at the mixed liquid interface (near the superhydrophobic surface) is not constant in the main thermocapillary flow direction. Secondly, the generation of recirculating flows around each solid protrudes due to the non-uniform temperature gradients at the liquid-air interface. In the transverse case, the flow cells are orientated parallel to the main Marangoni flow, reducing the main flow velocity. However, in the longitudinal case, the convective rolls will not affect much since their orientation are perpendicular to the main flow direction. Therefore, we should keep in mind that equation (2-10) can lead to larger evaluated flow velocities in real cases.

Considering thermocapillary flows between two superhydrophobic surfaces with longitudinal grooves (space apart with a distance $2h$), Yariv [37-38] further derived the Marangoni number in the superhydrophobic system, which is given by

$$Ma = U_M \frac{h}{\alpha} \qquad (2\text{-}11)$$

This expression shows that the geometric parameters of the set-up, e.g., space h and air fraction on the superhydrophobic surface, are vital for obtaining thermocapillary flows with different patterns.

2.2 Experimental

2.2.1 Materials

Tetraethyl orthosilicate (98 %), trichloro(1H, 1H, 2H, 2H-perfluorooctyl)silane (97 %) and Sodium dodecyl sulfate (SDS) were purchased from Sigma-Aldrich, Ethanol absolute, Hexane and iso-propanol and aqueous ammonia (25 %) were from Normapur. Fluorescent polystyrene (PS) tracers of two sizes were used in our system: Micrometer-sized PS beads with average diameter $d \sim$ 2.5 μm, excited at 488 nm and emitting in the range of 515 ~ 660 nm (Life technologies, USA), and sub-micrometer sized PS beads with $d \sim$ 200 nm, excited at 488 nm and emitting in the range of 510 ~ 630 nm (dyed with Nile red, synthesized by a soap-less emulsion polymerization method [89-90]).

Three kinds of surfaces, superhydrophobic soot surfaces ($\theta > 160°$, $\theta_{CAH} < 5°$), superhydrophilic soot surfaces ($\theta < 10°$) as well as superhydrophobic pillar surfaces ($\theta > 150°$, $\theta_{CAH} < 10°$) were prepared. The carbon black (soot), or mixed with PDMS, was used to prepare these surfaces due to its photothermal effect. More details for preparing these surfaces are described below.

2.2.2 Preparation of surfaces with different wettabilities

2.2.2.1 Preparation of superhydrophobic soot surfaces

First, we prepared the superhydrophobic soot surfaces via the approach of soot deposition.[91-92] The photothermal ability of the black soot layer allows a non-uniform temperature distribution to generate on the superhydrophobic surface under light irradiation. However, due to soot particles' inert nature, the deposited soot layer only shows week physical interactions with the substrate. Here, a wax layer was pre-coated on the substrate to enhance the adhesion between the soot layer and the substrate. The fabrication process is schematically illustrated in **Figure 12**.
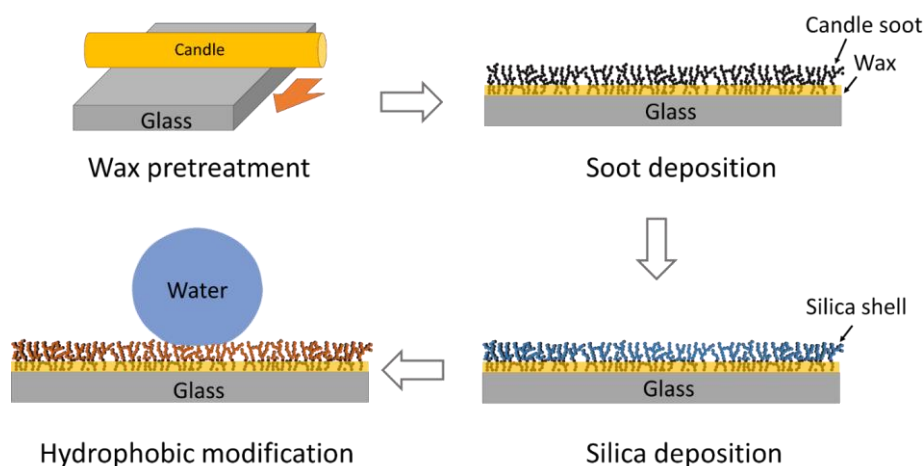
Figure 12. Schematic of the preparation of superhydrophobic soot surfaces.

The glass slides (dimensions 25 cm×25 cm; thickness 170 ± 5 μm, Marienfeld Superior) were first ultrasonically cleaned in a bath of ethanol, acetone, and isopropanol for 5 min, respectively, to remove contaminations on glass slides. After the cleaning procedure, by rubbing a candle on the substrates back and forth for several times, a thin layer of wax was pre-coated on the slide. Then, the slide was held over a candle flame to allow candle soot (soot particles with average diameter $D \sim 45 \pm 5$ nm) deposited and gradually formed a thin soot layer. The average thickness of the soot layer $h \sim 30$ μm. The soot layer was partly embedded in the wax coating, allowing the soot layer to adhere to the glass surface.

To enhance the robustness of the soot layer, a following stepwise chemical silica deposition approach was done.[93] A chemical vapor deposition approach (CVD) was firstly established by placing the soot-deposited slides in a desiccator with two vials. One vial is filled with 2 mL ammonia and the other is filled with 2 mL tetraethyl orthosilicate (TEOS). Then the desiccator was sealed for 48 h. In the desiccator, hydrolysis and condensation of TEOS occurred and formed silica under the ammonia atmosphere. Then the soot-based slides were taken out and had been covered with silica; Then, an additional Stöber reaction was done by immersing the slides in a staining dish with a solution of 18 mL ethanol, 2 mL silicate and 1.5 mL ammonia. The dish was placed on a shaker with a rotation speed of 150 rpm/s for 4 h. This procedure further deposits silica on soot-based surfaces to enhance its mechanical stability. Notably, after this stepwise silica deposition procedure, the soot layer was not burnt out (which was reported by previous works [91-92]) but remained to generate non-uniform temperature distributions on modified surfaces under light illumination.

After preparing the soot surfaces with micro/nano-structures, a further hydrophobic modification was done by placing the soot surfaces in a desiccator with a vial filled with Trichloro(1H, 1H, 2H, 2H-perfluorooctyl)silane (about 200 μL). Then the desiccator was sealed and vacuumed for about 30 s until the pressure inside < 200 mbar. The samples were taken out after 3 h. With this procedure, superhydrophobic soot surfaces were obtained (with water contact angle $\theta > 160$ ° and contact angle hysteresis $\theta_{CAH} < 5$ °.

2.2.2.2 Preparation of superhydrophilic soot surfaces

Superhydrophilic soot surfaces were prepared for contrast experiments. The preparation procedures of the soot-based layer are the same as described before. The difference is that after the stepwise silica deposition, no further chemical modification is needed since the silica shell showed hydrophilic nature themselves. It allows the surfaces to be hydrophilic ($\theta < 10$ °) while presenting the same heat conductivity and surface roughness compared with the superhydrophobic soot surfaces.

2.2.2.3 Preparation of superhydrophobic surfaces with pillar structures

To prepare a superhydrophobic surface with a more considerable slip length, micro-pillared surfaces fabricated by PDMS-Carbon black mixtures were prepared on glass slides. The schematic preparation procedure is shown in **Figure 13**.
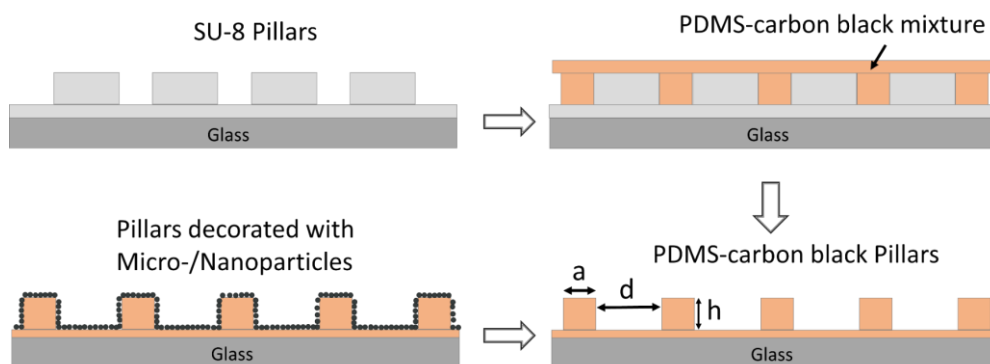
Figure 13. The schematic of the preparation of PDMS-carbon black pillar structures on a glass substrate.

Figure 14. SEM images of pillar surfaces deposited with micro-/nanoparticles (Pillar size $a =10\ \mu$m, distance $d =20\ \mu$m). (a) Silica nanoparticles with a diameter of 40 nm; (b) PS microparticles with an average diameter around 1 μm.

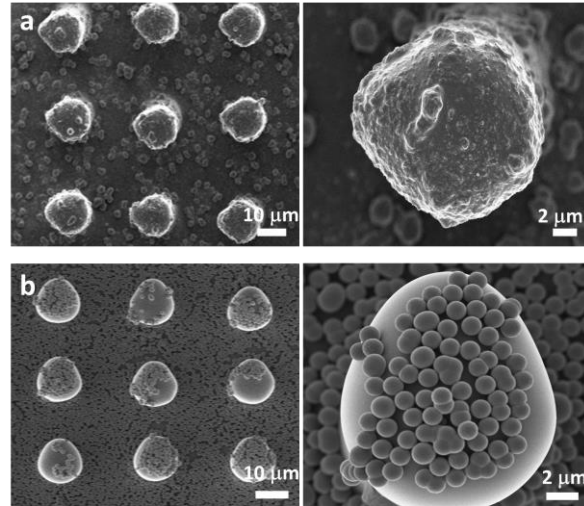The micro-pillar master was fabricated by a photolithographic process. An epoxy-based negative photoresist SU-8 was coated on a clean glass slide by a spin coater for 30 s (a speed of 1500 rpm/s). The resulted coating thickness is about 30 μm. Then the coated sliders were placed on a hotplate (set as 65 °C) for 3 min and a hotplate (85 °C) for 10 min, then placed on the 65 °C hotplate for another 30 min, respectively. This soft baking procedure was done to remove the solvents in the coating and improve the adhesion between the un-crosslinked SU-8 coating and the glass substrate. Then the slide was cooled down at room temperature before the exposure procedure. Afterward, the slide was covered by a photomask (round patches, with a diameter of $a = 10\ \mu$m and spacing $d = 20\ \mu$m) and transferred to the lithography chamber. Under UV light exposure for 14 s (by a UV Enhanced Silicon Photodetector with a Hg lamp, the exposure dose ~0.25 J/cm^2, $\lambda = 365$ nm), the SU-8 at the exposed areas was cross-linked. To improve the mechanical ability of the cross-liked coating, a step-wise hard-baking process was done subsequently: the slides were placed on a hotplate (65 °C) for 5 min and then on another hotplate (95 °C) for 10 min, then they were transferred on a non-heated surface for more than 30 min to cool down. After this post-baking procedure, the develop process was done by placing the cooled slides in a bath of the commercial developer for 2 min, and then with a gently shaking for 1 min before quickly transferred to 50 mL isopropanol for 20 s. Hence, a master with SU-8 pillar arrays was obtained with micro-pillar dimensions of $a = 10\ \mu$m, $d = 20\ \mu$m, $h = 30\ \mu$m.

Then a polydimethylsiloxane (PDMS)-carbon black mixture mold replica from the SU-8 master was obtained. The commercial un-crosslinked silicone elastomer was first mixed with the curing agent (SYLGARD 184, Dow Corning) and carbon black (with an average particle size ~42 nm, Thermo Fisher) in a mass weight ratio of 500: 50: 1. To disperse carbon black evenly in the viscous PDMS fluid, they were first dispersed in hexane and then dropped into the mixture ---un-crosslinked silicone elastomer and the curing agent in a dropwise manner. Then intensive shaking was applied to the mixture. The mixture was poured in an open chamber overnight to allow the hexane to evaporate before use. Afterward, we poured the PDMS-carbon black mixture on the SU-8 master surface. Then the sample was placed in an oven at 60 °C for 6 h to allow the PDMS mixture to be cured. This process creates pillar arrays ($a \sim 10\ \mu$m, $d \sim 20\ \mu$m, $h \sim 30\ \mu$m) on the PDMS-carbon black layer.

To create hierarchical structures on the micropillar surfaces, the pillars were decorated with micro/nano-particles. Two preparation approaches had been done.

The first approach was realized by depositing a layer of closely packed PS microparticles on the pillar surface. Closely packed particle monolayers were obtained by self-assembly at the water-air interface.[94] First, the PDMS-pillar surfaces was placed in a bath of 50 mL MilliQ water (note that the top of the pillar surface should be lower than the water surface). Then the PS particle dispersion (average particle diameter $d = 1.1\ \mu$m, a concentration of 1 wt% in ethanol) was added dropwise in the chamber. The micro-particles would either settle at the water liquid-air interface or disperse in the bulk liquid. Then by dropping the SDS aqueous solution (a concentration of about 1 wt%) in the water reservoir, due to the Marangoni effect caused by the SDS surfactants, the particles that freely settled at the interface were repelled from the region with high SDS concentration (low surface tension), thus formed a closely-packed particle monolayer at the liquid surface. Then the water subphase was sucked by a needle from the bottom to lower its surface level. As the liquid surface descended, the particle monolayer on the liquid surface ultimately settled on the pillar surfaces. Afterward, a hydrophobic modification of the microparticle-decorated pillar surface was done to obtain superhydrophobic surfaces ($\theta > 155°$, $\theta_{\mathrm{CAH}} \sim 15°$). An alternative way to prepare the superhydrophobic particles-decorated surface was done by directly spraying a commercial agent on the pillar surface from a distance ~ 20 cm (soft 99, Glaco Mirror Coat 'Zero', an alcohol-based dispersion of silica nanoparticles coated with a silane hydrophobic agent)[95]. With this procedure, this surface becomes hydrophobic with a water contact angle $\theta > 150°$ and a contact angle hysteresis $\theta_{\mathrm{CAH}} < 10°$.

Additionally, the morphology of these surfaces was visualized by a scanning electron microscope (SEM, low voltage LEO 1530 Gemini, Germany, and SU8000, Hitachi, Japan). From the SEM images (**Figure 9** and **Figure 14**), slip lengths[83-84] on superhydrophobic surfaces constructed with soot layer and micro-pillars can be calculated by evaluating their micro/nano-meter structures. On superhydrophobic soot surfaces with an evaluated protrude with an average diameter of $a = 0.2$ μm, and space $d = 1$ μm, the corresponding slip length was calculated to be $b \sim 0.22$ μm; On superhydrophobic pillar surfaces with pillar diameter of $a = 10$ μm and space $d = 20$ μm, a slip length $b \sim 3.2$ μm was estimated.

2.2.3 Experimental setup

The prepared surfaces were placed above water reservoirs in circular μ-Slide cells (with a height $H = 1$ mm, diameter $D = 21$ mm), as shown in **Figure 15**. To non-uniformly heat the water reservoir, a focused laser with an emission wavelength of $\lambda_{exe} = 488$ nm (cw-diode laser, Cobolt 06-01 series) was used to illuminate the photothermal soot-based surfaces. The laser beam that arrived at the substrate was measured with a power of $Q_{\text{measure}} \geq 10$ mW by a laser power meter (FieldMaxII-TOP, Coherent Inc., USA) and a spot diameter of $\varnothing \sim 350$ μm. The liquid cell was observed by a confocal laser scanning microscope (Leica LCS-SP8, Germany), equipped with a water objective ahead (Leica HCX IRAPO L 25x 0.95 W, with a free working distance of 2.5 mm). Two sizes of fluorescently-labeled PS beads, i.e., microbeads ($d \sim 2.5$ μm, with a concentration of $c \sim 1.2 \times 10^6$ /mL) and sub-micrometer beads ($d \sim 200$ nm, $c \sim 1 \times 10^6$ /mL), were used as tracers to visualize the flows in the liquid cell. A 488 nm argon laser (DPSS 561-10, with the power of 5 mW) from the objective of the confocal microscope was used to excite the liquid cell, and a fluorescent range between 510 and 630 nm was selected to detect the fluorescent particles. The experimental setup is shown in **Figure 16**.
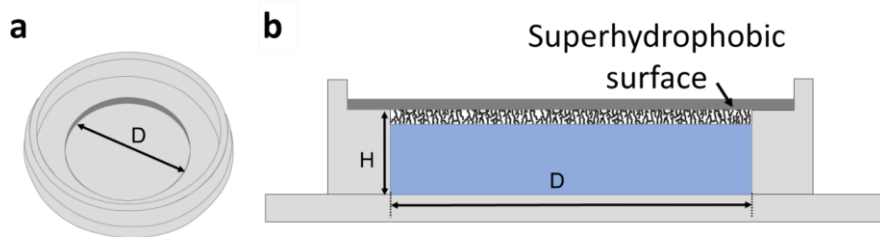
Figure 15. The schematic of the experimental liquid cell. (a) A circular μ-Slide cell with a hydrophilic polymer bottom surface (the bottom surface's thickness: 180 μm; reflective index: 1.52); (b) Side view of the liquid cell. The superhydrophobic surface is placed on top of the cell (dispersed with tracer particles).
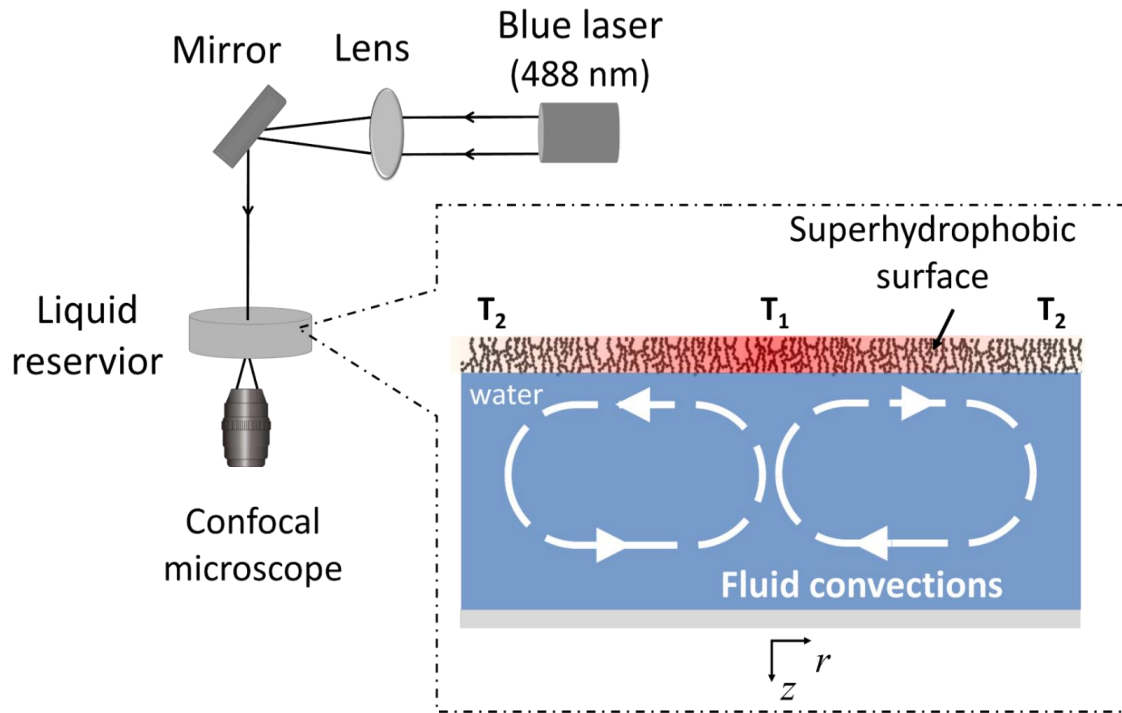
Figure 16. Schematic of the experimental setup. A superhydrophobic surface fabricated with a soot layer is placed above the observation cell. The photothermal effect of the soot allows the liquid phase to be in contact with the surface to be non-uniformly heated and generate convective flows. A confocal microscope with a 25x water objective is used for recording flows.

2.2.4 Temperature measurements

The temporal temperature distributions at solid surfaces were recorded by a thermal-infrared camera (IR 1.0/60 LW JENOPTIK, InfraTec, Germany). In contrast to conventional optical cameras, the infrared camera is sensitive to invisible infrared lights emitted from most objects above the absolute temperature (wavelength from 900 nm to about 14 μm). According to the Stefan-Boltzmann law,[96] the total radiated energy W is calculated to be $W \sim \sigma T^4$, where σ is a constant, $\sigma \sim 5.67 \times 10^{-8}$ W/m$^2 \cdot$K^4. The amount of the infrared radiation increases with temperature T. The infrared camera can convert the infrared radiated energy into a visual image (thermogram), which allows us to measure the temperature distribution across an object or scene in a non-contact manner. The infrared camera is installed with a 0.5$\times$ converter lens ahead (VarioCAM® HD head 680s, InfraTec, Germany). Its focal length is 30 mm (with a resolution of 32 μm). This camera can measure temperatures in the range of -20 to 120 °C (with a resolution of 0.02 °C). The size of the captured images is 640×480 pixels, with a spatial resolution of approximately 42 μm. Besides, the image sequences were recorded at 2 fps.

2.2.5 Liquid flow observations

Fluorescent images in *xyt* and *xzt* scanning modes, corresponding to planes parallel to the upper horizontal surface (top view) and in the vertical direction (side view) at successive time intervals (**Figure 16**), were recorded by confocal microscopy. In addition, a discrete stepwise *xytz* scanning mode, *i.e.,* times series of *xy*-planes taken at different focal planes in the vertical *z* (axial) direction (each of the step size $Z_{\text{step-size}} = 3$ μm), was also applied to obtain 3D information of tracer motions over time (**Figure 17**). The fluorescent images were recorded with a size resolution of 512×512 pixels (spatial resolution of 0.73 μm) at 15 fps. Each measurement was taken at least 500 frames and repeated at least three times to ensure repeatability and statistical analysis.
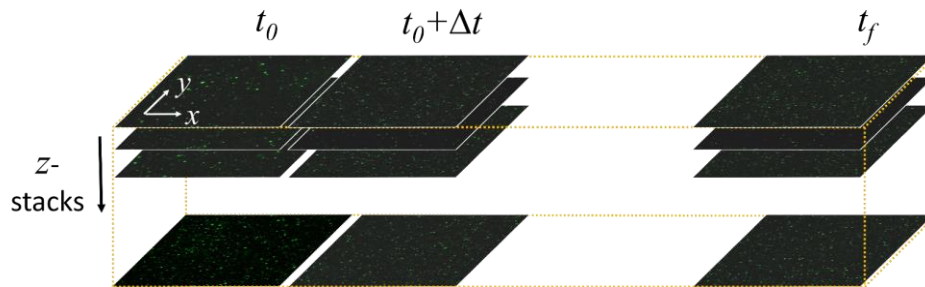
Figure 17. Discrete stepwise *xytz* scanning mode. Time series at different focal positions (along *z*-axis) were taken to analyze the trace motions in the liquid cell. The time interval between each frame Δt =0.68 s; Green dots: fluorescent PS microspheres (2.5 μm, excited at 488 nm and emitting in the range of 515 ~ 660 nm).

One thing to note, the smallest step size in z-direction was set according to the optical section thickness (d_z) determined by the measuring condition, which is given by,[97-98]

$$d_z = \sqrt{\left(\frac{\lambda_{exc} \cdot n}{NA^2}\right)^2 + \left(\frac{n \cdot \sqrt{2} \cdot PH}{NA}\right)^2} \sim \frac{n \cdot \sqrt{2} \cdot PH}{NA} \qquad (2\text{-}12)$$

Here, *NA* is the numerical aperture of the objective, *NA* =0.95; λ_{exc} is the wavelength of the incident laser from the confocal microscope, λ_{exc} =488 nm; n is the refractive index of the medium (between the coverslip and the objective), n =1.33 for water; *PH* is the size of the pinhole, PH =4d_{air} ≈2.5 μm (where d_{air} is the Airy unit, d_{air}= 1.22λ/NA ~ 627 nm). Thus, d_z is estimated to be about 5 μm.

2.2.5.1 Flow analyzing

The data saved as '.lif' formats were first resaved as 8-bit grayscale image sequences in '.tif' formats within the software package ImageJ (National Institutes of Health, Maryland, USA).

The flow velocity distribution in the observation cell was obtained by analyzing the mean velocity of particles in *xy*-planes with the MTrackJ plugin for ImageJ. "The MTrackJ plugin was used to detect and manually track the moving particles in the successive frames via their pixel coordinates." The measurement details are described below: First, an image sequence (100 continuous images) recorded in the *xyt* or *xytz* scanning mode by confocal microscopy was first uploaded in ImageJ. Then we applied the experimental parameters in the offsetting window of the MTrackJ plugin, *e.g.,* reference length (spatial resolution 0.73 μm/pixel) and time intervals (0.068 s). Afterward, the particles in the first image were marked, and their trajectories were automatically created in the image sequence. Therefore, the velocity of each particle can be obtained from its trajectory. For each velocity data point, it is obtained by averaging velocity values of at least 20 particles.

One thing to note, the *xyt* or *xytz* scanning mode allowed us to record the motions of the tracers over time *t* in multiple 2D *xy*-planes (with different *z*-depths). Therefore, the velocity values of the tracers were obtained by only considering their motions in the direction parallel to the upper surface (in *xy*-planes); their velocity components in the vertical direction (z-direction) were not considered. Even though at the selected observation regions (near the upper surface, but with a distance *r* away from the heated region), the tracers were more likely to transport in the direction parallel to the upper surface, we should keep in mind that these tracers may still transport in z-direction in the liquid cell (3D motion in *xyz*- space). This is also the reason why some tracers disappeared from the focus plane during recording by confocal microscopy.

The velocity distribution in the fluorescent images was processed using the PIVlab tool for MATLAB (PIVlab plugin, 2018b, MathWorks).[99-100] It performs a cross-correlation analysis between continuous image frames, divided into different interrogation areas (IA) to obtain the mean displacement vector for each IA. The processing details are described as below: First, by importing every 20 continuous frames of one image sequence (100 images) to the PIVlab, "an ROI region (region of interest, with a dimension of width 480 pixels and height 480 pixels) was drawn in the first image and automatically applied to the following images. Then the images were pre-processed by selecting the contrast-limited adaptive histogram equalization (CLAHE, 20 pixels), high-pass pre-analysis filters (15 pixels), and the contrast stretch (0.01-

0.32) to improve the image resolutions. We selected the Fast Fourier transform window deformation (FFT) cross-correlation algorithm and defined the IAs as a decreasing sequence of 240×120 pixels, 120×60 and 60×30 pixels to analyze the motions of the particles in the continuous image frames." The first pass uses relatively large IA (240×120 pixels) to calculate the displacement with a robust cross-correlation and good signal-to-noise ratio. However, it gives a low vector resolution. Thus following IAs with small areas were set to increase the vector resolutions. After these setting processes, images were correlated, and velocity vectors are validated (green arrows, as shown in **Figure 22**). By further selecting the "velocity limits to filter outliers, the out-of-range velocity vectors were deleted, and the missed vectors were replaced with values interpolated from nearest neighbors" (orange arrows). Notably, due to the low concentration of traces ($\sim 1.2 \times 10^6$/mL) in this system, a small IA would significantly increase the number of error correlations and noises. Therefore, the IAs were set to be larger than 30x30 pixels.

2.3 Temperature distribution observation by Infrared camera

2.3.1 On soot-based surfaces (in air)

The soot surface can be considered as a black body (an idealized opaque and non-reflective body) due to its excellent light absorbability. [101-102] The optical transitions of the pi-bands of black carbon particles and the micro/nanostructures of the soot surface help to trap the incident light. When a focused laser beam irradiates on the soot surface for 60 s (with a spot diameter $\varnothing \sim 350\,\mu$m), an axisymmetric temperature distribution generates on the solid substrate due to the photothermal effect. When the surface is exposed to the air, a sharp and narrow axisymmetric temperature distribution generates on the soot substrate, $\Delta T \sim 8\,°$C within the field $-1000 \leq r \leq 1000\,\mu$m. (**Figure 18**) The temperature profile curve on the soot surface displays a Gaussian-like shape corresponding to the laser beam (**Figure 18b**).
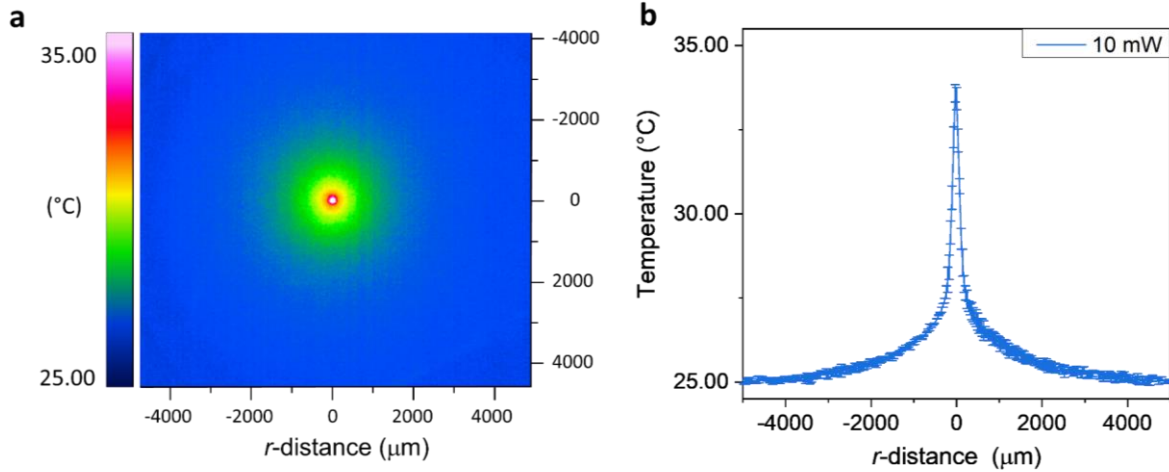
Figure 18. "Temperature distribution on a soot surface when irradiated by a blue laser" (exposed to air). (a) Infrared image of the soot surface; (b) Temperature profile curve obtained from (a). ($\lambda_{\text{laser}} = 488$ nm, $Q_{\text{laser}} = 10$ mW, $d = 350$ μm, soot layer thickness: 25 ± 5 μm).

2.3.2 In the liquid layer

When the soot surface is placed on a water reservoir under the same irradiation condition, the soot surface exhibits a broadened and flatten temperature distribution (**Figure 19a**). The water phase being in contact with the soot surface is also heated up. The temperature distribution in the liquid phase thus can be simplified into two directions: parallel the upper interface (ΔT_r) in r-direction; and perpendicular to the interface (ΔT_z) in z-direction (**Figure 19b**).

Close to the upper surface (in r-direction), a temperature gradient of $\frac{\partial T}{\partial r} \sim 0.25$ °C/mm is obtained. The temperature difference between the upper and bottom surface (in z-direction) is $\Delta T_{r,z} = T_{r,z=0} - T_{r,z=H} \sim 0.1$ °C. $\Delta T_{r,z}$ is the temperature difference with a horizontal distance r from the heated spot. Thus, heat conduction through the liquid phase is evident. A more evident temperature gradient is illustrated in r-direction, and it is expected to induce a Marangoni flow. Thus, we mainly studied the thermally-induced flows in this direction.

2.3 Temperature distribution observation by Infrared camera
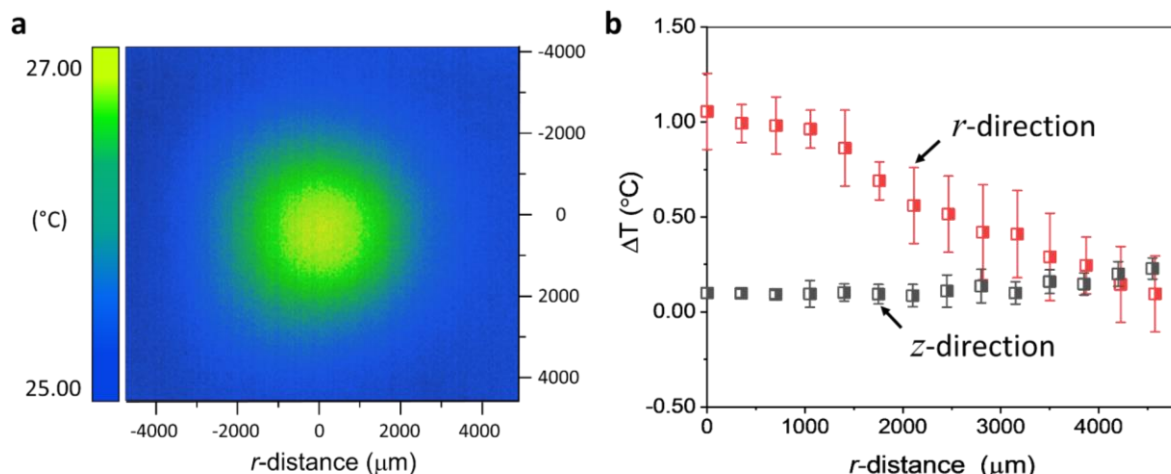
Figure 19. Temperature distribution in the liquid cell. (a) Infrared image showing the temperature distribution near the upper superhydrophobic soot surface; (b) Measured temperature differences of the liquid phase: r-direction: relative to the room temperature T_0 ($\Delta T_r = T_{r,z=0} - T_0$, red); z-direction: temperature differences between the top and bottom of the liquid layer ($\Delta T_{r,z} = T_{r,z=0} - T_{r,z=H}$, grey). The error bars are obtained from the standard deviation of the temperature values in at least three measurements. Laser: $\lambda_{\text{laser}} = 488$ nm, $Q_{\text{laser}} = 10$ mW, $\phi = 350\,\mu$m.
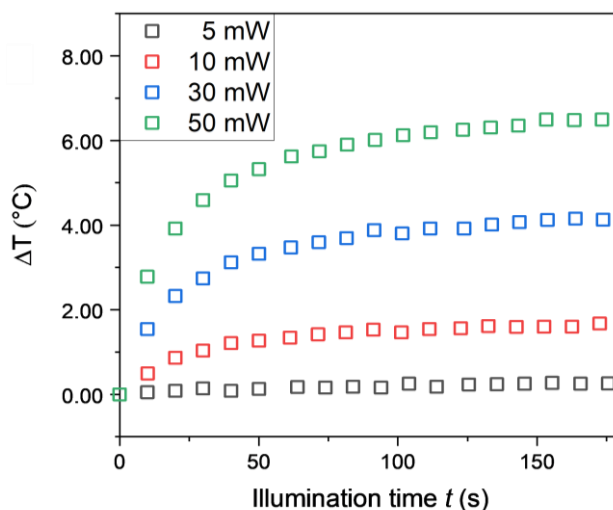
Figure 20. Temperature evolution curve of the laser irradiated region on soot surfaces ($\lambda_{\text{laser}} = 488$ nm, $\phi = 350\,\mu$m).

Figure 20 shows the temporal temperature evolution at the irradiation area on the soot surface under laser illumination with different powers. The temperature values change rapidly and stabilize after 60 s. Its evolution also shows a more pronounced variation (> 1 °C) when

30

$Q_{\text{laser}} \geq 10$ mW and increases with laser intensity. However, it should be noted that the laser power should not exceed $Q_{\text{laser}} = 30$ mW. In this case, bubbles continuously generate on the superhydrophobic soot surfaces and deform the liquid interfaces, reducing the measurement accuracy. Accordingly, a laser with power $Q_{\text{laser}} = 10$ mW was used to illuminate the soot surfaces in the following experiments, and the measurements were performed after illuminating the systems for at least 60 s to obtain stabilized data.

2.3.3 Near different surfaces

Figure 21 shows the temperature distributions of the liquid phase near three structured surfaces: superhydrophobic soot and superhydrophilic soot surfaces, as well as superhydrophobic pillar surfaces. The temperature distributions on three surfaces show a similar trend under the same illumination condition. On superhydrophilic soot surfaces, $\frac{\partial T}{\partial r} \sim 0.30$ °C/mm, which is slightly higher than superhydrophobic soot surfaces, especially near the irradiation spot area ($r \leq 500$ μm). This difference is presumably caused by the conductivity difference due to surface wettability. On superhydrophilic surfaces, heat is more easily transferred to the liquid phase since the water phase has a larger contact area with the heated substrate (Wenzel state). On superhydrophobic pillar surfaces, the corresponding temperature distributions are relatively moderate, $\frac{\partial T}{\partial r} \sim 0.23$ °C/mm.
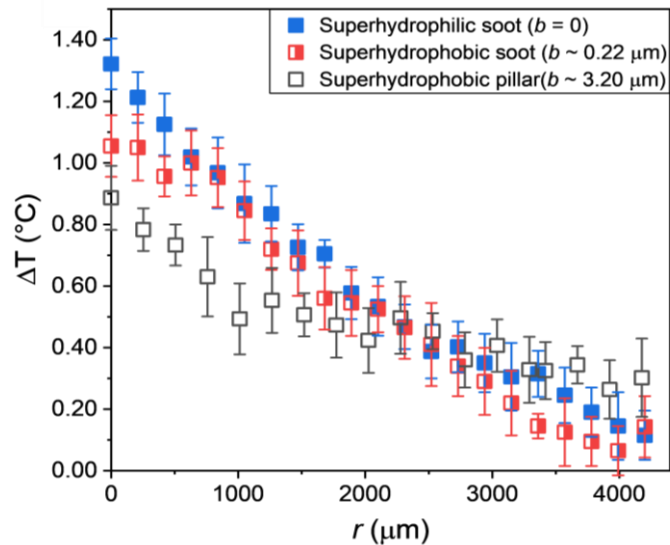
Figure 21. Temperature distribution near the surfaces with different wettability (Laser properties: $Q_{\text{laser}} = 10$ mW, $\lambda_{\text{laser}} = 488$ nm, $\phi = 350$ μm).

2.4 Observation of convective flows by confocal microscopy

With this axisymmetric temperature field in the liquid phase, one can expect liquid flows on superhydrophobic surfaces. To visualize the flows in the liquid phase, fluorescent PS particles were dispersed in the liquid phase, and their motions were recorded by confocal microscopy. Flow patterns in three regions of interest (marked with rectangles of different colors), i.e., near the upper surface away from the heated region ($r = 500\ \mu$m, $z \sim 0$, red), near the upper surface in the heated region ($r \sim 0$, $z \sim 0$, yellow) and near the bottom surface ($r \sim 0$, $z \sim 1000\ \mu$m, purple), are shown in **Figure 22**.
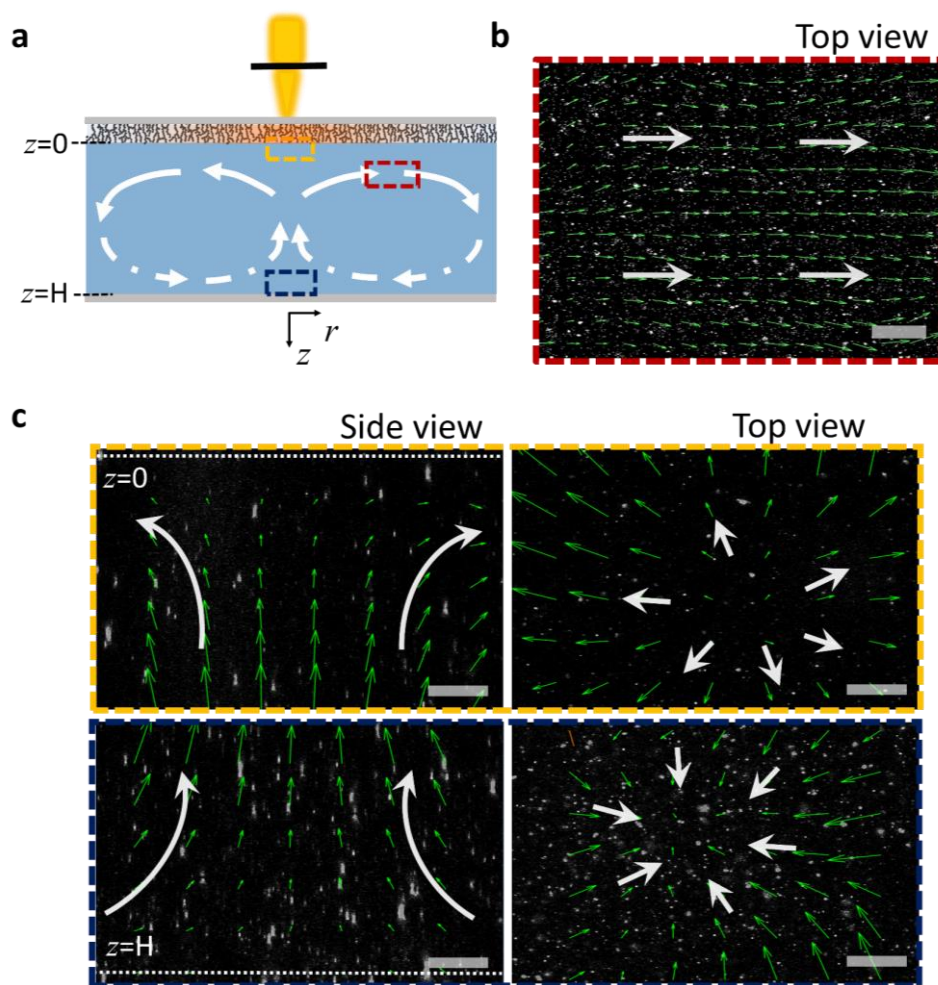
Figure 22. Optothermal-induced convective flows in the liquid layer. (a) Schematic of the cross-section of the fluid cell. Three regions of interest are marked with colored-rectangles. (b)(c) Images of fluorescent particles (white dots) with superimposed velocity vector profiles (green arrows). Scale bars: 50 μm.

Near the upper superhydrophobic surface ($r = 500$ μm, $z\sim 0$), the dispersed traces transport towards the direction of temperature decreases (**Figure 22b**). Near the upper surface in the heated region ($r\sim 0$, $z\sim 0$), the traces are driven upward and then transport axisymetrically outwards to the cold regions. When we lower the focus plane to the bottom surface ($r\sim 0$, $z\sim 1000$ μm), reversed flows are observed (**Figure 22c**). Without laser illumination on the set-up, the dispersed particles move randomly (contribute from Brownian motion) instead of a directional way. Therefore, asymmetric convective flows are formed in the liquid cell. Compared with the optothermal devices that usually been reported, *e.g.,* plasmonic nanostructured surfaces,[103-104] this superhydrophobic system shows the possibility of triggering flows in continuous liquid phase with a small temperature variation of about 0.1 °C/mm.

2.5 Physical modeling of the convective flows

In order to identify the possible mechanism of the thermally-induced flows on superhydrophobic surfaces, numerical simulations were performed by the COMSOL Multiphysics Software 5.4a (Comsol, Inc., Stockholm, Sweden) with an asymmetrical 2D rectangular geometry corresponding to the experimental fluid cell (zr-plane, r set to 20 mm and z defined to 1 mm) (**Figure 22a**). The "Laminar flow" module for fluid dynamics and the "heat transfer in fluid" module for thermal physics were applied.

2.5.1 Governing equations

Two thermally-induced effects in triggering flows in the liquid cell, the thermocapillary effect and the gravitational effect (or buoyancy effect), were investigated by applying the Navier-Stokes' equations in the modeling. For incompressible liquids, a Boussinesq approximation is applied. The stationary momentum and mass conservation equations are written as

$$\nabla \boldsymbol{u} = 0 \tag{2-13}$$

$$\rho \left(\frac{\partial \boldsymbol{u}}{\partial t} - (\boldsymbol{u}\nabla)\boldsymbol{u} \right) = \mu\nabla^2\boldsymbol{u} - \nabla p + \boldsymbol{F} \tag{2-14}$$

where $\boldsymbol{u}$ is the velocity field; ρ is the density of the liquid, μ is the corresponding dynamic viscosity; p is the liquid pressure, and $\boldsymbol{F}$ represents external body forces per unit volume applied to the liquid. In our system, the only body force to be considered is gravity, which is related to the temperature-dependent density. $\boldsymbol{F} = \rho_0 \boldsymbol{g}\beta(T - T_0)$, where ρ_0 and β are the

density and thermal expansion coefficient of liquids at a reference temperature T_0, and $\boldsymbol{g}$ is the gravitational acceleration.

The heat equation is written as

$$\rho c_p \boldsymbol{u} \cdot \nabla\mathrm{T} = k\nabla^2 T \tag{2-15}$$

where c_p is the specific heat capacity of the liquid, k is the thermal conductivity of the liquid. For water, some of its thermophysical property values at room temperature are: $\mu = 0.890$ mPa·s, $\beta = 2.570{\times}10^{-4}$ K^{-1}, $c_p = 4.182$ kJ/(kg·K) and $k = 0.608$ W/(m·K). They are considered constant with the variation of temperature, except for the surface tension and density. These two parameters may play a role in triggering flows in our system.

These equations were solved by COMSOL. In order to identify the roles of the two mentioned parameters in triggering thermally-induced flows, three different scenarios are theoretically defined: (1) Thermocapillary effect on the superhydrophobic surface; Neglect the gravitational effect in the liquid. This is the classical model reported by Baier *et al.*.[8,105-106] (2) No thermocapillary effect but only "slip" on the superhydrophobic surface; Gravitational effect in the system. (3) Thermocapillary effect on the superhydrophobic surface; Gravitational effect in the liquid.

At small dimensions, the gravitational effect is commonly assumed not to be considered, especially in the theoretical models of thermocapillary flows on superhydrophobic surfaces that have been reported.[37-38, 105-106] However, in our system, we will show that the gravitational effect also plays an essential role in triggering flows.

2.5.2 Boundary conditions

The experimental temperature gradients are first input to the boundaries (**Figure 23**). To illustrate the heated region in the cell, Boundaries 1 and 2 were applied with the experimental temperature gradients. Other boundaries were set with the reference temperature $T_0 =25$ °C. Then, the boundaries are defined with no-slip walls except for boundary 1. Boundary 1 represents the liquid interface being in contact with a superhydrophobic surface.
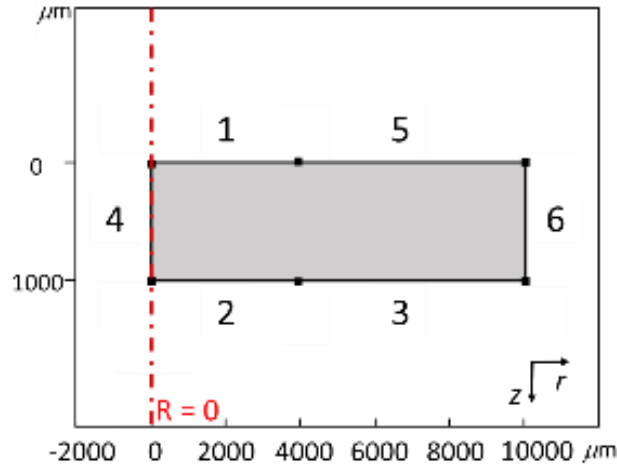
Figure 23. "Denomination of the boundaries in the simulation model. Boundaries 1 to 6 are defined by different boundary conditions."

In case (1), a condition for the thermocapillary velocity at boundary 1 is required. Typically, a Navier slip condition (see Equation (2-5)) is applied at the boundary for directional flows over superhydrophobic surfaces, e.g., pressure or shear-driven flows. However, for thermocapillary flows on superhydrophobic surfaces, there are no general boundary conditions. A simplified expression was reported by Baier *et al.*[33] for superhydrophobic surfaces with longitudinal grooves (Equation (2-10)). The velocity component parallel to the surface is expressed as $U_w = -\frac{\partial \sigma}{\partial T} \frac{\partial T}{\partial r} \cdot \frac{b}{\mu}$, with r the coordinate along the grooves. In this case, the gravitational force was assumed to be negligible; thus, the term $\boldsymbol{F} = 0$ in equation (2-14).

This equation is more for ideal cases in the longitudinal groove surfaces. For superhydrophobic surfaces with different morphologies rather than longitudinal groove structures, their boundary conditions are much more complicated.[38] Without an appropriate boundary condition, the simulated flow velocity may be overestimated. For instance, in the transverse case, the obtained velocity may overestimate, especially for superhydrophobic surfaces with large liquid-air interface fractions. In our experiments for a superhydrophobic soot surface, the geometry of the soot surface is irregular and complicated.[107] No exact boundary condition can be applied for such a surface. Therefore, we apply the equation for longitudinal groove surfaces as the closest condition and keep in mind the possibility of overestimating the Marangoni flows.

On a soot surface with irregular structures,[107] as shown in chapter 2.1.2, its effective slip length b cannot be exactly determined. b must be between the values of the transverse and longitudinal grooves.[80-82, 84] From the SEM image of the soot surface (**Figure 9**), with a

characteristic diameter of $a = 200$ nm on the soot particle-aggregated protrusions and a space of $d = 1$ μm between the protrusions, the corresponding effective slip length was estimated in the range of $0.22 < b < 0.45$ μm. On a superhydrophobic pillar surface with pillars diameters of $a = 10$ μm and spacing $d = 20$ μm, the corresponding effective slip length was estimated to be $3.2 < b < 6.4$ μm.

In contrast to case (1), the gravitational term $\boldsymbol{F}$ is "switched on" in case (2) and case (3). In Case (2), boundary 1 is applied with a Navier slip velocity, $\boldsymbol{u} = b\frac{\partial u}{\partial z}$ (Equation (2-5))[108] to show the "drag reduction" on the superhydrophobic surface. Case (3) assumes the model with the Marangoni shear stress at boundary 1, the same as the case (1). Thus, boundary 1 is defined with a Marangoni flow $U_w = -\frac{\partial \sigma}{\partial T}\frac{\partial T}{\partial r} \cdot \frac{b}{\mu}$ (see Equation (2-10)). The boundary conditions of the model in case (1) and (3) are listed in **Table 1**.

Table 1. "Boundary conditions for simulating thermocapillary-triggered flow in the setup. The experimentally measured temperature distributions are used as an input on boundaries 1 and 2. They are simplified as linear functions. Boundaries 3, 5 and 6 are no-slip walls with the ambient temperature $T_0 = 25$ °C. Boundary 4 is the symmetry axis of the simulated axisymmetric geometry."

Boundary	1	2	3, 5, 6
Condition	Superhydrophobic surface	No-slip walls	
u	$u_r = -\frac{\partial \sigma}{\partial T}\left(\frac{\partial T}{\partial r}\right) \cdot b;$ $u_z = 0$	$u_r = u_z = 0$	$u_r = u_z = 0$
T	$T_1 = T_0 + 1\text{K} - r\left(\frac{\partial T}{\partial r}\right)$	$T_2 = T_0 + 0.9\text{K} - r\left(\frac{\partial T}{\partial r}\right) \cdot 0.9$	$T = T_0$

2.5.3 Modeling results

By applying the experimental temperature values in the simulation (**Figure 19b** for the superhydrophobic soot surface), results according to the cases mentioned above are shown in **Figure 24**.
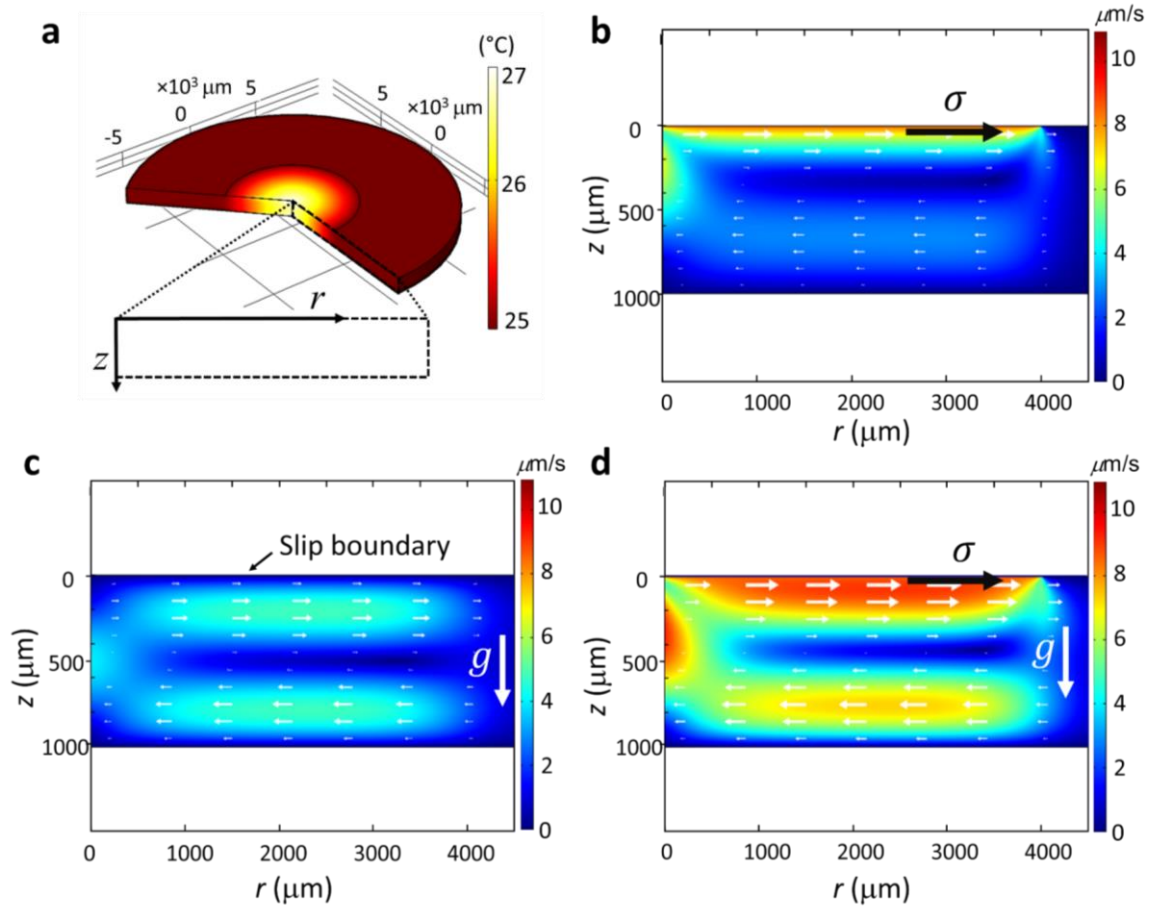
Figure 24. Computational simulations of two-dimensional fluid convections. (a) The 2D geometry for modeling. The color map denotes the temperature distribution in this geometry; (b) Thermocapillary convections superposed with flow vectors originated by the Marangoni stress σ at the upper boundary; (c) Natural convections in the presence of a gravitational field (g and a "slip" boundary); (d) Fluid convections caused by the Marangoni and the gravitational effect (σ, g). The color illustrates the magnitude of the velocity of the flows. Dark red and blue show the corresponding maximum and minimum velocity values, respectively.

Figure 24a shows the axisymmetric temperature distribution in the simulated system. In these three cases, axisymmetric convective flows are generated, which however, differ in their velocity distributions. In case (1) of pure thermocapillary flows (**Figure 24b**), the most vital flow generates near the upper boundary ($u_{max} \sim 8 \ \mu$m/s at $Z \sim 0$) and drags the rest of the bulk liquid. The flow velocity shows a decrease with depth z. Additionally, backflows are generated in the lower portion of the liquid phase since the system is closed. For case (2) that only considered the gravitational effect (**Figure 24c**), the convective flows are more evenly distributed in the water reservoir. The maximum velocity appears at the region $z \sim \frac{1}{4}$ of the liquid layer ($u_{max} \sim 5.5 \ \mu$m/s at $z \sim 250 \ \mu$m). Near the top "slip" boundary, the corresponding

flow velocity $u_{z=0}\sim 0$. **Figure 24d** shows case (3) of the combination of the two thermal-induced effects. Its velocity distribution can be considered as the superposition of the previous two cases. In case (1) and (2), the corresponding velocities are in the same order of magnitude; therefore, the maximum velocity in case (3) appears at a position between the two previous cases ($u_{max}\sim 9\ \mu$m/s at $z\sim 150\ \mu$m).

Overall, when only considering the thermocapillary effect, the strongest flows occur near the upper boundary, and the corresponding backflow in the lower portion of the liquid layer is weak. When only considers the gravitational effect, prominent convection rolls are formed in the cell; the last case shows the combination of the two previous convection, the maximum velocity shifts its position and strength accordingly with respect to the Marangoni effect. This distribution difference in these three cases shows the possibility of distinguishing the two thermos-induced effects in reality.

2.6 Flow velocity distribution analysis on different surfaces

Based on the above simulation analysis, I did more experiments on surfaces with different wettability and structures to recognize their corresponding flow mechanisms: superhydrophobic soot surfaces ($b\sim 0.22\ \mu$m), superhydrophilic soot surfaces ($b = 0$), and superhydrophobic pillar surfaces ($b\sim 3.2\ \mu$m). Note that we applied the effective slip length b on superhydrophobic surfaces with the values for the transverse cases. Among these surfaces, superhydrophobic and superhydrophilic soot surfaces have similar surface morphology, except for their wettability. Superhydrophilic surfaces are tested to experimentally examine the gravitational effect in the absence of the Marangoni stress. To test the role of the surface structure (i.e., the effective slip length b) on the thermocapillary flows, superhydrophobic pillar surfaces were also tested. As the pillar surface proposes a slip length of one more order of magnitude than on the soot surface, a more evident Marangoni stress is expected.

It also should be noted, as investigated before, the most evident difference between different flow mechanisms is illustrated on the velocity profiles near the upper surfaces (where the main flows are directed to r-direction). Therefore, the regions having a horizontal distance of r from the heated center are recorded (**Figure 22b**).

2.6.1 Superhydrophobic soot surface

Figure 25 shows the experimental velocity distributions in the upper portion of the liquid layer with defined horizontal distances from the center of the hot spot ($r = 500, 1500, 2500 \, \mu$m, $z < 500 \, \mu$m) as well as near the upper water interface ($z \leq 50 \, \mu$m), respectively.
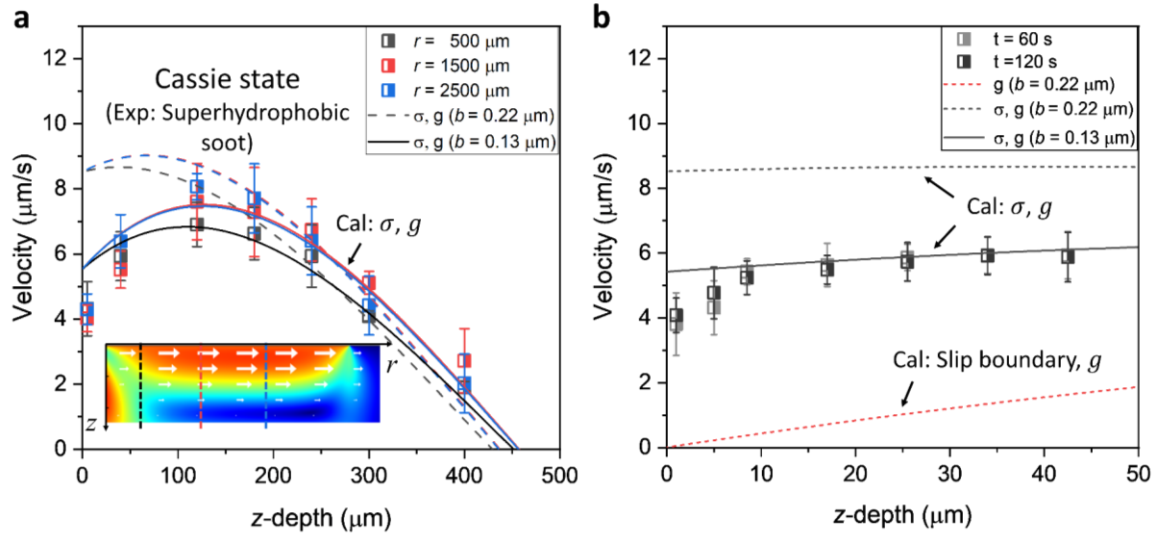
Figure 25. Velocity distribution in the upper portion of the liquid layer, being in contact with superhydrophobic soot surfaces in the Cassie-Baxter state. Points: Experiments; Lines: Simulations. (a) Velocity profiles in the upper fluid cell ($z < 500 \, \mu$m). Lines: case 3 (Marangoni stress σ, gravitational effect g). Inset: simulated velocity magnitude. (b) Velocity profiles near the upper surface for $r = 500 \, \mu$m ($z < 50 \, \mu$m). Lines: cases 2 (slip, g, red) and case 3 (σ, g, black).

The experimentally flow velocity near the superhydrophobic soot surface shows an average value $u \sim 4 \, \mu$m/s at $z \sim 0$, and shows an increase with the depth z. The maximum flow $u_{\text{max}} \sim 8$ μm/s appears at $z \sim 150 \, \mu$m (**Figure 25a**). The experimental velocity profiles do not match the ones in case (1) when only considers the Marangoni stress since the maximum experimental velocity does not appear at the upper boundary. Instead, their shapes are similar to case (3) by considering both the thermocapillary effect and the gravitational effect. The value of the effective slip length b that input in the simulation can affect the resulting velocity profiles, especially the maximum velocity. The larger the slip length, the maximum velocity occurs more closer to the surface. By applying the estimated effective slip length $b \sim 0.22 \, \mu$m in case (3), the corresponding velocity profiles show a similar trend with the experimental ones. However, it is not quite consistent with the experiments. The maximum simulated velocities

appear to be closer to the upper surface, and the boundary velocities are approximately twice compared with the experimental ones (**Figure 25a**).

It has to be considered that, first of all, as mentioned before, the effective sip length and the boundary condition utilized in the simulation may lead to overestimation of the flows. Secondly, there may be contaminations on superhydrophobic surfaces, such as surfactant residues. Even for surfactants with an ultra-low concentration as lower than 10^9 mol/m^3 on the superhydrophobic surface (after a standard microfluidic cleaning process), the reversed Marangoni effect (Ma_s) due to surfactant concentration gradients can largely hinder directional flows.[105, 109-111] These factors may reduce the flow velocity at the interface. Therefore, it is reasonable that the simulated velocity profiles for a slip length of 0.22 μm do not fit the experimental velocity profiles. Instead, an effective slip length of 0.13 μm is estimated, which is more consistent with the experimental velocity profiles (with a theoretical flow velocity of $u_M \sim \frac{\partial \sigma}{\partial T} \frac{\partial T}{\partial r} \cdot \frac{b}{\mu} \sim 5.3$ μm/s). This agreement indicates that the gravitational effect cannot be simply ignored in such a millimeter-scale system. Recently, the gravitational effect on such a small scale has also been reported in the work of Li *et al.*[112] for droplets.

Furthermore, the differences in velocity profiles between the experiment and the simulation in case (2) demonstrate the Marangoni flows present at the superhydrophobic surface (**Figure 25b**). The simulated profile of case (2) is obtained by only considering the gravity and a slip boundary without Marangoni stresses (slip, g, b =0.22 μm). In this case, nearly no flow occurs at the upper boundary ($u \sim 0$, $z = 0$). Hence, there must be thermocapillary flow generated at the superhydrophobic surface.

2.6.2 Superhydrophilic soot surfaces

Fluid convections are also observed in the control experiment on superhydrophilic surfaces (**Figure 26**). In this case, there is no Marangoni stress on the hydrophilic surface due to the absence of the liquid-air interfaces. The upper boundary is considered as a non-slip boundary ($b = 0$). The only thermal effect that has to be considered is the gravitational effect.
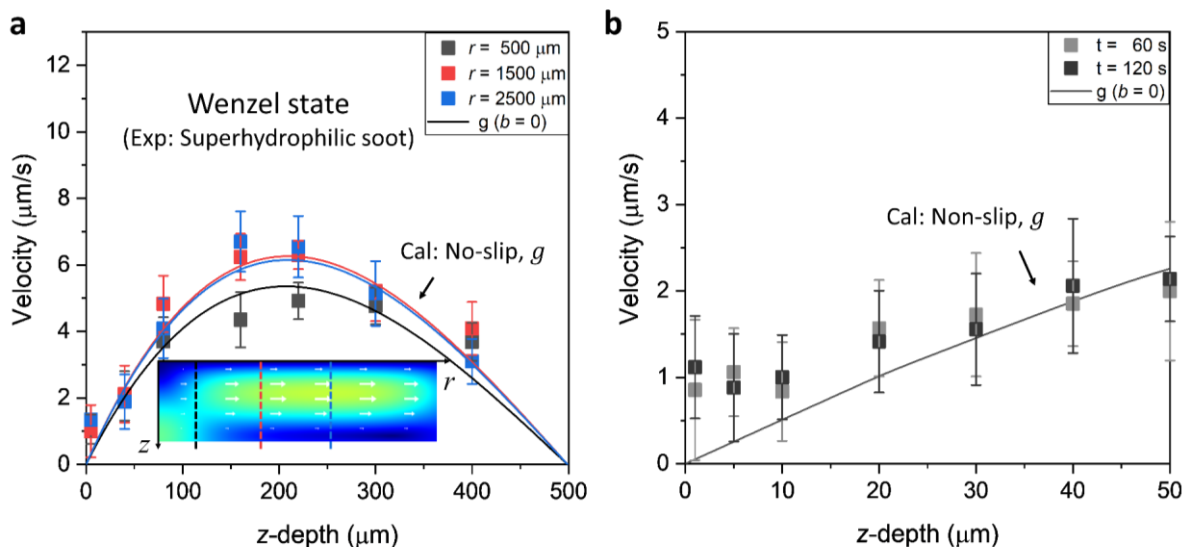
Figure 26. Flow velocity distributions in the liquid layer being in contact with a superhydrophilic soot surface from above (Wenzel state). Points: Experiments; Lines: Simulation for case (2) by considering the gravitational effect (No-slip, g). (a) In the upper portion of the liquid cell ($z < 500~\mu$m). Inset: simulated velocity magnitude; (b) Velocity profiles near the upper surface for $r = 500~\mu$m ($z < 50~\mu$m).

The velocity distributions at regions with different horizontal distances r from the laser-irradiated spot in the upper part of the liquid layer ($500 < r < 2500~\mu$m, $z < 500~\mu$m) are shown in **Figure 26a**. The experimental velocity profiles were in good agreement with the simulation results. The maximum flow velocity $u_{\max} \sim 7~\mu$m/s appears at $z \sim 250~\mu$m, which is shifted away from the upper boundary compared to the previous case on superhydrophobic surfaces.

Figure 26b shows the close-up of the flow profile close to the upper boundary ($z < 50~\mu$m) at $r = 500~\mu$m. Near the upper interface ($z \sim 0$), no evident directional flows have been observed. However, an average velocity value $u \sim 1~\mu$m/s was still obtained here. This value is originated from the diffusion of the dispersed particles due to Brownian motion (which is expected to be about 1 μm/s according to the Stokes-Einstein relation[113-114]). Overall, the good agreement between the experiments and calculations emphasizes the critical role of the gravitational effect in triggering flows. The corresponding flows, not only orientations but also velocity values, are similar to those originated from the thermocapillary effect. This result shows that this "upside-down" design allows us to utilize the gravitational effect to enhance thermocapillary flows in superhydrophobic-based systems.

2.6.3 Superhydrophobic pillar surfaces

As discussed before, the thermocapillary flow on a superhydrophobic surface is affected by its slip length (b).[33] For a better understanding of this factor, superhydrophobic pillar surfaces with a more evident slip length ($b\sim3.2\ \mu$m, about 10 times on soot surfaces) were tested. The corresponding flow velocity profiles near the pillar surface are shown in **Figure 27**.
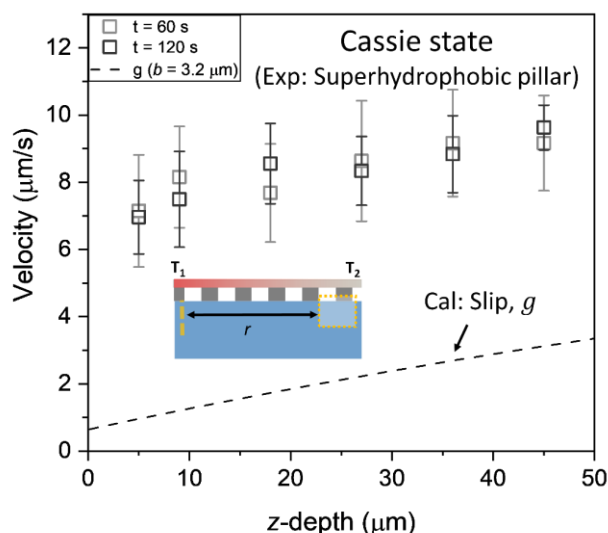
Figure 27. Velocity profiles in the liquid cell near a superhydrophobic pillar surface ($b\sim3.2$ μm, Cassie state). Dashed line: Calculation of case 2 (slip, g, $b\sim3.2\ \mu$m). Insets: Schematic of the observation region near the pillar surface ($r = 500\ \mu$m, $z \leq 50\ \mu$m).

As shown in **Figure 27a**, a more evident Marangoni flow is indeed observed near the pillar surface. Near the upper surface, the experimental velocity $u_{\text{pillar}}\sim 7\ \mu$m/s ($z\sim 0$). It is much larger than the simulated velocity of the case (2) when only considering the gravitational effect and a slip boundary (slip, g, $b\sim 3.2\ \mu$m). However, the increase of the velocity on superhydrophobic pillar surfaces is not that evident as predicted in case (3) when considering the Marangoni stresses. A slip length of $b\sim3.2\ \mu$m can lead to a theoretical thermocapillary flow velocity of $U_M\sim110\ \mu$m/s, almost two orders of magnitude of the experimental one. This massive overprediction, similar to the case on superhydrophobic soot surfaces, was caused by the defined boundary conditions and the possible surfactant contaminations on superhydrophobic surfaces. In addition, due to the large features of the pillar structures, the liquid interfaces at the pillar surfaces may be deformed, thereby primarily reducing the

directional thermocapillary flows (which has been reported to be dropped below 0.4% near the boundary).[115]

Even though the thermocapillary flow velocity was not that evident as predicted, a higher experimental velocity was obtained on superhydrophobic pillar surfaces (about two times of the velocity on soot surfaces shown in **Figure 25b**, $u_{\text{pillar}} \sim 2u_{\text{soot}}$). This result shows that a more pronounced thermocapillary flow can be expected on a superhydrophobic surface with a large slip length. In addition, the corresponding Marangoni number Ma that presenting the thermocapillary convections on soot and pillar surfaces, can be written as $Ma = U_M \frac{h}{\alpha} = -\frac{\partial \sigma}{\partial T} \frac{\partial T}{\partial r} \frac{b}{\mu} \frac{H}{\alpha}$ (equation (2-10) and (2-11)). With the small temperature gradients that generated in this project, *i.e.,* 0.2 to 0.3°C /mm, Ma is calculated to be in the range of 0.1 to 0.37. This value further theoretically verifies the presence of the thermocapillary convections in the liquid cell. In addition, this expression shows that the design of the set-up as well as liquids with different thermal diffusion coefficient α can also affect the thermocapillary flows. To better utilize the thermocapillary effect to trigger flows, more investigations on the relationship between the thermocapillary flow and the slip length b, the role of contaminations on the superhydrophobic surface, and the design of the experimental devices are required.

2.7 Summary

Here, an optical approach of manipulating liquid flows in a confined millimeter-sized water layer, which is in contact with a superhydrophobic surface, has been reported. By illuminating the superhydrophobic surface with focused light, due to the photothermal effect of the surface, the liquid is heated up and generates a small temperature gradient, i.e., 0.2 °C/mm near its upper interface. Liquid flows with a velocity of a few μm/s are created in the liquid layer. The corresponding experimental velocity distributions, which are in agreement with numerical simulations, show that the fluid motions can indeed be created due to the Marangoni effect on the superhydrophobic surface. The thermally-induced gravitational effect, which is usually neglected on small scales, was also found to drive flows. In addition, the flows driven by these two effects are in the same direction. To distinguish them, comparison experiments on superhydrophilic surfaces and superhydrophobic surfaces with different slip lengths were done.

This fundamental study helps us to better understand the fluid dynamics on superhydrophobic surfaces. From a practical point of view, this optical approach allows us to control liquid flows temporally and spatially, especially when combined with superhydrophobic surfaces. The

experimental setup design on the microscopic scales, i.e., the effective slip length of the superhydrophobic surface, plays a vital role in actuating flows. With the presented optical triggering flows by the gravitational effect, new propulsion and pumping methods for fluids are also expected.

3 Controlled droplet evaporation on oil-coated surfaces

The following work is based on the article that has been published as Gao et al. (2019):

Gao, A., Liu, J., Ye, L., Schönecker, C., Kappl, M., Butt, H. J., Steffen, W. Control of droplet evaporation on oil-coated surfaces for the synthesis of asymmetric supraparticles. *Langmuir*, 2019, *35*, 14042-14048. (Reprinted with permission from Ref.[116] Further permissions related to the material excerpted should be directed to the ACS.
https://pubs.acs.org/doi/full/10.1021/acs.langmuir.9b02464)

The "coffee ring" effect is a ubiquitous phenomenon in droplets of solutions drying on surfaces. However, controlling the distribution of solutes in drying liquids to produce homogeneous depositions is highly required in real applications. For this one needs to suppress the "coffee ring" effect. A practical approach is to alternate the internal flows in the droplet via controlling the evaporation flux along the droplet surface. Here, I show that control droplets evaporation to control flows as well as final particle depositions can be achieved through evaporating droplets on oil-coated surfaces.

3.1 Fundamentals

3.1.1 Droplet configurations

3.1.1.1 Sessile droplets on solid surfaces: Young's equation

When a drop of liquid such as water is deposited on a flat solid surface, it forms a spherical cap on the substrate.
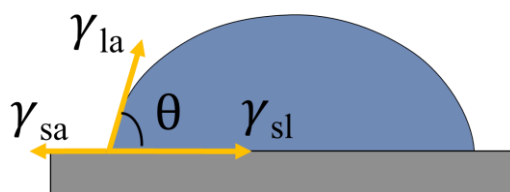
Figure 28. Schematic of a droplet resting on a solid surface. The droplet geometry is determined by the three interfacial tensions at the three-phase contact line.

The wetting configuration of the droplet depends on the balance of the interfacial tensions between the liquid-air (γ_{la}), solid-air (γ_{sa}) and liquid-solid (γ_{ls}) interface (**Figure 28**), which meet the relation of:[117]

$$\gamma_{la} \cos \theta = \gamma_{sa} - \gamma_{ls} \qquad\qquad (3\text{-}1)$$

Here, θ is the contact angle near the droplet three-phase contact line. This equation is also known as Young's equation. The contact angle is an important criterion to describe the surface wettability. For instance, if a droplet has an apparent contact angle $\theta > 90°$ near its edge, the substrate upon which it sits is defined as being hydrophobic; if $\theta < 90°$, the surface is hydrophilic. However, this equation only describes the contact angle in a static state; it cannot fully characterize a substrate, *e.g.*, surface roughness and chemical heterogeneity. For instance, on a superhydrophobic surface with hierarchical micro/nano-structures, water droplets show two possible wetting states: the Wenzel state (water penetrates the hierarchical structures)[118] and the Cassie-Baxter state (air trapped in the valleys of the structures)[35]. However, the static contact angle of droplets on these two surfaces both show $\theta > 150°$.

To fully characterize the substrate, contact angle hysteresis, which describes the droplet distortion in motion, is introduced to provide relevant information. For instance, a droplet sliding on a tilted substrate, its front advances (on the downhill side) while its rear recedes (on the uphill side). The difference between the critical advancing contact angle θ_{adv} and receding contact angle θ_{rec} is defined as the contact angle hysteresis θ_{CAH}, $\theta_{CAH} = \theta_{adv} - \theta_{rec}$. The lower hysteresis is, the easier the droplet moves on the substrate. The contact angle hysteresis is usually used to describe the droplet dynamics, *e.g.,* during its evaporation or sliding process.

3.1.1.2   Sessile droplets on low surface tension liquid-wetted surfaces

Compared with a droplet sitting on a solid surface, a droplet sitting on a solid surface is wet with another low-surface-tension liquid, *e.g.,* a water droplet on an oil-coated surface, the droplet configuration becomes more complicated than on a solid substrate. It mainly depends on the interfacial tensions among these immiscible phases on such a four-phase system (the oil, droplet, air, and solid substrate). Therefore, the spreading coefficient S and Young's equation, which are expressed in terms of interfacial tensions, are used to evaluate the droplet configurations. Four possible configurations are expected (**Figure 29**).
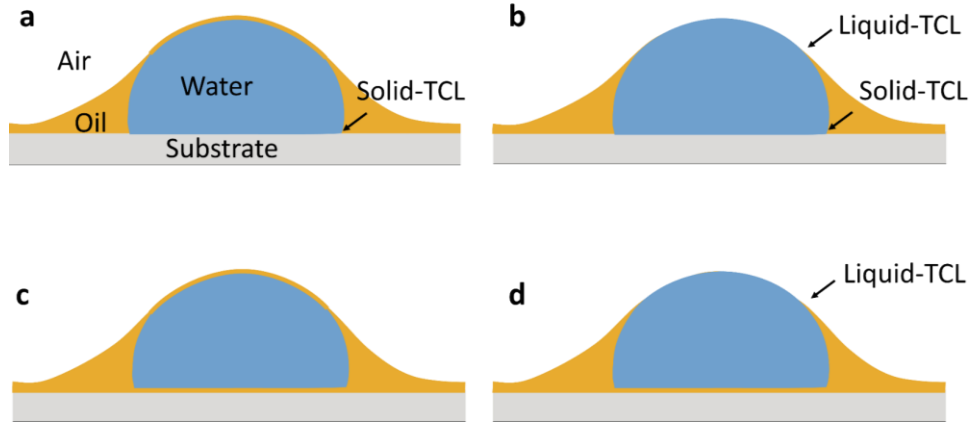
Figure 29. Schematic of possible wetting configurations of a sessile droplet on a lubricant oil-coated surface. The droplet rests on the substrate and pulls up the lubricant oil phase. The oil phase may "cloak" the droplet (a)(c) or partially wet the droplet, forming an oil "wetting ridge" around the droplet (b)(d). At the droplet base, the droplet may be directly in contact with the substrate (a)(b) or rest on a thin lubricant oil film (c)(d). Two possible three-phase contact lines (TCL) are shown: a liquid-TCL where droplet, lubricant oil, and air meet at the droplet surface and a solid-TCL where droplet, lubricant oil, and solid substrate meet at the droplet edge.

Smith *et al.* have theoretically analyzed these four configurations from two aspects:[67, 119]

(1) At the droplet surface: The low-surface-tension oil climbs up the droplet, may completely "cloak" the droplet, or form an annular "wetting ridge" around the droplet. Which of these occurs is determined by the spreading coefficient $S_{\text{ol(a)}}$,[119]

$$S_{\text{ol(a)}} = \gamma_{\text{la}} - \gamma_{\text{lo}} - \gamma_{\text{oa}} \tag{3-2}$$

where γ_{oa} and γ_{lo} are the interfacial tensions at the oil-air and liquid-oil interface, respectively. When $S_{\text{ol(a)}}$ is positive, the oil phase may completely "cloak" the sessile droplet (**Figure 29a,c**), e.g., a water droplet on a surface coated with a fluorinated oil-FC70 ($S_{\text{ol(a)}}$ =1.3 mN/m, where γ_{oa} =17.9 mN/m and $\gamma_{\text{lo}} \approx$ 52.8 mN/m).[67]

The thickness of the cloaking oil at the droplet apex can be theoretically estimated by equating the capillary force P of the oil film due to its curvature (related to the droplet radius, $P = 2\gamma/R$) as well as the disjoining pressure Π_{D} (which originated from the van der Waals forces between the two interfaces of the cloaking film), $\Pi_{\text{D}} = \left(\frac{A_{\text{H}}}{6\pi B^3}\right)^{1/3}$. Here, A_{H} is the Hamaker constant,

which quantifies the strength of the interaction between molecules.[120] Therefore, the oil film thickness B is expressed as,[67]

$$B \sim \left(\frac{A_{\mathrm{H}}R}{12\pi\gamma}\right)^{1/3} \tag{3-3}$$

In contrast to the previous case, when $S_{\mathrm{ol(a)}}$ is a negative value, the oil phase cannot completely spread over the droplet. It only forms a "wetting ridge" around the sessile droplet and exhibits a three-phase contact line at the droplet surface (liquid-TCL, where lubricant oil, droplet, and air meet) (**Figure 29b,d**). The height of the wetting ridge $h(r)$, can be analyzed by $P = 2gC(r) - \rho gh(r)$.[67, 121-123] Here, $C(r)$ is the mean curvature at the oil-air interface, r is the distance from the droplet center, and P is the pressure in the oil wetting ridge.

(2) Underneath the droplet: the droplet may rest on top of a thin oil film or repel the oil film and directly deposit on the solid substrate. Whether a thin oil film arises between the droplet and substrate depends on the interfacial tensions between the three phases, which is expressed as,[119]

$$S_{\mathrm{ol(s)}} = \gamma_{\mathrm{ls}} - \gamma_{\mathrm{lo}} - \gamma_{\mathrm{os}} = -\gamma_{\mathrm{lo}}(\cos\theta_{\mathrm{oil}} + 1) \tag{3-4}$$

where $S_{\mathrm{ol(s)}}$ is the corresponding spreading coefficient and γ_{os} is the oil-solid interfacial tension. θ_{oil} is the water contact angle at the water-solid-oil three-phase contact line (measured from the droplet depositions on the substrate in the silicone oil bath).When $\theta_{\mathrm{oil}} < 180°$, $S_{\mathrm{ol(s)}} < 0$, implies that the droplet can directly deposit on the solid substrate (**Figure 29a,b**), e.g., a dodecanol droplet rests on a silicone oil-coated polymethylpentene (PMP) surface ($\theta_{\mathrm{o}} \sim 23°$, $S_{\mathrm{ol(s)}}$ =-64 mN/m).[124] By contrast, **Figure 29c,d** show the case of the droplet rests on the oil layer ($S_{\mathrm{ol(s)}} > 0$). E.g., a water droplet rests on a thin silicone oil film when it is deposited on a silicone oil-coated PMP substrate. In this case, the thin oil film sandwiched between the droplet and the substrate, can also be calculated by the balance of the Laplace pressure P and the disjoining pressure Π_{D} due to van der Waals interaction in the oil film. Thus, the theoretical oil film thickness is given by $h \sim (RA/\gamma)^{1/3}$, where A is a coefficient estimated by the Hamaker constant.[125-126] Besides the value of S, Denial *et al.* also pointed out that whether there is a continuous oil film beneath the droplet depends on the coefficient A.[124] E.g., for a droplet of 60 wt% sucrose solution deposited on a silicone oil-coated PMP surface, even through $S_{\mathrm{ol(s)}}$ >0, the oil dewets into pockets instead of forming a continuous film under the droplet (A <0).

Therefore, due to the interplay of the interfacial tensions, the sessile droplet may exhibit zero, one and two three-phase contact lines (TCL), respectively. **Figure 29c** shows the particular case when the lubricant oil entirely covers the droplet (zero TCL), *e.g.,* a water droplet on a silica oil-coated hydrophobic surface. **Figure 29b** shows a sessile droplet with two three-phase contact lines: a solid-TCL at its base and a liquid-TCL at its upper surface, *e.g.*, a water droplet on an ionic liquid-coated surface.

3.1.2 Evaporation mode and rate of sessile droplets

3.1.2.1 Three evaporation modes

The evaporation of a droplet from solid surface proceeds in three modes[127] (**Figure 30**). (1) Constant contact angle mode (CCA). [64, 128-129,130-131] In this mode, the contact line of the droplet continuously recedes on the substrate. It usually occurs when droplets have contact angles larger than 90° and show extremely low contact angle hysteresis (less than 10°), *e.g.,* droplets evaporating on smooth hydrophobic surfaces. (2) Constant contact radius mode (CCR).[44, 132-135] In this mode, the droplet is pinned on the substrate while its contact angle continuously decreases. Typically, this mode occurs when the initial contact angle of droplets is less than 40° on hydrophilic substrates. (3) Mixed mode, or stick-slip mode.[136-139] The contact angle and contact radius of the droplet decrease gradually with time (transitions between the CCA and CCR modes). In practice, a sessile droplet may not evaporate in only one extreme modes, but in the mixed mode.
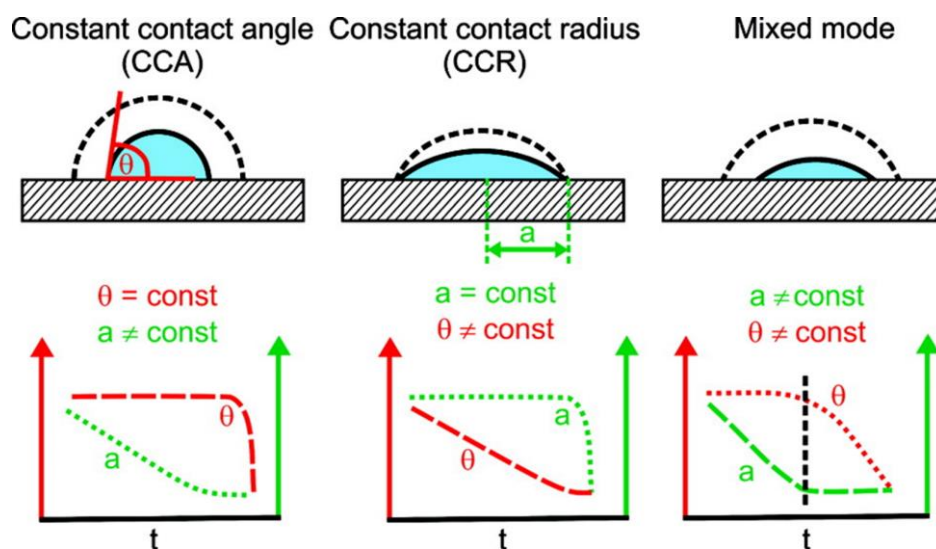
Figure 30. Three basic evaporation modes of sessile droplets. The plots of the corresponding contact angle and contact radius as a function of time are also plotted. Reprinted with permission from Ref.[140] Copyright © 2009, American Chemical Society.

3.1.2.2 Evaporate rate of sessile droplets

For a liquid droplet with a size smaller than the capillary length $\lambda_c = \left(\frac{\sigma}{\rho g}\right)^{1/2} \sim 2.7$ mm,[141] the gravity factor becomes negligible. The droplet forms a spherical cap shape on a substrate. From the side view, the cap geometry can be expressed with the time-dependent volume V, height h, base radius r, spherical cap radius R and contact angle θ, as shown in **Figure 31**.
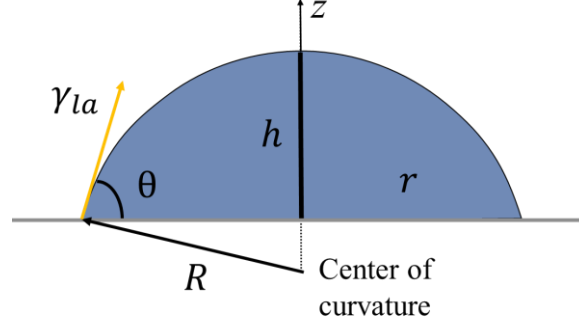
Figure 31. Profile of a sessile droplet on a substrate.

These parameters are shown as

$$r = R \sin \theta, R = \left(\frac{3V}{\pi\beta}\right)^{\frac{1}{3}} \tag{3-5}$$

$$h = R(1 - \cos \theta) \tag{3-6}$$

$$V = \frac{1}{3}\pi r^3 \beta = \pi R^3 \frac{\beta}{3 \sin^3 \theta} \tag{3-7}$$

where V is the droplet volume, $\beta = (1 - \cos \theta)^2 (2 + \cos \theta)$. During droplet evaporation, all these parameters are changing accordingly. The liquid loss rate through a liquid-air interface, which described by the droplet volume changes dV, is expressed as[142-143]

$$\frac{dV}{dt} = -\frac{1}{\rho}\int J \cdot dS = \frac{4\pi R D}{\rho}(c_s - c_\infty)f(\theta) \tag{3-8}$$

Here, ρ is the density of the liquid, S is the surface area of the cap where evaporation occurs, $S = 2\pi R^2(1 - \cos \theta)$. J is the evaporation flux along the droplet surface, $J = -D\mathbf{n} \cdot \nabla C$.[144-146] D is the diffusion coefficient of the vapor, $\mathbf{n}$ is the unit normal to the surface and ∇C is the vapor concentration gradient from the droplet surface (c_s) to the atmosphere (c_∞) through the liquid-air interface of the droplet. Normally, the evaporation flux J is not uniformly distributed

at the droplet surface and is related to the geometry of the droplet.[143, 147] For instance, Deegan *et al.* pointed out that the droplet evaporation flux (J) along its free surface is a diverging normal derivative,[44, 146, 148-149] $J = (R - r)^{B(\theta)}$, where $B(\theta) = \frac{2\theta - \pi}{2\pi - 2\theta}$. When $0 < \theta < 90°$, the evaporation flux at the contact line is higher; when $\theta > 90°$, the flux is minimized at the contact line. When $\theta = 90°$, the flux along the droplet surface is uniform distributed and can be simplified by $J = D(c_s - c_\infty)/R$.[143]

The function $f(\theta)$ expresses the dependence of the evaporation flux on the contact angle.[130, 142-143] An exact solution for $f(\theta)$ was derived by Picknett and Bexon,[142] which is given by

$$f(\theta) = \frac{1}{2}(0.0008157 + 0.6333\theta + 0.116\theta^2 - 0.08878\theta^3 + 0.01033\theta^4) \qquad (3\text{-}9)$$

where $10° < \theta < 180°$. In more recent works, Stauber *et al.*[147] modified the term $f(\theta) = \frac{g(\theta)}{(1+\cos\theta)^2}$, where $g(\theta)$ is given by $g(\theta) = (1 + \cos\theta)^2 \left\{ \tan\frac{\theta}{2} + 8 \int_0^\infty \frac{\cosh^2 \theta\tau}{\sinh 2\pi\tau} \tanh[\tau(\pi - \theta)] \, d\tau \right\}$, to evaluate the case for droplets evaporating on strongly hydrophobic surfaces.

Equation (3-7) has shown that V is related to contact angle θ and base radius r, which may vary independently as a function of time. Therefore, this single equation cannot fully describe the droplet evaporation process. However, the two constant modes, i.e., CCA and CCR, have shown the two extreme cases that may occur.

Case (1): CCA mode, $\theta_t = \theta_0 = $ constant. For instance, when droplets evaporate on smooth hydrophobic surfaces, the corresponding evaporation equation (3-8) is simplified as

$$\frac{dV}{dt} = -\lambda \left(\frac{3V}{\pi\beta}\right)^{\frac{1}{3}} f(\theta) \qquad (3\text{-}10)$$

where $\lambda = \frac{4\pi D(c_s - c_\infty)}{\rho}$. This equation can further be integrated between the initial volume of the droplet V_0 ($t \to 0$) and V_t ($t \to t$),

$$V(t)^{2/3} \approx V_i^{2/3} - \frac{4\lambda}{3}\left[\frac{3}{\pi\beta(\theta_0)}\right]^{1/3} f(\theta)t \qquad (3\text{-}11)$$

This equation illustrates that volume V to the power of 2/3, shows a linear relationship with time.

Case (2): CCR mode, $r_t = r_0 = $ constant and the contact angle of droplet $\theta(t)$ variable. The equation (3-8) has to be numerically integrated. The evaporation dynamics for these two cases can be concluded by the equation (3-8). For the case (3) of droplet evaporates in the mixed-mode, the above equation also performs by considering the evaporating process as alternating behaviors of the case (1) and (2).

3.1.3 Droplet evaporation on lubricant oil-coated surfaces

For a droplet deposited on a slippery lubricant liquid-coated surface, the low-surface-tension oil spontaneously forms a "wetting ridge" around the droplet rim. The optical image and the corresponding schematic of the sessile droplet on an oil-coated surface are shown in **Figure 32**. The nonvolatile oil "ridge" hinders the droplet from evaporating from its edge.[70, 150] It is natural to assume the droplet only evaporates from its apex. Guan *et al.*[70] have mentioned that the reduction of the evaporation can be expressed by a factor of h_s/h_0 compared to a droplet evaporate on a solid substrate. Here h_s is the height of the "wetting ridge" and h_0 is the height of the sessile droplet. In addition, due to the low contact angle hysteresis on lubricant-infused slippery surfaces, droplets on such a surface may evaporate in the CCA mode while its contact line continuously recedes.[64, 128]
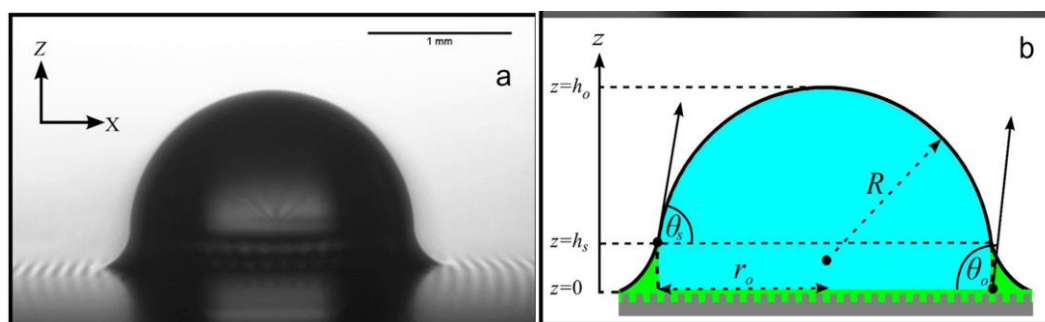
Figure 32. A sessile water droplet on a slippery lubricant oil-coated surface. (a) The optical image of the sessile droplet; (b) Schematic of the cross-section of the sessile droplet.[70] Reprinted with permission from Ref.[70] Copyright © 2015, American Chemical Society.

Assuming the apparent contact angle at the height h_s of the "wetting ridge" above the substrate is θ_s, the equation (3-10) can be rewritten as[70]

$$\frac{\mathrm{d}V}{\mathrm{d}t} = -\lambda \left(\frac{3V}{\pi\beta}\right)^{\frac{1}{3}} f(\theta_{\mathrm{s}}) \tag{3-12}$$

which is also expressed as

$$V(t)^{2/3} \approx V_i^{2/3} - \frac{4\lambda}{3}\left[\frac{3}{\pi\beta(\theta_0)}\right]^{1/3} f(\theta_{\mathrm{s}})t \tag{3-13}$$

Here, V_i is the initial volume of the droplet.

In this work, the oil "wetting ridge" on the evaporation dynamics of sessile droplets is studied. Compared with the lubricant-infused slippery surfaces, where the low contact angle hysteresis also dominates the evaporation dynamics, we decouple it from the surface wettability by using smooth surfaces. Smooth surfaces with different wettability are used to examine the general evaporation modes as well as deposition features.

3.2 Experimental

3.2.1 Materials

Silicone oils with viscosities from 10 to 10^5 cSt (with molecular weight MW from 1.250×10^3 to 1.39×10^5 g/mol) were purchased from Sigma-Aldrich. Vinyl-terminated polydimethylsiloxane (vinyl-terminated PDMS) with a viscosity in the range of 10 to 10^5 cSt (MW. 1.20×10^3 to 1.40×10^5 g/mol), a crosslinking agent (HMS-301), and platinum catalyst (SIP6831.2) were purchased from Gelest Inc. PS beads with fluorescently labeled and non-fluorescent labeled were used. Among them, the fluorescent PS particles (diameter 2.5 μm, excitable at 488 nm and emitting in the range of 515 ~ 600 nm) were bought from life technologies, USA; non-labeled PS particles (diameter of 3 μm) were synthesized in our lab by the dispersion polymerization method. Glass slides with dimensions: 25×75 mm and 150 μm thickness were bought from ThermoFisher. In all experiments, the temperature and the relative humidity were $T_a = 23 \pm 2$ °C and RH = 47 ± 5%, respectively.

3.2.2 Preparation of liquid-coated surfaces

To study the deposition feature of the droplet is whether determined by the flow patterns in the evaporating droplet or by the depinning of its contact line on the oil-coated surfaces, I prepared substrates with different wettabilities (hydrophilic and hydrophobic surfaces). The glass slides were first ultrasonically cleaned in ethanol, toluene, and isopropanol for 15 min, respectively,

and then treated with oxygen plasma for 10 min (UV light intensity: 100 mW/m^2, oxygen flow rate of 6 sccm). These slides were treated differently in two groups.

Hydrophobic surfaces: The plasma-treated glass slides were directly coated with silicone oil. The oil spontaneously spreads and forms a thin film on the glass surface due to its low surface tension ($\gamma \sim 20$ mN/m). Since the slides were exposed to the silicone oil phase after plasma treatment (less than 40 s), the hydrophobic oil phase shields due to van der Waals interaction and even form chemical siloxane (Si-O-Si) bonds with the activated glass surfaces, thus leading to hydrophobic substrates.[151-152]

Hydrophilic surfaces: The treated slides were first immersed in a Milli-Q water bath, allowing water to form hydrogen bonding with the hydrophilic sites on the active glass slides and decreasing the organic contamination from the atmosphere. After 3 h, these slides were dried with N$_2$ flow and coated with silicone oil. This approach allows the glass surfaces underneath to remain hydrophilic since the van der Waals interaction between silicone oil and the glass slides has mainly been decreased. In rare cases for thin oil layers (e.g., $< 10 \ \mu$m), oil dewetting occurs.

The slides with silicone oil coating in both groups were processed with a spin-coating procedure to obtain silicone oil films with different thicknesses. These samples were then placed on a horizontal plane for a few hours to let the liquid silicone oil film more uniformly spread on the slides, as the oil film at the edge may become thicker than in the center after the spin-coating process.

A white-light confocal microscope (µsurf®c series, NanoFocus AG, Germany) was applied to measure the oil film thickness. To obtain the oil film thickness after spin-coating, one can make a scratch onto the film to measure the height difference as the film thickness. Since it is impossible to make a scratch on the oil film being in the liquid phase, chemically similar crosslinked polymer films were prepared. Therefore, the cross-linkable vinyl-terminated PDMS (similar viscosity as the liquid silicone oil) was used instead.[153] The mixture of the vinyl-terminated PDMS (viscosity in the range of 10 to 10^5 cSt), a crosslinking agent (4 wt%), and a platinum catalyst (0.005 wt%) was spin-coated onto glass slides with defined speeds (from 400 rpm/s to 8000 rpm/s) for 30 s. These samples were then placed on a horizontal plate for a few hours, followed by placing them in an oven (60 °C) overnight to cure PDMS films. By making scratches with a blade on the cured PDMS films, the film thicknesses were measured under the Nanofocus microscope with a 20x objective (with a horizontal resolution

of 1.6 μm and vertical of 6 nm). With this approach, the thickness of the liquid oil film (corresponding to PDMS with similar viscosity) under the same spin-coating speed was assumed. The thickness of the crosslinked PDMS film with different viscosities (10 to 10^3 cSt) as a function of spin-coating speed is shown in **Figure 33**. Notably, for vinyl-terminated PDMS with higher viscosities (10^4, 10^5 cSt), dilution in hexane with a volume ratio of 1:10 was prepared to obtain smooth films on slides by the spin-coating procedure.
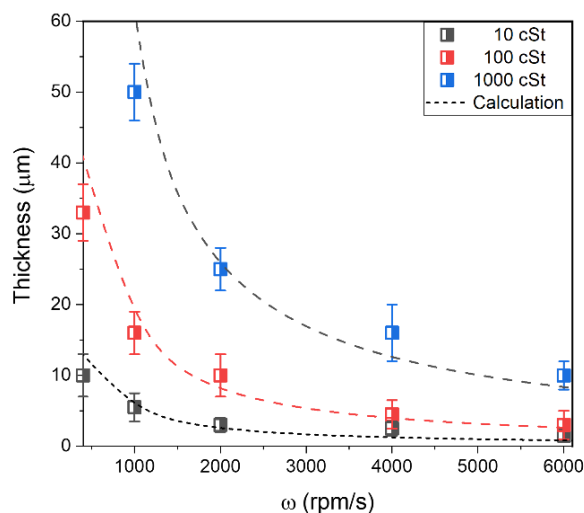
Figure 33. The thickness of the vinyl-terminated PDMS film in terms of spin-coating speed. PDMS with different kinematic viscosities (grey: 10 cSt, red: 100 cSt; blue: 1000 cSt) were measured. The dashed lines show the evaluating curve of the final thickness h with spin speed ω, $h \sim \left(\frac{v}{\omega^2}\right)^{1/2}$.[154-155]

3.2.3 Contact angle measurements

The wettability of each glass slide was measured with a Dataphysics OCA35 goniometer, with the sessile drop configuration (Data Physics Instruments GmbH, Germany). To distinguish the wettability of the substrates without the oil coating, the oil was first washed away from the pre-coated substrates by ultrasonically cleaning the substrate in hexane for 5 min before measuring. A dynamic sessile drop approach was applied. A 4 μL water droplet was first deposited on the measured surface. Then a needle was inserted into the droplet. An additional 10 μL water was injected into the droplet at a rate of 0.2 μL/s, then kept for 10 s before withdrawing the injected water from the droplet. By this process, a series of images of the advancing and receding contact angles (θ_{adv}, θ_{rec}) on the substrates were obtained. On hydrophobic surfaces, $\theta_{adv} \approx 102 \pm 3°$, $\theta_{rec} \approx 92 \pm 5°$; on hydrophilic surfaces, $\theta_{adv} \approx 75 \pm 3°$, $\theta_{rec} \approx 40 \pm 6°$.

3.2.4 Surface tension measurement

The surface tension of the water solution dispersed with micro-PS particles (with concentrations from 10^8 to 10^{12} /mL) was measured with a Wilhelmy plate tensiometer (DCAT11EC, DataPhysics, Germany) (**Figure 34**). A thin, rectangular plate made of platinum-iridium alloy (PT11, with a length $l = 19.9$ mm and thickness $b = 0.2$ mm) was used and attached to the weighing system. The plate is chemically stable and roughly enough for completely wetting by different liquids (the corresponding contact angle of a liquid on the plate $\theta = 0°$).[156] When the liquid bath is raised to a stage where the plate comes into contact with the liquid surface, the liquid simultaneously wet the plate and formed a liquid meniscus at the plate surface. The force exerted on the plate surface (F) due to surface tension force is measured using the tensiometer. The corresponding surface tension of the liquid (σ), thus can be obtained by $\sigma = \frac{F}{L \cos \theta}$. Here, L is the wetting perimeter, $L = 2(b + l)$. With this equation, the surface tension of the PS solutions were measured to be $\sigma \sim 72 \pm 1$ mN/m.
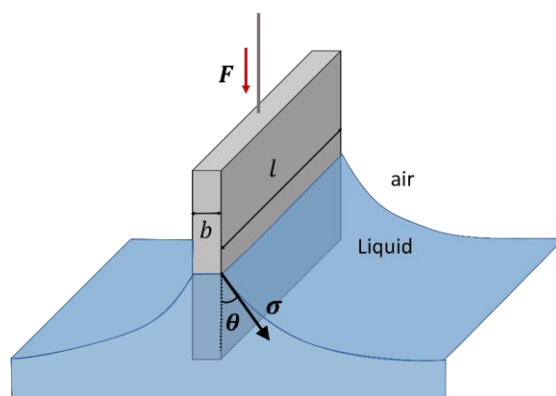
Figure 34. Schematic of the Wilhelmy plate method for measuring surface tension.

3.2.5 Optical measurement

With a laser scanning confocal microscope (with a 20×/0.75 multi-immersion objective), the evolution of water droplets (dispersed with PS particles) evaporating on oil-coated surfaces was recorded. The corresponding configurations of an evaporating droplet and the internal flows inside the droplet were recorded.

To examine the evaporating water droplet configurations, the water phase was first dyed with Alexa 488 ($\lambda_{exc} = 493$ nm, 0.01 mg in 10 ml water, Fisher Scientific Ltd.) and the silicone oil was dyed with Nile red ($\lambda_{exc} = 563$ nm, 0.03 mg in 10 ml silicone oil, Fisher Scientific Ltd.). Microliter-sized droplets (0.05-0.2 μL) were dropped onto the oil-coated substrate. Then the

configuration of the droplet, near its base as well as near its apex, was observed by the CLSM. Besides, the configuration at the droplet base was also examined by the reflection interference technique.[157-158] Refractive indices: silicon oil: 1.422; water: 1.33.

To visualize the internal flows in the droplet, fluorescent PS particles (with a diameter of 2.5 μm, concentration of 1.2×10^8 beads/ml, excited at $\lambda_{exc}= 561$ nm) were dispersed in the water phase. In this case, silicon oil was dyed with Coumarin 6 (with a concentration of 0.05 mg/ml and excited by a blue laser $\lambda_{exc} = 458$ nm). Fluorescent images in *xzt* mode (images perpendicular to the substrate) were obtained by confocal microscopy for further analysis. Additionally, an optical microscope (Carl Zeiss Axiotech Vario 100HD, 10× objective) was used to record the droplet evaporation process to provide a top view. In addition, the dried depositions on the oil-coated surface were observed by SEM and the optical microscope (Carl Zeiss Axiotech). The corresponding deposition height profiles were optically measured by the Nanofocus microscope.

In addition, a thin-film interference technique was introduced to visualize the oil film between the sessile droplet and the solid substrate.[157-159] A monochromatic incident light with intensity I_0 is first reflected at the oil/glass interface, gives rise to ray I_1; the transmitted light is further reflected at the water/oil interface and gives a ray I_2 (**Figure 35**). These two reflected lights interfere with each other and give bright or dark fringes. The resultant interfere light intensity I, thus is given by $I \sim I_1 + I_2 + 2\sqrt{I_1 I_2}\, cos\, \varphi$,[160] where φ is the phase difference between I_1 and I_2. This interfere technique allows us to detect thin films with a thickness down to a few nanometers. Therefore, the confocal microscope was used to scan the glass surface with a monochromatic laser beam with a wavelength $\lambda_{exc}= 458$ nm and capture the two reflected lights.
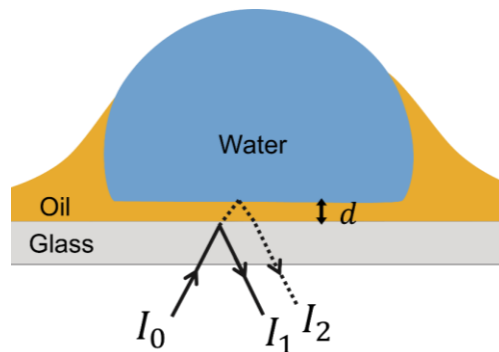
Figure 35. Schematic of the thin-film reflection interference technique.

3.3 Features of the depositions

To investigate the suppression of the "coffee ring" effect on the oil-coated surface, a contrast experiment by depositing droplets on both oil-coated surfaces (a silicone oil-coated surface was used in this work) and normal glass substrates was done. The snapshots of sessile droplets evaporating on both surfaces are shown in **Figure 36**.
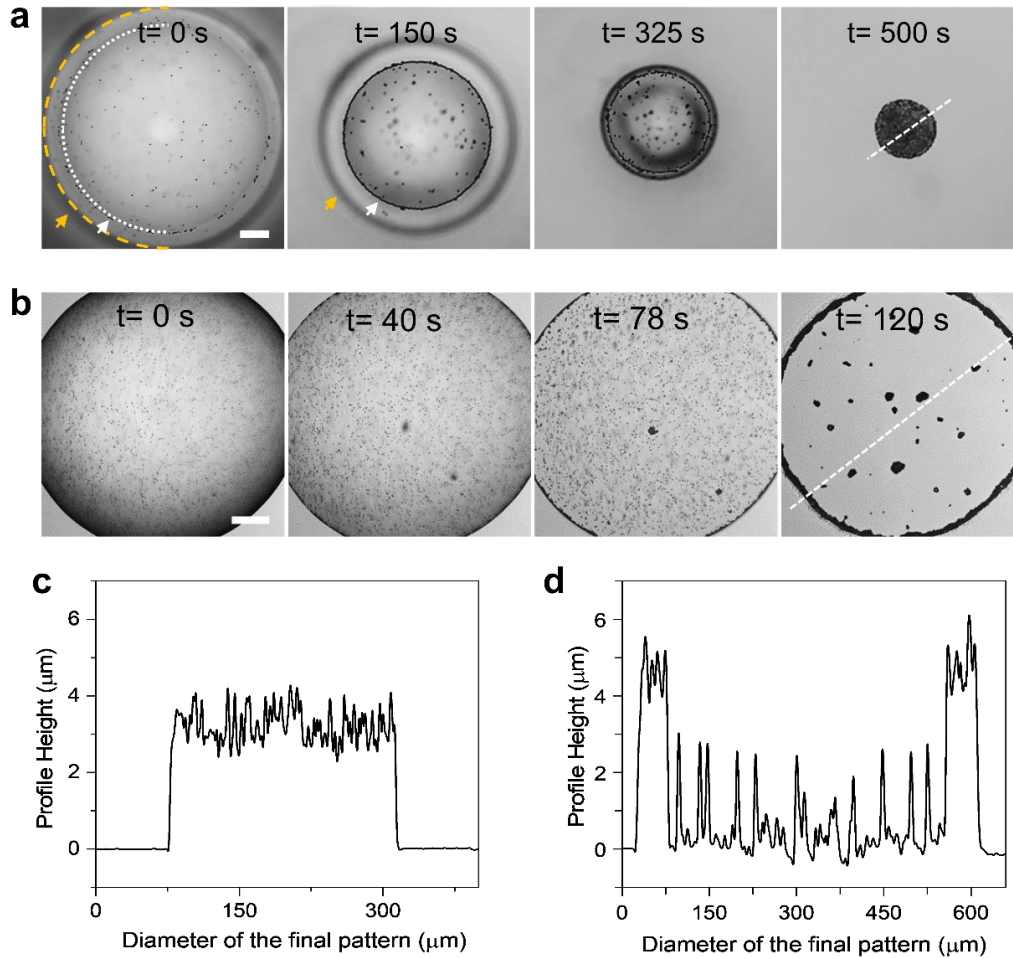
Figure 36. Snapshots of sessile droplets evaporating on (a) a silicone oil-coated surface and (b) a bare glass surface, respectively. Water droplets containing PS colloids (with an average diameter of 2.5 μm) with a concentration of 0.15 vol% and an initial volume of 0.5 μL were deposited on both surfaces. In (a), two particle-packed lines were observed on the evaporating droplet: an outer line near the droplet base (yellow) and an inner line at the droplet upper portion (white). The initial oil coating thickness before depositing droplets was 10μm. (c)(d) The final deposit profiles on surfaces correspond to the depositions marked with white dashed lines in (a) and (b), respectively. Scale bars: 100 μm. Reprinted with permission from Ref..[116]

58

Sessile droplets on the oil-coated surface present two apparent lines in their evaporating process. (**Figure 36a**). One line is the contact line located at the droplet base. The other line is located at the upper portion of the droplet, where the oil phase approaches the droplet surface, and particles have aggregated there. During the evaporation process ($t \leq 325$ s), both lines retract inward to the droplet center, and the outer line retracts faster than the inner one. With the droplet volume reducing during evaporation ($t > 325$ s), the outer line seems to merge with the inner line. During this period, pinning on the substrate was observed regularly. Finally, a concentrated deposition forms on the oil-coated surface, as shown in **Figure 36c.** While on the bare glass substrate, one line with particles aggregated is shown on the droplet surface (**Figure 36b**). This contact line was almost pinned in the droplet drying process and ultimately formed a "coffee ring" pattern (**Figure 36d**).

The evaporation-induced coffee ring effect has been successfully suppressed on the oil-coated surface. How does it occur? Is the hindered evaporation at the droplet periphery diminishing the capillary flows in the droplet? Or is it happening because of the droplet periphery depinning on the oil-coated surface? To investigate the corresponding mechanism, further investigation of the droplet morphology and its evaporating behavior on the oil-coated surface was done.

3.4 Droplet configurations

The morphology of the sessile droplet on the oil-coated surface was investigated from two regions: near the upper liquid surface where the oil film approaches the droplet surface (**Figure 37**) and at the droplet base (**Figure 38**).

In this work, the coated oil phase (silicone oil) has a lower surface tension than the droplet phase (water). The interfacial tensions between the water, oil and air phase ($\gamma_{la} = 72$ mN/m, $\gamma_{oa} = 20$ mN/m and $\gamma_{lo} \approx 45$ mN/m) gives a positive spreading efficient $S_{ol(a)} = \gamma_{la} - \gamma_{lo} - \gamma_{oa} > 0$.[119] Therefore, the silicone oil is expected to "cloaking" the sessile water droplet (**Figure 37**). The theoretical thickness of the cloaking film B, can be calculated from the balance of the disjoining pressure originating from the van der Waals force and the Laplace pressure caused by the droplet curvature: $B = (A_H R / 12\pi\gamma_{oa})^{1/3}$ (Equation (3-3)). For droplets with a few microliter sizes, B is in the range of a few nanometers, ~10 ± 2 nm.
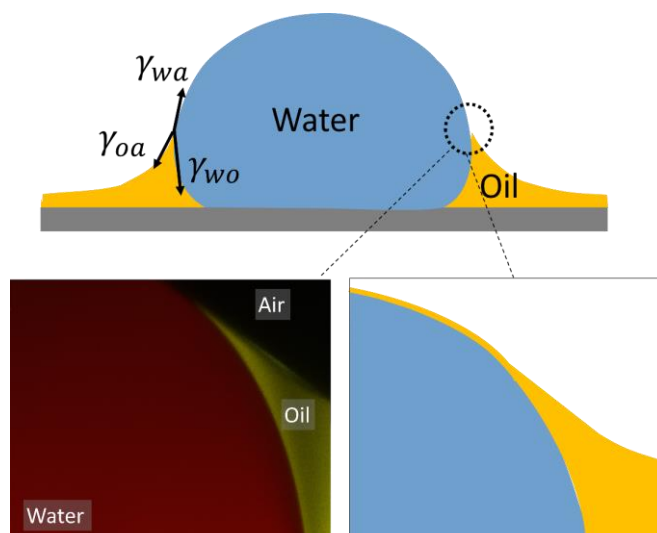
Figure 37. Side view of a sessile droplet edge on an oil-coated surface. An apparent wetting ridge is formed around the droplet. The enlarged images show the corresponding confocal image in false colors and the schematic of the droplet configuration. (Yellow: silicone oil, dyed with Nile red; Red: water droplet dyed with Alexa 457).

However, the "wrapping over" oil film at the droplet apex is too thin to be distinguished by a confocal microscope (the fluorescent image in **Figure 37**). Such a thin oil film hardly hinders the evaporation from the droplet apex. Thus, the oil phase is assumed to form an apparent "wetting ridge" around the sessile droplet. We should note that B is a dynamic parameter determined by the droplet curvature and becomes thicker in the droplet evaporating process.

Then the morphology at the bottom of the sessile droplet was investigated. Two possible configurations are illustrated in **Figure 38**: a thin oil film is sandwiched between the water droplet and the solid substrate, or the droplet is directly sitting on the solid substrate by expelling the oil film. The behavior can be predicted by the spreading coefficient $S_{ol(s)} = \gamma_{ls} - \gamma_{lo} - \gamma_{os} = -\gamma_{lo}(\cos\theta_{oil} + 1)$ (equation (3-4)) determined by the interfacial tension difference between the water, oil and solid phase. On hydrophobic surfaces, When $S_{ol(s)} > 0$, the water droplet is sitting on the oil film (**Figure 38a**), otherwise the droplet directly wets the solid substrate (**Figure 38b**). Thus, the wettability of the solid surface plays a key role in creating the droplet morphology at its base.
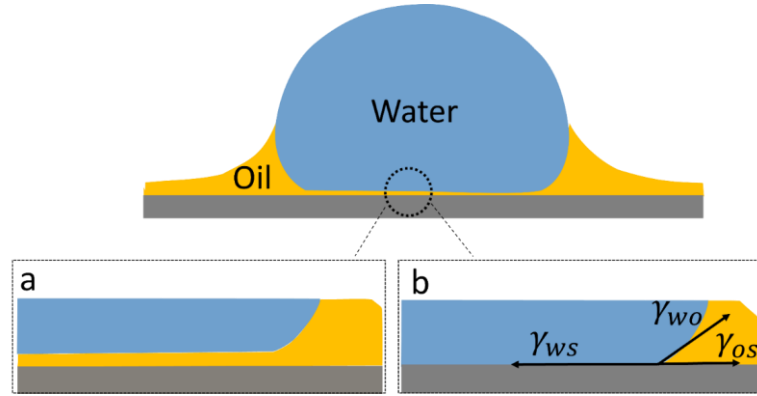
Figure 38. Schematic of the possible morphologies at the droplet base on the oil-coated surface. (a) The droplet is indirectly sitting on the substrate (an oil film sandwiched between the droplet and the substrate); (b) The droplet is in direct contact with the solid substrate.

3.5 Mechanism of suppressing the coffee ring effect

3.5.1 Contact line depinning effect

The role of the droplet pinning on the oil-coated surface was first investigated. As discussed before, the substrate wettability determines whether there is an oil film underneath the droplet or not. The existence of the oil film may help the droplet contact line depinning on the substrate during its evaporation. Hence, contrast experiments on hydrophobic surfaces ($\theta_{adv} \approx 102 \pm 3\,°$, $\theta_{rec} \approx 92 \pm 5\,°$) as well as hydrophilic surfaces ($\theta_{adv} \approx 75 \pm 3\,°$, $\theta_{rec} \approx 40 \pm 6\,°$) were done (**Figure 39**).

When a water droplet is deposited on the oil-coated hydrophobic surface ($\theta_{oil} = 177 \pm 3\,°$), $S_{ol(s)} = 0$, an oil film is predicted to be presented underneath the droplet. A thin-film interference technique was introduced to verify its existence.[157-159] In this case, interference patterns were observed by the confocal microscope, indicating a thin oil film remains underneath the droplet (**Figure 39a**). On the other hand of the oil-coated hydrophilic surface ($\theta_{oil} = 135 \pm 5\,°$), $S_{ol(s)} = -13.7$ mN/m, the water droplet is predicted to repel the oil phase and directly deposit on the solid substrate. No interference pattern was captured in this case (**Figure 39c**). Since the interference technique allows us to detect thin films with thickness down to nanometers, the droplet was considered to directly depositing on the hydrophilic surface. **Figure 39b** and **Figure 39d** show that after droplet drying on these two surfaces, concentrated depositions are observed, illustrating suppression of the "coffee ring" effect realized on surfaces regardless of their wettability. Thus, the presence of the oil film under the

sessile droplet, which determines the droplet's continuous depinning on the substrate, is not critical for suppressing the "coffee ring" effect.
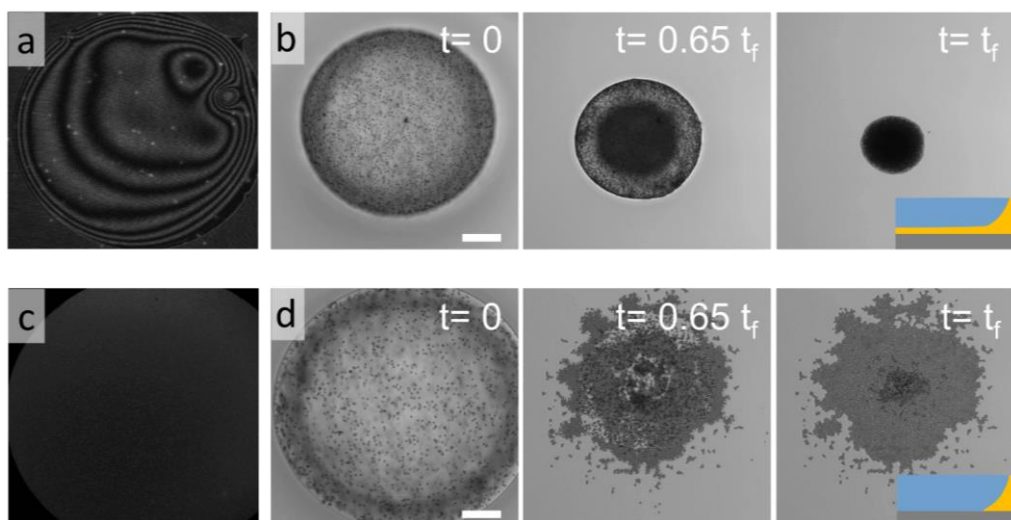
Figure 39. The morphology of the droplet base and the corresponding droplet evaporation process on oil-coated surfaces with different wettabilities. a,c) Interference images at the base of the sessile droplets (Bright spots: Fluorescent PS particles, 2.5 μm). In a), the interference rings are formed due to the ultrathin layer of the oil phase between the water droplet and the substrate; in c), the absence of the interference rings is proof of direct contact of the water droplet on the substrate; (b)(d) Evolution of 0.2 μL water droplets that contain colloids (0.15 vol%) evaporating on the oil-coated surface, taken by the confocal microscope with a bottom view. (a)(b) Oil-coated hydrophobic surface; (c)(d) Oil-coated hydrophilic surface. Insets: the schematic of the configuration at the droplet edge. t_f: the total evaporation time. Scale bars: 50 μm. Reprinted with permission from Ref..[116]

It should be noted that the wettability of the surface may affect the final feature of the deposit. On the oil-coated hydrophobic surface, a more concentrated deposition is obtained as the initial droplet base is smaller and retracts more efficiently due to the presence of the oil film underneath the droplet. Besides, as shown before, the continuity of the oil film underneath the water droplet can be deduced by calculating the Hamaker coefficient A_H of the disjoining pressure, which originates from the van der Waals force between the water-oil and the oil-solid interface. As $A_H > 0$, a stable and continuous oil film forms between the sessile droplet and the hydrophobic substrate.

3.5.2 Outward flows suppression due to controlled evaporation

The possible mechanism of hindering evaporation at the droplet periphery by changing the internal flows of the droplet was also investigated. The flow pattern in the evaporating droplet was visualized by dispersing fluorescent tracers (PS, 2.5 μm, 0.015 vol%) in the droplet and observed by the confocal microscope. The tracer trajectories showed that upward flows were formed in the evaporating droplet (**Figure 40**). There is no outward capillary flow observed in the droplet, indicating that the evaporation at the droplet periphery is un-favored and mostly occurs at its apex. Additionally, the particles settled at the upper droplet interface were also observed to be transported downward along the interface (the white arrows in image t=26 s in **Figure 40**). This phenomenon showed that weak fluid convections were also formed in the evaporating droplet on the oil-coated surface. Hence, the formed oil "wetting ridge" minimizes the evaporation at the droplet periphery and alters the droplet's internal flows. Ultimately, the suppression of the "coffee ring" effect is achieved for the droplet drying on the oil-coated surface.
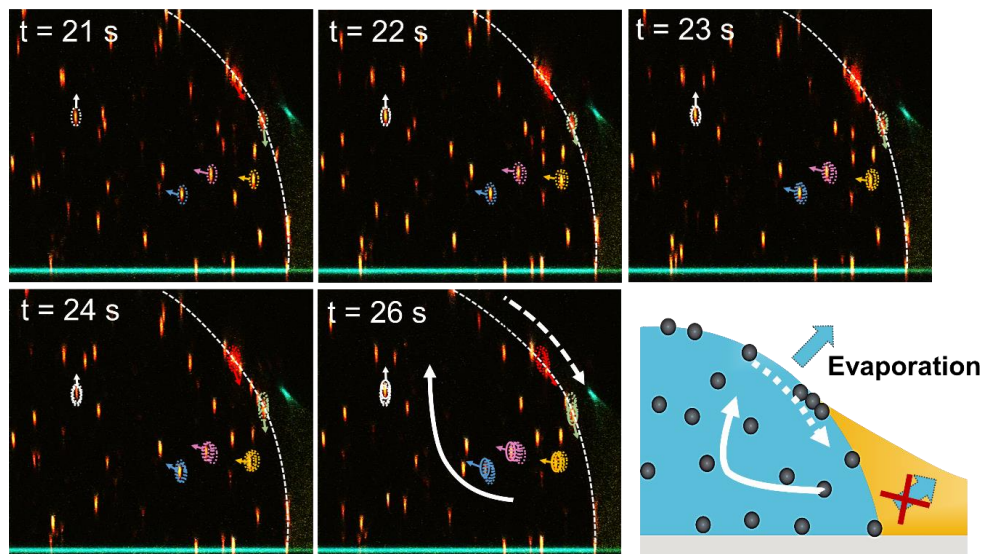
Figure 40. The trajectory of tracers in the evaporating droplet. Tracers in the droplet are moving upward while a few tracers at the droplet interface flow downward. Several tracers are marked with different colors to visualize the flows inside the droplet. Small arrows: the motion of particles; Large arrows: the main flows inside the droplet. Orange: Fluorescent traces (PS microbeads, 2.5 μm); Yellow: oil phase; Cyan: reflection from interfaces. The schematic image shows that the hindered evaporation at the droplet periphery (blue arrows) induces upward flows in the droplet (white curved arrow). Reprinted with permission from Ref..[116]

3.6 Contact line, contact angle and particle deposition behaviors

To gain more insight into droplets drying on oil-coated surfaces, their dynamic changes, such as the evolution of droplet base radius and the corresponding contact angles, the tracers' motion, and substrates with different wettability, were investigated (**Figure 41**).

In the case of droplets evaporating on oil-coated hydrophobic surfaces (**Figure 41a**), the periphery of the sessile droplet continuously shrinks and is retracting. In the initial evaporation process (0 to 280 s), the particles dispersed in the liquid were driven upward and captured by the declining upper droplet interface. Besides, the particles near the droplet base were further driven inwards by the retracting droplet contact lines. There were nearly no particles left on the hydrophobic surface. As evaporation continues (280 to 390 s), more and more particles settled at the upper droplet surface and were packed into a viscous colloidal skin. The droplet periphery began to pin on the substrate. The fully packed skin began to collapse and is ultimately deposited on the substrate to form a concentrated deposit on the oil-coated hydrophobic surface.

The depositing behavior of particles from droplets evaporating on oil-coated hydrophilic surfaces was similar (**Figure 41b**). The dispersed particles were driven upward and attached to the upper droplet interface. With the evaporation of the droplet, a significant difference occurs near the droplet periphery on the hydrophilic surface. In the images taken between $t = 120$ and 320 s, the particles near the periphery were left on the substrate instead of retracting with the shrinking droplet contact line. The reason is that the droplet completely expelled the oil film from underneath, allowing particles near the droplet base to attach to the hydrophilic surface. As more and more dispersed particles aggregated at the upper droplet interface, the deformation of the interface due to contact line retraction becomes more difficult. This lead to the pinning of the droplet on the surface ($t = 320$ to 370 s). Finally, a large and flat deposition was left on the oil-coated hydrophilic surface. The corresponding 3D particle deposition evolution was shown in **Figure 43**.

The temporal evolution of the deposition size (r) and the instant droplet contact angle (θ, near the droplet periphery) were given in **Figure 42** (corresponding to **Figure 41**). The droplet deposition radius was continuously decreasing on oil-coated hydrophobic surfaces while the corresponding contact angles reduced slowly (from 100 to 280 s, **Figure 42a**). After $t = 280$ s, the droplet contact line remained pinned on the substrate, and the corresponding contact angle decreased faster than before. On the contrary, on the oil-coated hydrophilic surface, the droplet's deposit radius barely retracted in its evaporation process (**Figure 42b**). The instant

contact angle of the droplet continuously decreased in the whole evaporation process, which is always smaller than that on the oil-coated hydrophobic surface.

Therefore, the droplet evaporation process on the oil-coated surface can be summarized into two stages (**Figure 44**): In the first stage (stage I), the baseline of droplets retracts continually, and most of the colloids inside the droplet are driven to the upper interface to form a particle-packed monolayer; in the second stage (stage II), the droplet baseline begins to pin on the substrate due to the high Laplace pressure caused by droplet curvature. As the droplet volume continues to shrink, the particles-packed interface is receding towards the substrate and ultimately forms a concentrated deposit instead of a "coffee ring" pattern.
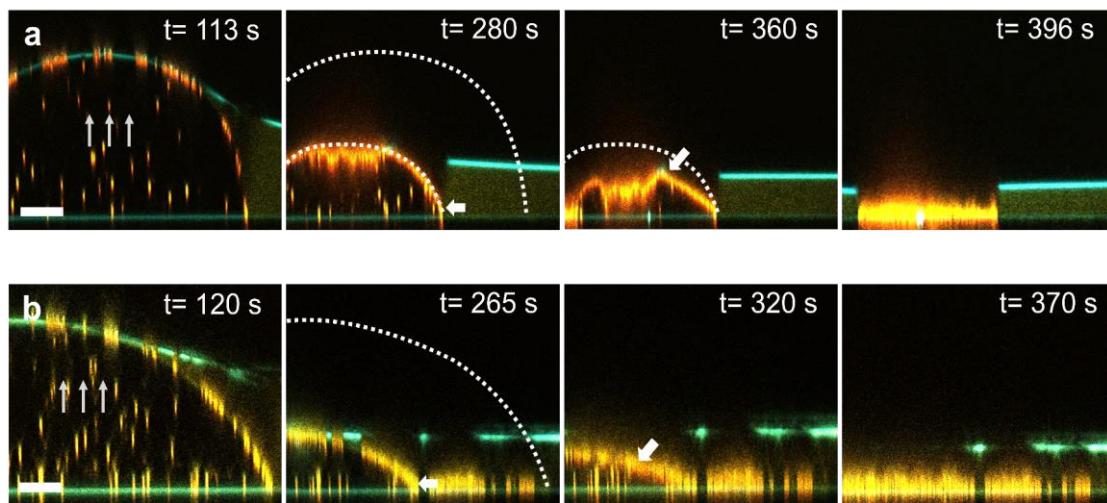
Figure 41. Evolution of sessile droplets containing PS microbeads (orange) evaporating on oil-coated hydrophobic (a) and hydrophilic (b) surfaces, respectively. White dotted lines: (previous) droplet profiles; Thick arrows: the retracting droplet edge and declining droplet surface; Thin arrows: transport direction of the tracer. Yellow: oil phase; Cyan: reflections from interfaces. Scale bars: 50 μm. Reprinted with permission from Ref..[116]
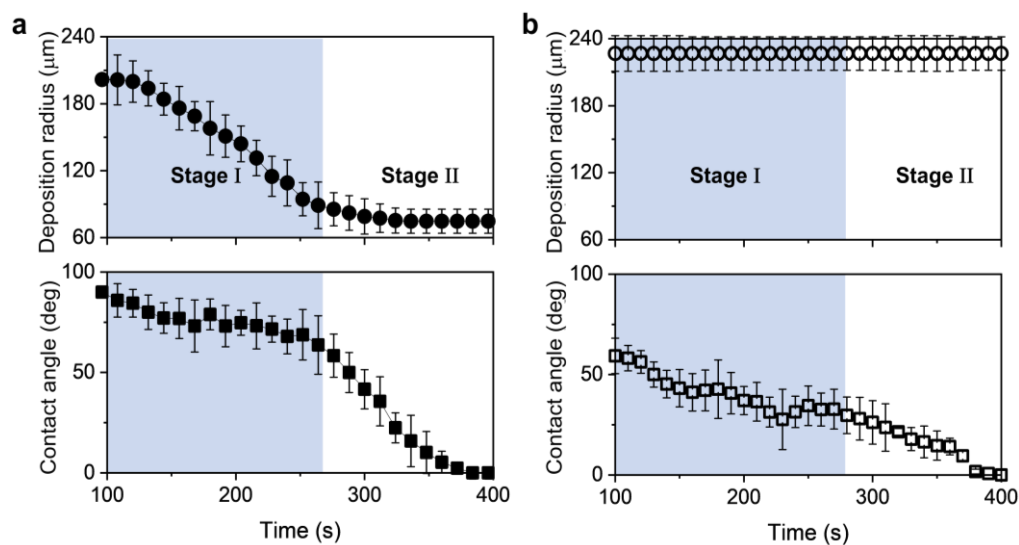
Figure 42. Evaporation kinetics of droplets, characterized by the deposit base radius (R) and the instant droplet contact angles (θ) on oil-coated hydrophobic (solid symbol) and hydrophilic (hollow symbol) surfaces, respectively. Blue background: the stage of the droplet retracting process. Reprinted with permission from Ref..[116]
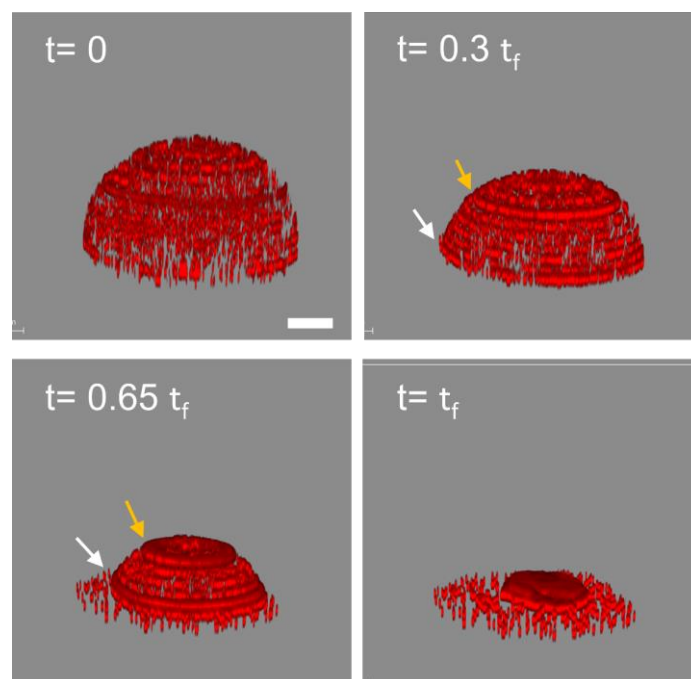
Figure 43. 3D reconstruction of particle assembly inside the evaporating droplet (0.05 μL, 0.1 vol%) on the oil-coated hydrophilic surface via confocal 3d microscopy. Two particle-aggregated line on the evaporating droplet were observed (colored arrows). Reprinted with permission from Ref..[116]
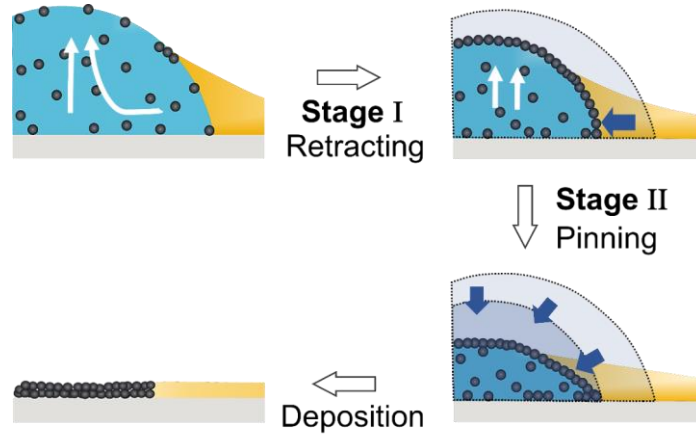
Figure 44. Schematic of droplets evaporating on oil-coated surfaces. The evaporating process is summarized into two stages: a gradual contracting process in most of the evaporating period (Stage I) and a pinning process in the final drying period (Stage II). White arrows: liquid flows in the droplet; Blue arrows: Retraction of the droplet interface. Reprinted with permission from Ref..[116]

One thing to note, the dispersed particles prefer to accumulate at the upper droplet interface rather than to move back to the bulk liquid. Two factors induce this phenomenon: (1) Upward flows in the evaporating droplet drive particles to the upper droplet interface. (2) Particles trapped at the droplet interface are in a thermodynamically stable state. As mentioned before, the initial oil film on the droplet apex was calculated to be approximately 10 nm. At the same time, the particles used in the experiments were 2.5 μm. Once the particles settled on the droplet apex, the particles were directly in contact with the air atmosphere. Hence, the droplet interface near the droplet apex can be assumed to be a bare liquid-air interface. For each particle trapped here, the corresponding binding energy ΔE between a particle and the liquid-air interface is addressed with the equation $\Delta E = -\pi R^2 \gamma_0 (1 - (\gamma_2 - \gamma_1)/\gamma_0)^2$, where R is the particle radius, $\gamma_0, \gamma_1, \gamma_2$ are the interfacial tensions of the water-air, particle-water and particle-air interface, respectively.[161-162] We assume the particles rest at the liquid-air interface have an almost equal affinity for water and air. Therefore, the binding energy ΔE of micro-particles is calculated to be around 10^{-10} mN·m. For nanoparticles, $\Delta E \approx 10^{-16}$ mN·m. Correspondingly, the energy for particles detach from the interface due to Brownian motions can be expressed as $\varepsilon = k_B T$, where k_B is the Boltzmann's constant and T is the absolute temperature, $T = 298$ K. $\varepsilon \approx 10^{-21}$ mN·m, which is less than the corresponding binding energy for micro-/nanoparticles at the liquid-air interface. Therefore, these micro/nano-particles are more likely

to be trapped at the liquid-air interface to keep their thermodynamic stability. In this study, we have neglected the particle-particle interactions at the liquid-air interface.

3.7 Constant contact angle evaporation mode

Jian *et al.*[2] have reported that evaporation from droplets on such surfaces can be considered only to occur above the height of the oil wetting ridge (h_s), as illustrated in the schematic in **Figure 45a**. A contrast experiment of droplets evaporating on bare hydrophobic and oil-coated surfaces has been done. On both surfaces, droplets all experience receding of their base radius in most of their evaporation process ($t \sim \frac{3}{4} t_{\text{evap}}$). The corresponding evaporation curves are shown in **Figure 45b**.
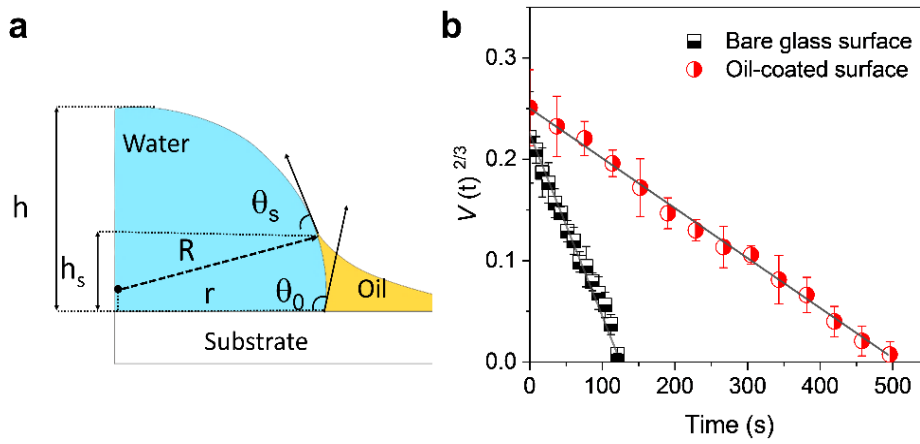
Figure 45. Droplet evaporation on oil-coated surfaces. (a) A schematic of the cross-section of a sessile droplet on the oil-coated surface. An "oil wetting ridge" formed at the base of the droplet. (b) The evolution of 0.1 μL droplets evaporating on a glass substrate and an oil-coated surface, respectively. The fit curves show the volume of droplets ($V(t)^{2/3}$) with the function of time. Oil phase: 100 cSt, 20 μm. Reprinted with permission from Ref..[116]

In **Figure 45b**, the droplet volume curve shows that a significant delay occurs for droplets evaporating on oil-coated hydrophobic surfaces compared to droplets evaporating on solid hydrophobic surfaces. This time delay verifies that the oil "wetting ridge" reduces the droplet evaporation, which can be expressed by a factor of $[1 - h_s/h_0]$. At the same time, the droplet volume $V(t)$, showed a relationship of $V(t)^{2/3}$ linearly decreasing with the evaporation time t on both hydrophobic surfaces. Therefore, the evaporation of droplet evaporating on oil-coated surfaces follow $V(t)^{2/3} \approx V_i^{2/3} - \frac{4\lambda}{3} \left[\frac{3}{\pi \beta(\theta_0)} \right]^{1/3} f(\theta_s) t$ (equation   (3-13)). Even though the

evaporating droplets undergo slow contraction of their peripheries, similar evaporating curves were observed. Thus, the evaporation of the sessile droplet on the oil-coated hydrophilic surface can also be theoretically analyzed by this equation.

3.8 Deposit features on surfaces with different wettability

To investigate the suppression of the "coffee ring" effect on the oil-coated surfaces, some experimental parameter, such as surface wettability (hydrophobic or hydrophilic), oil properties (a viscosity in the range of 10 to 10^5 cSt, oil film thickness 1-20 μm), colloid concentration (0.015-1.5 vol%) as well as droplet sizes (0.01-2 μL), were examined.

The role of the substrate wettability was first investigated by evaporating 0.2 μL droplets (containing PS particles) on oil-coated hydrophobic ($\theta_{adv} \approx 102 \pm 3$ °, $\theta_{rec} \approx 92 \pm 5$ °) and oil-coated hydrophilic ($\theta_{adv} \approx 75 \pm 3$ °, $\theta_{rec} \approx 40 \pm 6$ °) surfaces, respectively. The corresponding "phase" diagrams of the drying features were shown in **Figure 46**. The diagram shows that the coffee ring's suppression occurs on both - oil-coated hydrophobic and hydrophilic surfaces - regardless of the viscosity of the coated oil or its layer thickness. Notably, the initial oil film thickness has to be sufficient enough to form a "wetting ridge" to prevent evaporation at the droplet periphery. The critical thickness of the oil coating on hydrophobic surfaces was 1 μm (**Figure 46a**), while it must be large than 3 μm on hydrophilic surfaces (**Figure 46b**). Besides, for oil with high viscosity (>1000 cSt), the oil coating thickness can be decreased to 1 μm on the hydrophilic surface. This difference indicated that the existence of the high-viscosity oil film underneath the droplet (which is hardly to be expelled by water droplets due to its high viscosity) helps droplets to retract on hydrophilic surfaces.

Figure 46. "Phase" diagram of the suppression of "coffee ring" effect on oil-coated surfaces. Uniform depositions are marked with solid squares (□) on a hydrophobic surface (a), while in (b) by hollow triangles (△) on a hydrophilic surface; Coffee ring patterns are noted with crosses (×). Dashed black lines represent the critical thickness of the oil coating. Reprinted with permission from Ref..[116]

Then the fate of droplets with different particle concentrations was investigated. **Figure 47** shows the optical images of final depositions by drying 0.2 μL droplets dispersed with PS particles with different concentrations (in the range of 0.015 to 1.5 vol%) on oil-coated surfaces. On oil-coated hydrophobic surfaces, the size of the depositions increases with the increase of the dispersed particle concentrations (**Figure 47a**). In contrast, the deposition sizes did not change with particle concentrations for droplets evaporating on oil-coated hydrophilic surfaces (**Figure 47b**). The corresponding curve of deposition diameter to the droplet concentration is shown in **Figure 48**. The difference in droplet deposition behaviors indicates that the drying

deposition features on oil-coated surfaces can be controlled by adjusting the solid surface wettability.
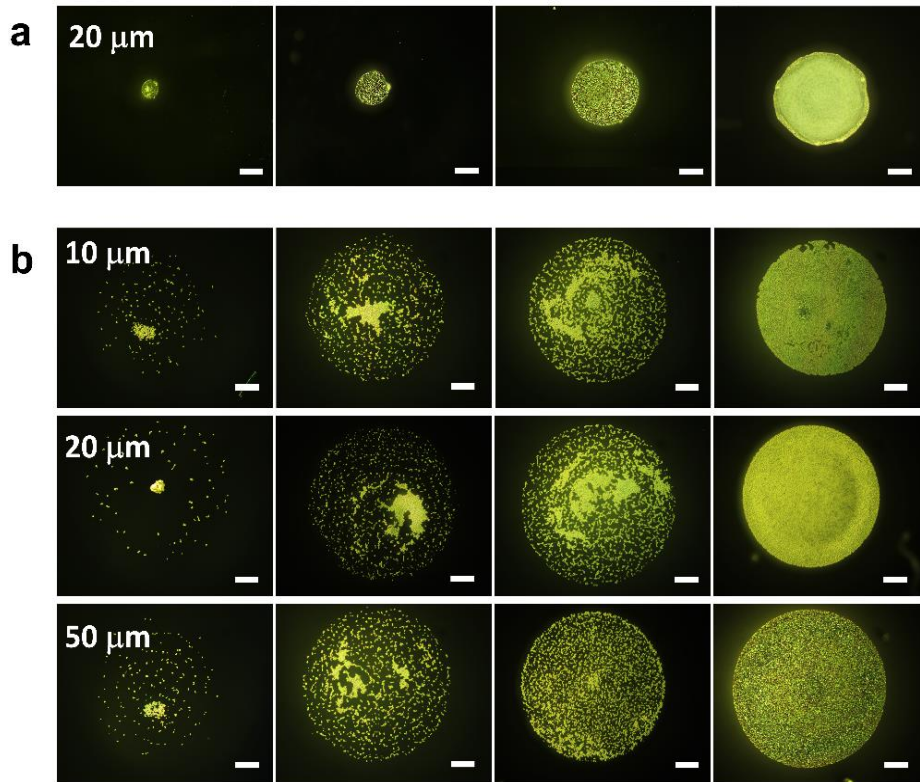
Figure 47. Dried depositions of droplets containing PS particles (3 μm, 0.2 μL) on oil-coated surfaces. (a) Depositions on oil-coated hydrophobic surfaces. The initial oil film thicknesses are 20 μm. (b) Depositions on oil-coated hydrophilic surfaces. Columns with an increase of the oil thickness (from 3 to 50 μm) while rows present a variation of the initial concentrations in evaporating droplets (increased from 0.015 to 1.5 vol%). Scale bars: 100 μm. Reprinted with permission from Ref..[116]
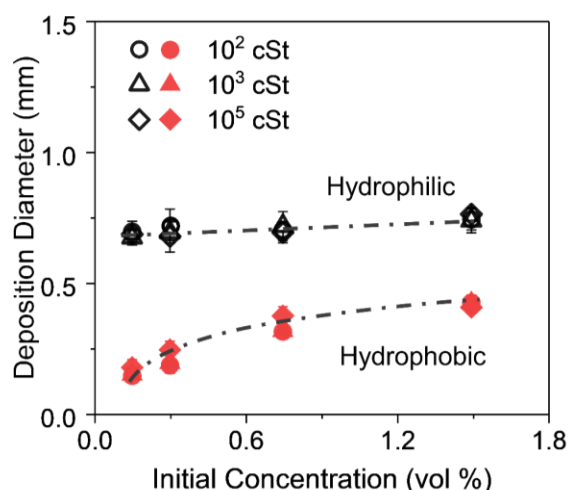
Figure 48. The size of depositions on oil-coated surfaces with different oil viscosities and the variation of PS concentration in the evaporating droplets. Reprinted with permission from Ref..[116]
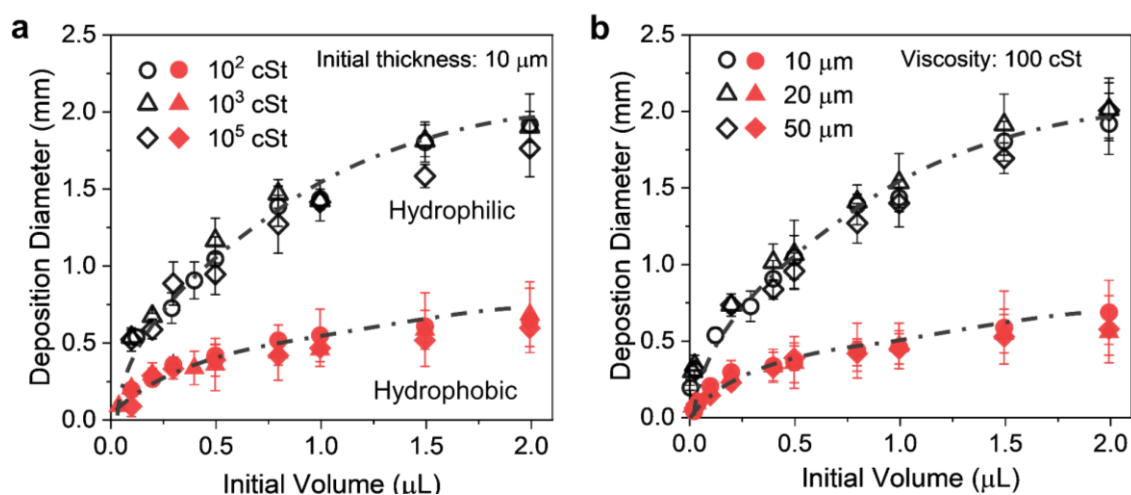
Figure 49. Influence of the initial volume of the colloidal droplet and the oil property (viscosity and thickness) on the deposition features. The size of depositions varied with the initial droplet size, (a) oil coating with different viscosities and (b) oil coating with different thicknesses. Lines: a guide for the eye. Reprinted with permission from Ref..[116]

Other parameters, such as the volume of the evaporating droplet (0.01 to 2 μL), and oil coatings with different viscosity and thickness (viscosity, 10^2 to 10^5 cSt; initial oil thickness, 10 to 50 μm), were also investigated (**Figure 49**). The size of the final depositions shows an increase from a few tens of micrometers to millimeters with the increasing initial droplet volumes (**Figure 49a**). The data were located on two distinct curves: for hydrophobic and for the hydrophilic case. On oil-coated hydrophilic surfaces, larger depositions were obtained. Similar

relationships were observed with the variation of the oil coating thickness (**Figure 49b**). These two results showed that the feature of final depositions on oil-coated surfaces depended on the substrate wettability, while rarely was affected by the oil coatings. The difference of the depositions features on oil-coated surfaces with different wettability indicates its ability to prepare depositions in a controlled manner, which further shows its potential in surface patterning applications.

3.9 Application: producing asymmetric supraparticles

Evaporation of droplets containing micro/nanoparticles on superhydrophobic and superamphiphobic surfaces has been reported as a straightforward approach to fabricate supraparticles.[163-166] However, the complicated process of constructing hierarchal structures on solid surfaces and the limitation of droplet volumes restrict their applications in manufacturing ultra-small supraparticles (radius $R < 5$ μm)[165]. Since the evaporating droplets may suffer Cassie-Wenzel wetting transitions due to the increasing Laplace pressure (when the droplets are getting smaller and their sizes are comparable to the surface roughness). For instance, the critical impalement pressure on a cylindrical pillar surface is given by $P^{\max}(1 - \phi) = -\frac{2\pi R\gamma}{A}\cos\theta_{\mathrm{adv}}$, [167-170] where R is the pillar radius; A is the area per pillar occupied, $A = a^2$; ϕ is the solid area fraction of the pillar surface, $\phi = \pi R^2/A$; γ is the surface tension on the liquid-air interface and θ_{adv} is the apparent advancing contact angle. The limitation of the droplet size is that it should be larger than the nano- or microstructures of the superhydrophobic surfaces, typically larger than 10 μm.

In this work, droplets drying on oil-coated hydrophobic surfaces to produce supraparticles were studied. The stable thin oil film sandwiched between the droplet and the hydrophobic substrate helps droplets to recede easily without pinning in most of their evaporation processes. Besides, the flat features of oil-coated surfaces provide the possibility of drying droplets with ultra-small sizes, *i.e.,* nano-/pico-liter droplets, by avoiding the liquid penetrating into the rough structures of the substrate. **Figure 50** shows the supraparticles of micro/nanoparticles with various sizes obtained on oil-coated hydrophobic surfaces.
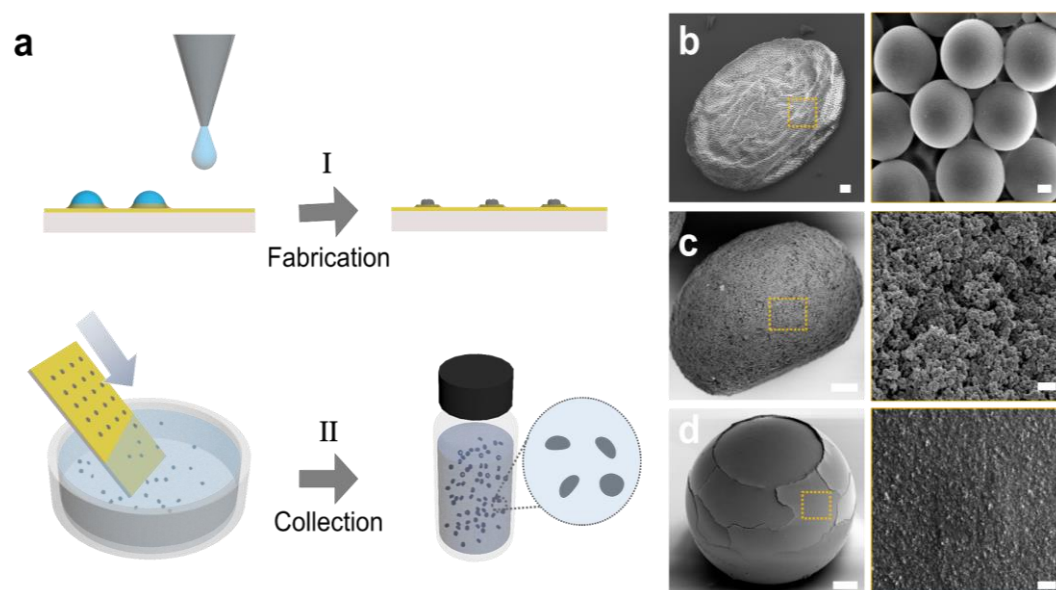
Figure 50. Supraparticle production on oil-coated hydrophobic surfaces. (a) Schematic images of the fabrication and collection process of supraparticles. SEM images in the right part shows supraparticles self-assembled by the following particles: (b) PS (1 μm, 0.1 vol%), (c) TiO$_2$ (25 nm, 0.1 vol%) and (d) carbon diamond seeds (20 nm, 0.1 vol%). Scale bars: 20 μm. Images on the right side of (b)-(d) show the close-up view of the porous microstructures. Scale bars: 1 μm. Reprinted with permission from Ref..[116]

The schematic of the fabrication and collection of supraparticles is illustrated in **Figure 50a.** By depositing droplet arrays on oil-coated hydrophobic surfaces, the simultaneous evaporation of the volatile liquid in the droplets helps particles self-assemble to supraparticles. Then by simply immersing the supraparticle-loaded substrate in hexane solution, batches of supraparticles were detached from the substrate and can be easily collected in one chamber. **Figure 50b-d** show SEM images of supraparticles prepared by drying droplets dispersed with different micro/nanoparticles: PS (3 μm, 0.1 vol%), TiO$_2$ (25 nm, 0.1 vol%) as well as carbon diamond (20 nm, 0.1 vol%), respectively. The supraparticles showed various shapes from disk-like, pill-like to nearly spherical shape—the variation of their shapes are affected by the dispersed particle size and their intrinsic densities.

As micrometer-sized PS particles assembled into supraparticles in disc-like shapes (**Figure 50b**), drying droplets dispersed of nanometer-sized PS particles can assemble into pill-like shapes, as shown in **Figure 51**. This result shows that the size of the dispersed particles can affect the shape of the final supraparticles. The feature difference is because micrometer-sized particles can pack into a larger jamming area at the liquid-air interface than nanoparticles

(forms a more loosely-packed structure). Thus, the energy for interface deformation is larger. Then the droplet periphery is pinned on the substrate (corresponding to stage II in **Figure 44**), and ultimately we obtain supraparticles with larger and flatter features. Besides, the density of the dispersed particles also affects the supraparticle shape (**Figure 50c** and **d**). Two kinds of nanometer-sized particles, TiO_2 and carbon diamond, which have similar sizes but different densities, were self-assembled into supraparticles with different shapes (pill-like and nearly spherical shapes). The results indicate the possibility of producing supraparticles with defined shapes on the oil-coated surface. With this straightforward approach, batches of supraparticles were obtained. **Figure 52** shows batches of pill-like supraparticles of TiO_2, ZnO, and SiO_2 obtained on oil-coated hydrophobic surfaces.
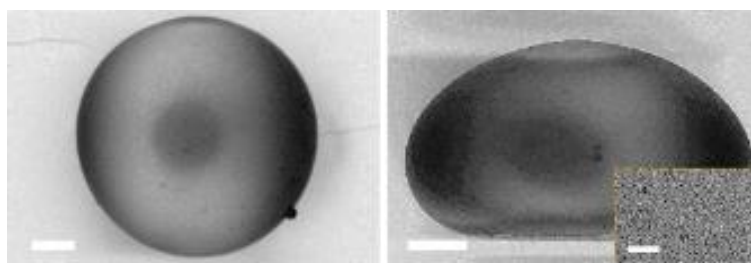
Figure 51. Supraparticle formed via self-assembly of nanometer-sized PS particles (average diameter of 68 nm). The initial concentration of PS in the drying droplets was 0.1 vol%. SEM images of the supraparticle with a top view (left) and a side (right) view. Insets: close-up of the surface structure. Scale bars: 100 μm; Insets: 1 μm. Reprinted with permission from Ref..[116]
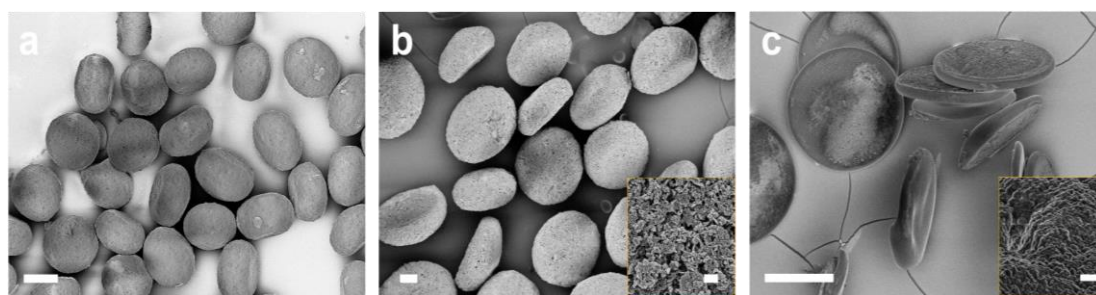
Figure 52. Batches of supraparticles obtained by drying droplets of (a) TiO_2 (25 nm, 0.1 vol%), (b) ZnO (20 nm, 0.1 vol%) and (c) SiO_2 (250 nm, 0.1 vol%) particles suspensions, respectively. Scale bars: 200 μm. Insets scale bars: 1 μm. Reprinted with permission from Ref..[116]

3.10 Summary

The mechanism of suppressing the "coffee ring" effect during droplet drying on low surface tension oil-coated surfaces has been investigated in this work. Due to the imbalance of the

surface tensions between the low surface tension oil phase and the aqueous liquid droplet and the capillary force caused by droplet curvature, the oil phase spontaneously climbs up and forms an oil "wetting ridge" around the droplet periphery. The oil "wetting ridge" plays a crucial role in altering the internal flows of the evaporating droplets. Consequently, the dispersed particles are driven upward and are captured by the declining free upper interface. Ultimately, depositions with homogeneous and concentrated features are left on oil-coated surfaces. This approach shows that the suppression of the "coffee ring" effect is realized on oil-coated surfaces. This suppression ability was not affected by the oil parameters (viscosity or film thickness) or the wettability of the solid substrate.

However, the wettability of the substrate was found to be important in determining the final deposition features. More concentrated depositions were obtained on oil-coated hydrophobic surfaces. Taking advantage of the oil-coated hydrophobic surfaces, micro/millimeter-sized asymmetric supraparticles with different shapes have successfully been fabricated. This approach shows its potential in realizing surface patterning, catalysis, and energy applications at large-scales.

4 Conclusion

In this thesis, I investigated two approaches to manipulate fluid flows in bulk liquid and droplets by introducing surface tension variation at fluid-fluid interfaces. The first one represents an active approach of triggering flow in the liquid layer by the thermocapillary effect near a superhydrophobic surface. The second shows a passive strategy of altering the streams inside evaporating droplets by utilizing interfacial deformation between liquid phases.

In the first project, I have shown that liquid flows can be triggered in a confined liquid phase in contact with a superhydrophobic surface (Cassie state) by light illumination. The liquid flows develop into convective patterns. Based on experiments and numerical simulations, I figured out that the liquid flows originate from the thermocapillary effect and the non-negligible buoyancy effect induced by the non-uniform temperature distribution near the superhydrophobic surface. In particular, the thermocapillary effect on superhydrophobic surfaces has been verified, and it can be tuned by designing surfaces with different microstructures (corresponding to slip lengths). A controlled thermocapillary flow thus is expected.

In the second project, I introduce an approach of alternating internal flows in drying droplets to suppress the so-called "coffee ring" effect. It is realized by depositing droplets on another immiscible, oil-coated substrate. Due to the interfacial tension differences of the two liquid phases in the air atmosphere, the low-surface-tension oil spontaneously forms a "wetting ridge" around the droplet periphery. This "wetting ridge" vastly reduces the evaporation at the droplet periphery, thus minimizing the outward capillary flow while inducing upward flows in the droplet. Consequently, a homogeneous deposition was left on the substrate. The surface wettability plays a critical role in defining the morphology of final drying patterns: depositions on oil-coated hydrophilic surfaces illustrate much wider and flatter features while concentrated depositions are obtained on oil-coated hydrophobic surfaces. This work has illustrated that the drying patterns on surfaces can be controlled by tuning the interfacial characteristics.

These two aspects of my PhD project provide new insights on how liquid flows can be triggered and manipulated by introducing fluid-fluid interfaces at a solid or a liquid boundary. From a technical point of view, the ability of surface tension-induced flow/deformation on the superhydrophobic and liquid-coated surfaces will find their applications in microfluidics and printing techniques.

References

[1]   Thomson, J., XLII. On certain curious motions observable at the surfaces of wine and other alcoholic liquors. *The London, Edinburgh, and Dublin Philosophical Magazine and Journal of Science* **1855,** *10*, 330.

[2]   Marangoni, C., Spreading of droplets of a liquid on the surface of another. *Ann Phys Lpz* **1871,** *143*, 337.

[3]   Hondros, E. D.; McLean, M.; Mills, K. C.; Velarde, M. G., Drops, liquid layers and the Marangoni effect. *Philosophical Transactions of the Royal Society of London. Series A: Mathematical, Physical and Engineering Sciences* **1998,** *356*, 829.

[4]   Golovin, A. A.; Nepomnyashchy, A. A.; Pismen, L. M., Pattern-Formation in Large-Scale Marangoni Convection with Deformable Interface. *Physica D-Nonlinear Phenomena* **1995,** *81*, 117.

[5]   Pearson, J. R. A., On convection cells induced by surface tension. *Journal of Fluid Mechanics* **1958,** *4*, 489.

[6]   Velarde, M. G.; Normand, C., Convection. *Scientific American* **1980,** *243*, 92.

[7]   Robert D. Deegan, O. B., Todd F. Dupont, Greb Huber, Sidney R. Nagel & Thomas A. Witten, Capillary flow as the cause of ring stains from dried liquid drops. *Nature* **1997,** *389*, 827.

[8]   Marangoni, C., Study on surface tension of fluid. *Ann. Phys. Chem* **1871,** *143*, 337.

[9]   Scriven, L. E.; Sternling, C. V., The Marangoni Effects. *Nature* **1960,** *187*, 186.

[10]   Cerisier, P.; Jamond, C.; Pantaloni, J.; Perezgarcia, C., Stability of Roll and Hexagonal Patterns in Benard-Marangoni Convection. *Physics of Fluids* **1987,** *30*, 954.

[11]   Trittel, T.; Harth, K.; Klopp, C.; Stannarius, R., Marangoni Flow in Freely Suspended Liquid Films. *Physical Review Letters* **2019,** *122*, 234501.

[12]   Maggi, C.; Saglimbeni, F.; Dipalo, M.; De Angelis, F.; Di Leonardo, R., Micromotors with asymmetric shape that efficiently convert light into work by thermocapillary effects. *Nat. Commun.* **2015,** *6*, 7855.

[13]   Troian, S. M.; Wu, X. L.; Safran, S. A., Fingering instability in thin wetting films. *Physical Review Letters* **1989,** *62*, 1496.

[14]   Bates, C. M.; Stevens, F.; Langford, S. C.; Dickinson, J. T., Motion and dissolution of drops of sparingly soluble alcohols on water. *Langmuir* **2008,** *24*, 7193.

[15]   Keiser, L.; Bense, H.; Colinet, P.; Bico, J.; Reyssat, E., Marangoni Bursting: Evaporation-Induced Emulsification of Binary Mixtures on a Liquid Layer. *Physical Review Letters* **2017,** *118*, 074504.

[16]   Baroud, C. N.; de Saint Vincent, M. R.; Delville, J.-P., An optical toolbox for total control of droplet microfluidics. *Lab on a Chip* **2007,** *7*, 1029.

[17]   Liu, G. L.; Kim, J.; Lu, Y.; Lee, L. P., Optofluidic control using photothermal nanoparticles. *Nat Mater* **2006,** *5*, 27.

[18]   Monat, C.; Domachuk, P.; Eggleton, B., Integrated optofluidics: A new river of light. *Nature photonics* **2007,** *1*, 106.

[19]   Xu, L.; Mou, F.; Gong, H.; Luo, M.; Guan, J., Light-driven micro/nanomotors: from fundamentals to applications. *Chemical Society Reviews* **2017,** *46*, 6905.

[20]   Harasima, A., Molecular Theory of Surface Tension. In *Advances in Chemical Physics*, 1957; pp 203.

[21]   Bénard, H., *Les tourbillons cellulaires dans une nappe liquide propageant de la chaleur par convection: en régime permanent*. Gauthier-Villars: 1901.

[22]   Vargaftik, N. B.; Volkov, B. N.; Voljak, L. D., International Tables of the Surface-Tension of Water. *Journal of Physical and Chemical Reference Data* **1983,** *12*, 817.

[23]   Shereshefsky, J., Surface tension of saturated vapors and the equation of Eötvös. *The Journal of physical chemistry* **1931,** *35*, 1712.

[24]   Davis, S. H., Thermocapillary instabilities. *Annual Review of Fluid Mechanics* **1987,** *19*, 403.

[25]   Winterer, F.; Maier, C. M.; Pernpeintner, C.; Lohmuller, T., Optofluidic transport and manipulation of plasmonic nanoparticles by thermocapillary convection. *Soft Matter* **2018,** *14*, 628.

[26]   Burelbach, J. P.; Bankoff, S. G.; Davis, S. H., Nonlinear stability of evaporating/condensing liquid films. *Journal of Fluid Mechanics* **2006,** *195*.

[27]   Bowen, M.; Tilley, B. S., Thermally induced van der Waals rupture of thin viscous fluid sheets. *Physics of Fluids* **2012,** *24*.

[28]   Kirkinis, E.; Andreev, A. V., Healing of thermocapillary film rupture by viscous heating. *Journal of Fluid Mechanics* **2019,** *872*, 308.

[29]   Hu, W.; Imaishi, N., Thermocapillary flow in a jet of liquid film painted on a moving boundary. *Langmuir* **2000,** *16*, 4632.

[30]   Hu, K.-X.; He, M.; Chen, Q.-S.; Liu, R., Linear stability of thermocapillary liquid layers of a shear-thinning fluid. *Physics of Fluids* **2017,** *29*, 073101.

[31] Nahas, N. M.; Panton, R. L., *Control of surface tension flows: instability of a liquid jet.* 1990.

[32] Robert de Saint Vincent, M.; Chraïbi, H.; Delville, J.-P., Optical Flow Focusing: Light-Induced Destabilization of Stable Liquid Threads. *Physical Review Applied* **2015,** *4*.

[33] Baier, T.; Steffes, C.; Hardt, S., Thermocapillary flow on superhydrophobic surfaces. *Phys Rev E* **2010,** *82*, 037301.

[34] Barthlott, W.; Neinhuis, C., Purity of the sacred lotus, or escape from contamination in biological surfaces. *Planta* **1997,** *202*, 1.

[35] Cassie, A., Contact angles. *Discussions of the Faraday Society* **1948,** *3*, 11.

[36] Amador, G. J.; Ren, Z.; Tabak, A. F.; Alapan, Y.; Yasa, O.; Sitti, M., Temperature Gradients Drive Bulk Flow Within Microchannel Lined by Fluid-Fluid Interfaces. *Small* **2019,** *15*, 1900472

[37] Yariv, E., Thermocapillary flow between longitudinally grooved superhydrophobic surfaces. *Journal of Fluid Mechanics* **2018,** *855*, 574.

[38] Yariv, E.; Crowdy, D., Thermocapillary flow between grooved superhydrophobic surfaces: transverse temperature gradients. *Journal of Fluid Mechanics* **2019,** *871*, 775.

[39] Al-Kharabsheh, S.; Yogi, D., Analysis of an innovative water desalination system using low-grade solar heat. *Desalination* **2003,** *156*, 323.

[40] Zhang, Z.; Li, X.; Yin, J.; Xu, Y.; Fei, W.; Xue, M.; Wang, Q.; Zhou, J.; Guo, W., Emerging hydrovoltaic technology. *Nature Nanotechnology* **2018,** *13*, 1109.

[41] Darabi, J.; Ohadi, M. M.; DeVoe, D., An electrohydrodynamic polarization micropump for electronic cooling. *Journal of Microelectromechanical Systems* **2001,** *10*, 98.

[42] Han, W.; Lin, Z., Learning from "coffee rings": ordered structures enabled by controlled evaporative self-assembly. *Angewandte Chemie, International Edition in English* **2012,** *51*, 1534.

[43] Das, S.; Dey, A.; Reddy, G.; Sarma, D. D., Suppression of the Coffee-Ring Effect and Evaporation-Driven Disorder to Order Transition in Colloidal Droplets. *J Phys Chem Lett* **2017,** *8*, 4704.

[44] Deegan, R. D.; Bakajin, O.; Dupont, T. F.; Huber, G.; Nagel, S. R.; Witten, T. A., Capillary flow as the cause of ring stains from dried liquid drops. *Nature* **1997,** *389*, 827.

[45] Deegan, R. D., Pattern formation in drying drops. *Physical Review E* **2000,** *61*, 475.

[46] Getling, A. V., *Rayleigh-B nard Convection: Structures and Dynamics.* World Scientific: 1998; Vol. 11.

[47]   Yang, W.-J.; Guo, K.-H.; Sakamoto, M., Evaporation-induced cellular convection in thin liquid layers. *EXPERIMENTAL HEAT TRANSFER An International Journal* **1997,** *10*, 191.

[48]   Bassou, N.; Rharbi, Y., Role of Benard− Marangoni instabilities during solvent evaporation in polymer surface corrugations. *Langmuir* **2009,** *25*, 624.

[49]   Still, T.; Yunker, P. J.; Yodh, A. G., Surfactant-Induced Marangoni Eddies Alter the Coffee-Rings of Evaporating Colloidal Drops. *Langmuir* **2012,** *28*, 4984.

[50]   Sempels, W.; De Dier, R.; Mizuno, H.; Hofkens, J.; Vermant, J., Auto-production of biosurfactants reverses the coffee ring effect in a bacterial system. *Nat. Commun.* **2013,** *4*, 1757.

[51]   Duan, F.; Ward, C. A., Surface excess properties from energy transport measurements during water evaporation. *Phys Rev E Stat Nonlin Soft Matter Phys* **2005,** *72*, 056302.

[52]   Hu, H.; Larson, R. G., Marangoni effect reverses coffee-ring depositions. *Journal of Physical Chemistry B* **2006,** *110*, 7090.

[53]   Kang, K. H.; Lim, H. C.; Lee, H. W.; Lee, S. J., Evaporation-induced saline Rayleigh convection inside a colloidal droplet. *Physics of Fluids* **2013,** *25*, 042001.

[54]   Zhang, Z.; Zhang, X.; Xin, Z.; Deng, M.; Wen, Y.; Song, Y., Controlled inkjetting of a conductive pattern of silver nanoparticles based on the coffee‐ring effect. *Advanced Materials* **2013,** *25*, 6714.

[55]   Nguyen, V. X.; Stebe, K. J., Patterning of small particles by a surfactant-enhanced Marangoni-Benard instability. *Physical Review Letters* **2002,** *88*, 164501.

[56]   Park, J.; Moon, J., Control of Colloidal Particle Deposit Patterns within Picoliter Droplets Ejected by Ink-Jet Printing. *Langmuir* **2006,** *22*, 3506.

[57]   de Gans, B.-J.; Duineveld, P. C.; Schubert, U. S., Inkjet Printing of Polymers: State of the Art and Future Developments. *Advanced Materials* **2004,** *16*, 203.

[58]   Deng, Y.; Zhu, X. Y.; Kienlen, T.; Guo, A., Transport at the Air/Water Interface is the Reason for Rings in Protein Microarrays. *Journal of the American Chemical Society* **2006,** *128*, 2768.

[59]   Cui, L. Y.; Zhang, J. H.; Zhang, X. M.; Li, Y. F.; Wang, Z. H.; Gao, H. N.; Wang, T. Q.; Zhu, S. J.; Yu, H. L.; Yang, B., Avoiding coffee ring structure based on hydrophobic silicon pillar arrays during single-drop evaporation. *Soft Matter* **2012,** *8*, 10448.

[60]   Chu, Z.; Seeger, S., Superamphiphobic surfaces. *Chemical Society Reviews* **2014,** *43*, 2784.

[61]   Yunker, P. J.; Still, T.; Lohr, M. A.; Yodh, A. G., Suppression of the coffee-ring effect by shape-dependent capillary interactions. *Nature* **2011,** *476*, 308.

[62] Li, Y.; Yang, Q.; Li, M.; Song, Y., Rate-dependent interface capture beyond the coffee-ring effect. *Sci Rep* **2016,** *6*, 24628.

[63] Deegan, R. D.; Bakajin, O.; Dupont, T. F.; Huber, G.; Nagel, S. R.; Witten, T. A., Contact line deposits in an evaporating drop. *Physical Review E* **2000,** *62*, 756.

[64] Lafuma, A.; Quere, D., Slippery pre-suffused surfaces. *Epl* **2011,** *96*, 56001.

[65] Wong, T. S.; Kang, S. H.; Tang, S. K.; Smythe, E. J.; Hatton, B. D.; Grinthal, A.; Aizenberg, J., Bioinspired self-repairing slippery surfaces with pressure-stable omniphobicity. *Nature* **2011,** *477*, 443.

[66] Smith, J. D.; Dhiman, R.; Anand, S.; Reza-Garduno, E.; Cohen, R. E.; McKinley, G. H.; Varanasi, K. K., Droplet mobility on lubricant-impregnated surfaces. *Soft Matter* **2013,** *9*, 1772.

[67] Schellenberger, F.; Xie, J.; Encinas, N.; Hardy, A.; Klapper, M.; Papadopoulos, P.; Butt, H. J.; Vollmer, D., Direct observation of drops on slippery lubricant-infused surfaces. *Soft Matter* **2015,** *11*, 7617.

[68] A.M.A. Archives of DermatologyTeisala, H.; Schönecker, C.; Kaltbeitzel, A.; Steffen, W.; Butt, H.-J.; Vollmer, D., Wetting over pre-existing liquid films. *Phys. Rev. Fluids* **2018,** *3*, 084002(13).

[69] Tress, M.; Karpitschka, S.; Papadopoulos, P.; Snoeijer, J. H.; Vollmer, D.; Butt, H. J., Shape of a sessile drop on a flat surface covered with a liquid film. *Soft Matter* **2017,** *13*, 3760.

[70] Guan, J. H.; Wells, G. G.; Xu, B.; McHale, G.; Wood, D.; Martin, J.; Stuart-Cole, S., Evaporation of Sessile Droplets on Slippery Liquid-Infused Porous Surfaces (SLIPS). *Langmuir* **2015,** *31*, 11781.

[71] Villers, D.; Platten, J. K., Temperature-Dependence of the Interfacial-Tension between Water and Long-Chain Alcohols. *Journal of Physical Chemistry* **1988,** *92*, 4023.

[72] Schatz, M. F.; Neitzel, G. P., Experiments On thermocapillary instabilities. *Annual Review of Fluid Mechanics* **2001,** *33*, 93.

[73] Eckert, K.; Bestehorn, M.; Thess, A., Square cells in surface-tension-driven Bénard convection: experiment and theory. *Journal of Fluid Mechanics* **1998,** *356*, 155.

[74] Nuz, A. E.; Nepomnyashchy, A. A.; Golovin, A. A.; Hari, A. A.; Pismen, L. M., Stability of rolls and hexagonal patterns in non-potential systems. *Physica D-Nonlinear Phenomena* **2000,** *135*, 233.

[75] Navier, C., Sur les lois de l'équilibre et du mouvement des corps élastiques. *Mem. Acad. R. Sci. Inst. France* **1827,** *6*, 1827.

[76] Choi, C.-H.; Westin, K. J. A.; Breuer, K. S., Apparent slip flows in hydrophilic and hydrophobic microchannels. *Physics of Fluids* **2003,** *15*, 2897.

[77] Neto, C.; Evans, D. R.; Bonaccurso, E.; Butt, H.-J.; Craig, V. S., Boundary slip in Newtonian liquids: a review of experimental studies. *Reports on Progress in Physics* **2005,** *68*, 2859.

[78] Bocquet, L.; Barrat, J.-L., Flow boundary conditions from nano-to micro-scales. *Soft Matter* **2007,** *3*, 685.

[79] Rothstein, J. P., Slip on Superhydrophobic Surfaces. *Annual Review of Fluid Mechanics* **2010,** *42*, 89.

[80] Philip, J. R., Flows satisfying mixed no-slip and no-shear conditions. *Zeitschrift für angewandte Mathematik und Physik ZAMP* **1972,** *23*, 353.

[81] Philip, J. R., Integral properties of flows satisfying mixed no-slip and no-shear conditions. *Zeitschrift für angewandte Mathematik und Physik ZAMP* **1972,** *23*, 960.

[82] Lauga, E.; Stone, H. A., Effective slip in pressure-driven Stokes flow. *Journal of Fluid Mechanics* **2003,** *489*, 55.

[83] Schönecker, C.; Hardt, S., Longitudinal and transverse flow over a cavity containing a second immiscible fluid. *Journal of Fluid Mechanics* **2013,** *717*, 376.

[84] Schönecker, C.; Baier, T.; Hardt, S., Influence of the enclosed fluid on the flow over a microstructured surface in the Cassie state. *Journal of Fluid Mechanics* **2014,** *740*, 168.

[85] Davis, A. M. J.; Lauga, E., Hydrodynamic friction of fakir-like superhydrophobic surfaces. *Journal of Fluid Mechanics* **2010,** *661*, 402.

[86] Cottin-Bizonne, C.; Barentin, C.; Charlaix, E.; Bocquet, L.; Barrat, J. L., Dynamics of simple liquids at heterogeneous surfaces: molecular-dynamics simulations and hydrodynamic description. *Eur Phys J E Soft Matter* **2004,** *15*, 427.

[87] Ybert, C.; Barentin, C.; Cottin-Bizonne, C.; Joseph, P.; Bocquet, L., Achieving large slip with superhydrophobic surfaces: Scaling laws for generic geometries. *Physics of Fluids* **2007,** *19*, 123601 (10).

[88] Baier, T.; Steffes, C.; Hardt, S., Numerical modelling of thermocapillary flow on superhydrophobic surfaces. In *14th International Conference on Miniaturized Systems for Chemistry and Life Sciences. Chemical and Biological Microsystems Society*, 2010.

[89] Goodwin, J.; Hearn, J.; Ho, C.; Ottewill, R., Studies on the preparation and characterisation of monodisperse polystyrene laticee. *Colloid and Polymer Science* **1974,** *252*, 464.

[90] Furusawa, K.; Norde, W.; Lyklema, J., A method for preparing surfactant-free polystyrene latices of high surface charge. *Kolloid-Zeitschrift & Zeitschrift für Polymere* **1972,** *250*, 908.

[91]   Deng, X.; Mammen, L.; Butt, H. J.; Vollmer, D., Candle soot as a template for a transparent robust superamphiphobic coating. *Science* **2012,** *335*, 67.

[92]   Paven, M.; Fuchs, R.; Yakabe, T.; Vollmer, D.; Kappl, M.; Itakura, A. N.; Butt, H. J., Mechanical Properties of Highly Porous Super Liquid-Repellent Surfaces. *Advanced Functional Materials* **2016,** *26*, 4914.

[93]   Stöber, W.; Fink, A.; Bohn, E., Controlled growth of monodisperse silica spheres in the micron size range. *Journal of Colloid and Interface Science* **1968,** *26*, 62.

[94]   Mammen, L.; Bley, K.; Papadopoulos, P.; Schellenberger, F.; Encinas, N.; Butt, H. J.; Weiss, C. K.; Vollmer, D., Functional superhydrophobic surfaces made of Janus micropillars. *Soft Matter* **2015,** *11*, 506.

[95]   Vakarelski, I. U.; Patankar, N. A.; Marston, J. O.; Chan, D. Y.; Thoroddsen, S. T., Stabilization of Leidenfrost vapour layer by textured superhydrophobic surfaces. *Nature* **2012,** *489*, 274.

[96]   Violle, J., STEFAN.—Ueber die Beziehung zwischen der Wärmestrahlung und der Temperatur (Sur la relation entre le rayonnement calorifique et la température); Sitzungs berichte d. K. Akademie d. Wissenschaften in Wien, p. 84. *J. Phys. Theor. Appl.* **1881,** *10*, 317.

[97]   Wilson, T.; Sheppard, C., *Theory and practice of scanning optical microscopy*. Academic Press London: 1984; Vol. 180.

[98]   Kino, G. S.; Corle, T. R., *Confocal scanning optical microscopy and related imaging systems*. Academic Press: 1996.

[99]   Thielicke, W.; Stamhuis, E. J., PIVlab – Towards User-friendly, Affordable and Accurate Digital Particle Image Velocimetry in MATLAB. *Journal of Open Research Software* **2014,** *2*.

[100]   Thielicke, W. The flapping flight of birds: Analysis and application. University of Groningen, 2014.

[101]   Kirchhoff, G., Black bodies.

[102]   Robitaille, P.-M., Blackbody radiation and the carbon particle. *Progress in Physics* **2008,** *3*, 36.

[103]   Donner, J. S.; Baffou, G.; McCloskey, D.; Quidant, R., Plasmon-assisted optofluidics. *Acs nano* **2011,** *5*, 5457.

[104]   Roxworthy, B. J.; Bhuiya, A. M.; Vanka, S. P.; Toussaint, K. C., Jr., Understanding and controlling plasmon-induced convection. *Nat Commun* **2014,** *5*, 3173 (10).

[105]   Landel, J. R.; Peaudecerf, F. J.; Temprano-Coleto, F.; Gibou, F.; Goldstein, R. E.; Luzzatto-Fegiz, P., A theory for the slip and drag of superhydrophobic surfaces with surfactant. *Journal of Fluid Mechanics* **2020,** *883*, A18 (50).

[106]   Enright, R.; Hodes, M.; Salamon, T.; Muzychka, Y., Isoflux Nusselt Number and Slip Length Formulae for Superhydrophobic Microchannels. *Journal of Heat Transfer-Transactions of the Asme* **2014,** *136*, 012402 (9).

[107]   Paven, M.; Papadopoulos, P.; Mammen, L.; Deng, X.; Sachdev, H.; Vollmer, D.; Butt, H. J., Optimization of superamphiphobic layers based on candle soot. *Pure and Applied Chemistry* **2014,** *86*, 87.

[108]   Navier, C., Mémoire sur les lois du mouvement des fluides. *Mémoires de l'Académie Royale des Sciences de l'Institut de France* **1823,** *6*, 389.

[109]   Peaudecerf, F. J.; Landel, J. R.; Goldstein, R. E.; Luzzatto-Fegiz, P., Traces of surfactants can severely limit the drag reduction of superhydrophobic surfaces. *Proc Natl Acad Sci U S A* **2017,** *114*, 7254.

[110]   Schaffel, D.; Koynov, K.; Vollmer, D.; Butt, H. J.; Schonecker, C., Local Flow Field and Slip Length of Superhydrophobic Surfaces. *Physical Review Letters* **2016,** *116*, 134501.

[111]   Bolognesi, G.; Cottin-Bizonne, C.; Pirat, C., Evidence of slippage breakdown for a superhydrophobic microchannel. *Physics of Fluids* **2014,** *26*, 082004.

[112]   Li, Y.; Diddens, C.; Lv, P.; Wijshoff, H.; Versluis, M.; Lohse, D., Gravitational Effect in Evaporating Binary Microdroplets. *Physical Review Letters* **2019,** *122*, 114501.

[113]   von Smoluchowski, M., Zur kinetischen Theorie der Brownschen Molekularbewegung und der Suspensionen. *Annalen der Physik* **1906,** *326*, 756.

[114]   Einstein, A., Zur theorie der brownschen bewegung. *Annalen der physik* **1906,** *324*, 371.

[115]   Song, D.; Song, B. W.; Hu, H. B.; Du, X. S.; Du, P.; Choi, C. H.; Rothstein, J. P., Effect of a surface tension gradient on the slip flow along a superhydrophobic air-water interface. *Physical Review Fluids* **2018,** *3*, 033303.

[116]   Gao, A.; Liu, J.; Ye, L.; Schönecker, C.; Kappl, M.; Butt, H.-J. r.; Steffen, W., Control of droplet evaporation on oil-coated surfaces for the synthesis of asymmetric supraparticles. *Langmuir* **2019,** *35*, 14042.

[117]   Young, T., III. An essay on the cohesion of fluids. *Philosophical Transactions of the Royal Society of London* **1805**, 65.

[118]   Wenzel, R. N., Resistance of solid surfaces to wetting by water. *Industrial & Engineering Chemistry* **1936,** *28*, 988.

[119]   De Gennes, P.-G.; Brochard-Wyart, F.; Quéré, D., *Capillarity and wetting phenomena: drops, bubbles, pearls, waves*. Springer Science & Business Media: 2013.

[120]   Butt, H.-J.; Kappl, M., *Surface and interfacial forces*. Wiley Online Library: 2010.

[121]   Princen, H.; Mason, S., Shape of a fluid drop at a fluid-liquid interface. II. Theory for three-phase systems. *Journal of Colloid Science* **1965,** *20*, 246.

[122]   Eirich, F. R.; Matijević, E., *Surface and colloid science*. Wiley-Interscience: 1969.

[123]   Pierre-Gilles de Gennes, F. D. Q., *Capillarity and Wetting Phenome*. 2002.

[124]   Daniel, D.; Timonen, J. V. I.; Li, R.; Velling, S. J.; Aizenberg, J., Oleoplaning droplets on lubricated surfaces. *Nature Physics* **2017,** *13*, 1020.

[125]   Israelachvili, J. N., *Intermolecular and surface forces*. Academic press: 2011.

[126]   Brochard-Wyart, F.; Di Meglio, J. M.; Quere, D.; De Gennes, P. G., Spreading of nonvolatile liquids in a continuum picture. *Langmuir* **1991,** *7*, 335.

[127]   Birdi, K.; Vu, D., Wettability and the evaporation rates of fluids from solid surfaces. *Journal of Adhesion Science and Technology* **1993,** *7*, 485.

[128]   Cao, M.; Guo, D.; Yu, C.; Li, K.; Liu, M.; Jiang, L., Water-Repellent Properties of Superhydrophobic and Lubricant-Infused "Slippery" Surfaces: A Brief Study on the Functions and Applications. *ACS Appl Mater Interfaces* **2016,** *8*, 3615.

[129]   Dugyala, V. R.; Basavaraj, M. G., Evaporation of Sessile Drops Containing Colloidal Rods: Coffee-Ring and Order-Disorder Transition. *Journal of Physical Chemistry B* **2015,** *119*, 3860.

[130]   Shanahan, M.; Bourges, C., Effects of evaporation on contact angles on polymer surfaces. *International Journal of Adhesion and Adhesives* **1994,** *14*, 201.

[131]   Bourges-Monnier, C.; Shanahan, M., Influence of evaporation on contact angle. *Langmuir* **1995,** *11*, 2820.

[132]   Bhardwaj, R.; Fang, X. H.; Attinger, D., Pattern formation during the evaporation of a colloidal nanoliter drop: a numerical and experimental study. *New Journal of Physics* **2009,** *11*, 075020.

[133]   Birdi, K.; Vu, D.; Winter, A., A study of the evaporation rates of small water drops placed on a solid surface. *The Journal of physical chemistry* **1989,** *93*, 3702.

[134]   Shin, D. H.; Lee, S. H.; Jung, J. Y.; Yoo, J. Y., Evaporating characteristics of sessile droplet on hydrophobic and hydrophilic surfaces. *Microelectronic Engineering* **2009,** *86*, 1350.

[135]   Sobac, B.; Brutin, D., Triple-line behavior and wettability controlled by nanocoated substrates: influence on sessile drop evaporation. *Langmuir* **2011,** *27*, 14999.

[136]   Grandas, L.; Reynard, C.; Santini, R.; Tadrist, L., Experimental study of the evaporation of a sessile drop on a heat wall. Wetting influence. *International Journal of Thermal Sciences* **2005,** *44*, 137.

[137]   Doganci, M. D.; Sesli, B. U.; Erbil, H. Y., Diffusion-controlled evaporation of sodium dodecyl sulfate solution drops placed on a hydrophobic substrate. *Journal of Colloid and Interface Science* **2011,** *362*, 524.

[138]   Semenov, S.; Starov, V.; Rubio, R.; Agogo, H.; Velarde, M., Evaporation of sessile water droplets: Universal behaviour in presence of contact angle hysteresis. *Colloids and Surfaces A: Physicochemical and Engineering Aspects* **2011,** *391*, 135.

[139]   Dash, S.; Garimella, S. V., Droplet evaporation dynamics on a superhydrophobic surface with negligible hysteresis. *Langmuir* **2013,** *29*, 10785.

[140]   Li, G.; Flores, S. M.; Vavilala, C.; Schmittel, M.; Graf, K., Evaporation dynamics of microdroplets on self-assembled monolayers of dialkyl disulfides. *Langmuir* **2009,** *25*, 13438.

[141]   Batchelor, C. K.; Batchelor, G., *An introduction to fluid dynamics*. Cambridge university press: 2000.

[142]   Picknett, R.; Bexon, R., The evaporation of sessile or pendant drops in still air. *Journal of Colloid and Interface Science* **1977,** *61*, 336.

[143]   Rowan, S. M.; Newton, M.; McHale, G., Evaporation of microdroplets and the wetting of solid surfaces. *The Journal of physical chemistry* **1995,** *99*, 13268.

[144]   Lebedev, N. N., *Special functions and their applications*. Prentice-Hall: 1965.

[145]   Hu, H.; Larson, R. G., Evaporation of a sessile droplet on a substrate. *Journal of Physical Chemistry B* **2002,** *106*, 1334.

[146]   Popov, Y. O., Evaporative deposition patterns: Spatial dimensions of the deposit. *Physical Review E* **2005,** *71*.

[147]   Stauber, J. M.; Wilson, S. K.; Duffy, B. R.; Sefiane, K., Evaporation of droplets on strongly hydrophobic substrates. *Langmuir* **2015,** *31*, 3653.

[148]   Smith, G. S.; Barakat, R., Electrostatics of two conducting spheres in contact. *Applied Scientific Research* **1975,** *30*, 418.

[149]   Jackson, J. D., *Classical electrodynamics*. John Wiley & Sons: 2007.

[150]   Li, Y.; Diddens, C.; Segers, T.; Wijshoff, H.; Versluis, M.; Lohse, D., Evaporating droplets on oil-wetted surfaces: Suppression of the coffee-stain effect. *Proc Natl Acad Sci U S A* **2020**, 16756.

[151]   Barankin, M. D.; Gonzalez, E., 2nd; Habib, S. B.; Gao, L.; Guschl, P. C.; Hicks, R. F., Hydrophobic films by atmospheric plasma curing of spun-on liquid precursors. *Langmuir* **2009,** *25*, 2495.

[152]   Bhattacharya, S.; Datta, A.; Berg, J. M.; Gangopadhyay, S., Studies on surface wettability of poly(dimethyl) siloxane (PDMS) and glass under oxygen-plasma treatment and correlation with bond strength. *Journal of Microelectromechanical Systems* **2005,** *14*, 590.

[153]   Wooh, S.; Butt, H. J., A Photocatalytically Active Lubricant-Impregnated Surface. *Angewandte Chemie, International Edition in English* **2017,** *56*, 4965.

[154]   Emslie, A. G.; Bonner, F. T.; Peck, L. G., Flow of a Viscous Liquid on a Rotating Disk. *Journal of Applied Physics* **1958,** *29*, 858.

[155]   Ohara, T.; Matsumoto, Y.; Ohashi, H., The Film Formation Dynamics in Spin Coating. *Physics of Fluids a-Fluid Dynamics* **1989,** *1*, 1949.

[156]   Butt, H.-J.; Graf, K.; Kappl, M., *Physics and chemistry of interfaces*. John Wiley & Sons: 2013.

[157]   van der Veen, R. C.; Tran, T.; Lohse, D.; Sun, C., Direct measurements of air layer profiles under impacting droplets using high-speed color interferometry. *Phys Rev E Stat Nonlin Soft Matter Phys* **2012,** *85*, 026315.

[158]   Daniel, D.; Timonen, J. V. I.; Li, R. P.; Velling, S. J.; Aizenberg, J., Oleoplaning droplets on lubricated surfaces. *Nature Physics* **2017,** *13*, 1020.

[159]   de Ruiter, J.; Mugele, F.; van den Ende, D., Air cushioning in droplet impact. I. Dynamics of thin films studied by dual wavelength reflection interference microscopy. *Physics of Fluids* **2015,** *27*, 012104.

[160]   Born, M.; Wolf, E., *Principles of optics: electromagnetic theory of propagation, interference and diffraction of light*. Elsevier: 2013.

[161]   Pieranski, P., Two-Dimensional Interfacial Colloidal Crystals. *Physical Review Letters* **1980,** *45*, 569.

[162]   Du, K.; Glogowski, E.; Emrick, T.; Russell, T. P.; Dinsmore, A. D., Adsorption energy of nano- and microparticles at liquid-liquid interfaces. *Langmuir* **2010,** *26*, 12518.

[163]   Rastogi, V.; Melle, S.; Calderon, O. G.; Garcia, A. A.; Marquez, M.; Velev, O. D., Synthesis of Light-Diffracting Assemblies from Microspheres and Nanoparticles in Droplets on a Superhydrophobic Surface. *Advanced Materials* **2008,** *20*, 4263.

[164]   Marin, A. G.; Gelderblom, H.; Susarrey-Arce, A.; van Houselt, A.; Lefferts, L.; Gardeniers, J. G.; Lohse, D.; Snoeijer, J. H., Building microscopic soccer balls with evaporating colloidal fakir drops. *Proc Natl Acad Sci U S A* **2012,** *109*, 16455.

[165]   Wooh, S.; Huesmann, H.; Tahir, M. N.; Paven, M.; Wichmann, K.; Vollmer, D.; Tremel, W.; Papadopoulos, P.; Butt, H. J., Synthesis of Mesoporous Supraparticles on Superamphiphobic Surfaces. *Advanced Materials* **2015,** *27*, 7338.

[166]   Liu, W.; Midya, J.; Kappl, M.; Butt, H.-J. r.; Nikoubashman, A., Segregation in Drying Binary Colloidal Droplets. *ACS nano* **2019,** *13*, 4972.

[167]   Butt, H. J.; Vollmer, D.; Papadopoulos, P., Super liquid-repellent layers: The smaller the better. *Advances in Colloid and Interface Science* **2015,** *222*, 104.

[168]   Teisala, H.; Butt, H.-J., Hierarchical Structures for Superhydrophobic and Superoleophobic Surfaces. *Langmuir* **2019,** *35*, 10689.

[169]   Chen, X.; Ma, R.; Li, J.; Hao, C.; Guo, W.; Luk, B. L.; Li, S. C.; Yao, S.; Wang, Z., Evaporation of droplets on superhydrophobic surfaces: Surface roughness and small droplet size effects. *Physical Review Letters* **2012,** *109*, 116101.

[170]   Deng, T.; Varanasi, K. K.; Hsu, M.; Bhate, N.; Keimel, C.; Stein, J.; Blohm, M., Nonwetting of impinging droplets on textured surfaces. *Applied Physics Letters* **2009,** *94*, 133109.

Bibliography

Variables

σ, γ	Surface tension
σ_T	Surface tension temperature coefficient
$\gamma_{i,j}$	Interfacial tension between two immiscible phases denoted by subscripts i and j
$\partial\sigma/\partial r$	Surface tension gradient along the liquid interface (in r-direction)
T	Temperature
$\partial\mathrm{T}/\partial r$	Temperature gradient along r-direction
ΔT	Temperature difference
T_0	Reference temperature
$\tau_{(\sigma)}$	Tangential stress due to surface tension variation
$\tau_{(\mu)}$	Viscous stress
β	Thermal expansion efficient
α	Thermal diffusion, $\alpha = \kappa/\rho c_p$
κ	Thermal conductivity
ρ	Density
L	Characterized length
ν	Kinematic viscosity, $\nu = \mu/\rho$
η/μ	Dynamic viscosity
N	Viscosity ratio between fluid 1 and fluid 2, μ_1/μ_2
c_p	Specific heat capacity
p	Pressure
g	Gravity acceleration
F	Body force
q	Heat flux
u	Velocity vector
u_r	Velocity component along r-direction
u_z	Velocity component in z-direction

u_M	Thermocapillary velocity
U_w	Boundary velocity
Ma	Marangoni number
b	Slip length
b_l	Slip length in the longitudinal case
b_t	Slip length in the transverse case
b_l^*	Normalized slip length in the longitudinal case
b_t^*	Normalized slip length in the transverse case
ϕ_g	Air fraction
θ	Static contact angle
θ_{adv}	Advancing contact angle
θ_{rec}	Receding contact angle
θ_{CAH}	Contact angle hysteresis
λ_c	Capillary length
D	Diffusion coefficient
V	Droplet volume
R	Droplet base radius
h	Droplet height
J	Evaporation flux along the droplet surface
c_0	Vapor concentration at the droplet surface
c_∞	Vapor concentration in the atmosphere
$S_{\mathrm{ol(a)}}$	Spreading coefficient due to interfacial tensions among liquid-air, liquid-oil and oil-air interfaces
$S_{\mathrm{ol(s)}}$	Spreading coefficient due to interfacial tensions among liquid-solid, liquid-oil and oil-solid interfaces
h_s	The height of oil wetting ridge
P	Capillary force
Π_{D}	Disjoining pressure
A_H	Hamaker constant
B	Oil film thickness at the droplet apex
t	Time

Δt	Time intervial
t_0	Initial time
t_f	Final time
ω	Spin speed
Q_{laser}	Laser power
λ	Wavelength
λ_{exc}	Excitation wavelength
n	Reflection index
d_z	Optical section thickness

Acronyms

PDMS   Polydimethylsiloxane

PS   Polystyrene

SDS   Sodium dodecyl sulfate

OTS   Octadecyltrichlorosilane

CVD   Chemical Vapor Deposition process

CLSM   Confocal Laser Scanning Microscope

SEM   Scanning Electron Microscope

PIV   Microparticle Image Velocimetry

IA   Interrogation area

FFT   Fast Fourier transform window deformation

CCA   Constant contact angle mode

CCR   Constant contact area mode

TCL   Three-phase contact line

Acknowledgements

Curriculum Vitae